The Dissertation Committee for Zhiyuan Luo certifies that this is the approved version of the following dissertation:

Modeling Injection Induced Fractures and Their Impact in CO_2 Geological Storage

Committee:

Steven L. Bryant, Supervisor

Kamy Sepehrnoori

Jon Olson

Sanjay Srinivasan

Jean-Philippe Nicot

Modeling Injection Induced Fractures and Their Impact in CO_2 Geological Storage

by

Zhiyuan Luo, B.E.; M.S.

Dissertation

Presented to the Faculty of the Graduate School of

The University of Texas at Austin

in Partial Fulfillment

of the Requirements

for the Degree of

Doctor of Philosophy

The University of Texas at Austin

August 2013

Dedication

To my parents, my wife and my daughter

Acknowledgements

I would like to express my most sincere gratitude and appreciation to my supervisor, Dr. Steven L. Bryant for his constant support, patience and guidance during Ph.D study of research work. I also want to thank Dr. Steven Bryant for his generosity in spending hours and hours editing my dissertation. My sincere appreciation goes to him for teaching me on how to approach complex problems and technical writing. I would also like to thank and appreciate all guidance and comments that I received from my supervising committee members, Dr. Jon Olson, Dr. Sanjay Srinivasan, and Dr. Kamy Sepehrnoori from the Department of Petroleum and Geo-systems Engineering and Dr. Jean-Philippe Nicot from Bureau of Economic Geology.

I am also grateful to the financial support from the Geological CO_2 Storage Industrial Affiliates Program at The University of Texas at Austin, who guaranteed my research facility and my cost of living.

I am thankful to Dr. Timothy A. Meckel in Bureau of Economic Geology to provide precious field measurements and suggestions to my research.

I would like to express my deep gratitude to my colleagues and friends Dean A. Checkai, Nicolas J.Huerta, David Alexander, Javad Behseresht, Qing Tao, Yao Peng, Li Ji, Ehsan Saadatpoor, Yagna Oruganti, Yuhao Sun, Bo Ren, and Yun Wu. It is enlightening and enjoyable to work with you together.

Modeling Injection Induced Fractures and Their Impact in CO_2 Geological Storage

Zhiyuan Luo, Ph.D

The University of Texas at Austin, 2013

Supervisor: Steven L. Bryant

Large-scale geologic CO_2 storage is a technically feasible way to reduce anthropogenic emission of green house gas to atmosphere by human beings. In large-scale geologic CO_2 sequestration, high injection rate is required to satisfy economics and operational considerations. During the injection phase, temperature and pressure of the storage aquifers may vary significantly with the introduced CO_2. These changes would re-distribute the in-situ stresses in formations and induce fracture initiation or even propagation. If fractures are not permitted by regulators, then the injection operation strategies must be supervised and designed to prevent fracture initiation, and the storage formations should be screened for risk of fracturing. In more flexible regulatory environment, if fractures are allowed, fractures would strongly influence the CO_2 migration profile and storage site usage efficiency depending on fracture length and growth rate.

In this dissertation, we built analytical heat transfer models for vertical and horizontal injection wells. The models account for the dependency of overall heat transfer coefficient on injection rate to more accurately predict the borehole temperature. Based on these models, we can calculate temperature change in formation surrounding

wellbores and thus evaluate thermo-elastic stress around borehole as well as its impact on fracture initiation pressure. By considering the impact of thermo-elastic effect on fracturing pressure, we predicted maximum injection rate avoiding fracture initiation and provided injection and storage strategies to increase the maximum safe injection rate. The results show that thermo-elastic stress significantly limits maximum injection rate for no-fractured injection scenario, especially for horizontal injectors. To improve injection rate, partial perforation and pre-heating CO_2 before injection have been designed, and results shows that these strategies can strongly negate thermo-elastic influence for various injection scenarios. On the other hand, the model provides parametric analysis on geological and operational conditions of CO_2 storage project for site screening work.

In the case of permitting fracture occurrence, a semi-analytical model was built to quantitatively describe fracture propagation and injected fluid migration profile of a fractured vertical injector for storage systems with various boundary conditions. We examined the correlation between fracture growth and CO_2 migration in various injection scenarios. Two-phase fractional flow model of Buckley-Leverett theory has been extended to account for the CO_2-brine three-region flow system (dry CO_2, CO_2-brine, and brine) from a fractured injector. In the sensitivity study, fracture growth and fluid migration greatly depend on Young's modulus of the formation rock and storage site boundary conditions. Consequently, the results show that fast growing, long fractures may yield a flooding pattern with large aspect ratio, as well as early breakthrough at the drainage boundary; in contrast, slow growing short fractures provides high injectivity without changing flooded area shape.

We studied the physics for issues related to injection induced fractures in geologic CO_2 sequestration in saline aquifers, assessed risk associated to them and developed low cost and quick analytical models. These models could easily provide predictions on

maximum injection rate in no-fracture regulation CO_2 storage projects as well as estimate fracture growth and injected fluid migration under fracture allowable scenarios. "Preferred storage aquifers" have following properties: larger permeability, deep formation, no over pressure, low Young's modulus and low Poisson's ratio and open boundaries. In many practical cases, however, injection strategies have to be designed if some properties of formation are out of ideal range. Besides applications in CO_2 storage, the approach and model we developed can also be applied into any injection induced fracture topics, namely water/CO_2 flooding and wasted water re-injection.

Table of Contents

List of Tables

List of Figures

Chapter 1 Introduction

1.1 Background of geological CO_2 storage in saline aquifer

In the past decades, a trend of rising global temperature associated with increasing amount of greenhouse gas has been acknowledged by more and more scientists (Houghton, 1997). Because of its large quantities emitted to atmosphere, anthropogenic CO_2 is the most common greenhouse gas as shown in Fig. 1.1. In 2004, the global CO_2 emission was about 28 Gt. Between 1970 and 2004, annual emission of CO_2 grew by about 80% (IPCC, 2007). Fig. 1.2 shows world CO_2 emission and growth projections by the Energy Information Administration (EIA) for various economic growth scenarios (IEA, 2006).

To mitigate the effect of anthropogenic emission of CO_2, multiple technologies are required. Due to the large amount CO_2 emission each year, geological storage must play a leading role. For standard process of geological storage, CO_2 is captured from major sources such as fossil-fuel power plants, and then is compressed, transported, and injected through injection wells to target storage formations, which could be depleted oil or gas reservoirs, depleted or unmineable coal bed, and deep saline aquifer (Beilinski, 2007).

The idea of CO_2 geological sequestration was first proposed in 1970s. After 1990s, plenty of researches have been conducted (van der Meer, 1992; Bachu, 1994; Bergman, 1999; Takahashi, 2000; Orr, 2004; Pruess, 2005; Hovorka, 2006; Oldenburg, 2007; Bryant, 2007; Benson, 2008; Saadatpoor, 2010; Zoback, 2012; Heinemann, 2013). On the other hand, there are some CO_2 geological sequestration projects ranging from pilot-scale to commercial scale CO_2 geological sequestration projects currently running.

From mid-1990, Statoil started to inject CO_2 into Sleipner gas field to displace natural gas with an injection rate about 1 million tons per year through a single well. Another commercial-scale ongoing operation is conducted by BP at In Salah gas field in Algeria. Since 2004, nearly 1 million tons of CO_2 per year has been injected into the formations where gas is produced. In the U.S., Denbury operated Cranfield CO_2 EOR/sequestration projects which injected about 1 to 1.5 million tons of CO_2 per year since 2009.

Depleted oil and gas fields are favorable CO_2 storage sites, because they have proven to store fluids for very long time due to their geological structure. Further, the geological and hydraulic operation and assessment equipments are readily available for injection and monitoring with some improvements and modification. Additionally, CO_2 injection to depleted reservoirs can help to recover remaining oil or gas from reservoir. Therefore, this type of storage produces oil and meanwhile geologically stores CO_2. Due to economic benefit, CO_2 EOR projects are expanding around the world, especially in west Texas. The total of amount of CO_2 sales to EOR industry in 2012 is 3.35 BCF/day , which increases almost ten times from 1986 (Courtesy Melzer Consulting).

However, storage capacity and location limit the application of this storage approach worldwide (Fig 1.3). On the other hand, deep saline aquifers (deeper than 800m from surface) in large sedimentary basins are best suited with tremendous pore volume and they are distributed in every continent (Bachu, 2003; Benson, 2008) (Fig. 1.4). From Fig. 1.3, we know saline aquifer owns the largest capacity which is sufficient to hold decades of anthropogenic CO_2 emissions in the future. Of equal importance, storage in sedimentary rocks has a key advantage: oil industry is experienced on injecting large volumes of fluids into such type of formations.

Common deep saline aquifers comprise of sandstone or limestone in formations with permeability of 10 md to several hundreds of millidarcy. The overburden and

underburden confinements of aquifers are aquitards, mainly comprised of shale, which has very low permeability and could serve as effective sealing layers for CO_2 storage. When CO_2 is sequestered in a geological formation, there are five main mechanisms for long-term (hundreds of years) storage:

- Stratigraphic trapping: Capillary entry pressure of sealing layer is higher than pore pressure of stored CO_2. Hence, CO_2 cannot enter cap rock.
- Permeability trapping: Cap rock prevents CO_2 from rising upwards due to its low permeability. Migration for CO_2 diffusion through the cap rock takes millions of years.
- Residual fluid trapping: During migration in aquifer, CO_2 plume leaves behind a region of residual saturation, as CO_2 is non-wetting phase compared to brine.
- Solubility trapping: CO_2 and brine mutually dissolve in each other and stay in aquifer.
- Mineral trapping: CO_2 reacts with formation rocks and causes carbonate minerals to precipitate, a geochemistry process which is expected to take place very slowly.

Along with the benefit of storing CO_2 in saline aquifer, risks are also associated. The biggest risk is leakage. As CO_2 is less dense than formation brine, once there are conduits connecting the storage formation with shallow formations, the CO_2 can migrate upward, contaminating or perturbing other subsurface resources, such as groundwater, and possibly reaching the surface to enter the atmosphere. There are several types of potential conduits for leakage. As shown in Fig. 1.5, poor cementing for bore hole of injectors and abandoned well may be poorly cemented with non-isolated intervals between wellbore and formation, which act like high conductivity conduits for leakage

(Wertz et al., 2008; Tao et al., 2012). Fractures and faults are listed at high level risk for leakage. In Fig 1.5, one type of fracture is injection induced, which occurs within the storage formation as indicated by "1". This type of fracture grows with CO_2 migration and may or may not connect with naturally pre-existing faults or fractures, depending on injection operation and formation geological condition. This type of fracture is the research objective in my Ph.D work and thus this dissertation conducts a comprehensive study on it. Another type of fracture occurs in cap rocks (the sealing) of storage formation when pore pressure in storage formation is too high and causes tensile failure or shear failure in cap rock (Gor et al., 2012) as indicated by "2". If cap rock is weak or has natural flaws, this type of fracture occurs relatively easily. As indicated by "3", naturally pre-existing fractures or faults in aquifer or cap rock connect to upper formations. CO_2 may leak through those conduits to upper aquifer or even the surface, which has been investigated a lot (Pruess, 2008; Chang et al., 2008). Those three types of fracture and intervals between wellbore and formation constitute main paths for leakage. In the following, we will provide generic description of processes leading to injection induced fractures.

1.2 CO_2 INJECTION INDUCED FRACTURE AND ITS INFLUENCE

Commercial CO_2 geologic storage will require large injection rates and economic consideration will favor pipeline transport of CO_2 as a dense (liquid) phase. We can take a simple calculation here to understand the average amount of CO_2 emission from coal power plant. According to EPA (U.S. Environmental Protection Agency) data in 2012, the average CO_2 emission per coal power plant in the U.S. in 2009 is 9680 ton/d. For CO_2 at typical bottom hole conditions (density 0.8 ton/m^3), this corresponds to an injection

rate of 76,107 reservoir barrels/day, which is an extremely high rate for a single injection well. In practice, multiple injection wells will be needed, but those wells will still operate at large injection rates to minimize costs.

High injection rate results high bottom hole pressure for injection, which is one reason for fracture initiation and propagation from injector in storage formations. However, the bottom hole pressure is not as high as that in hydraulic fracturing treatment. The other more important reason is thermally induced stress, also known as thermo-elastic stress, may remarkably reduce pressure needed for fracture initiation and propagation in storage formations (Perkins and Gonzalez, 1985; Clifford et al., 1991). When CO_2 is injected at high rate, the temperature of CO_2 entering a storage formation may be significantly lower than the formation temperature at large injection rate. This means injected CO_2 will cool formation rock near borehole. That temperature change causes a thermo-elastic deformation of the rock and thus induces thermo-elastic stress that reduces in-site stresses in the formation. Since minimum in-situ stress is the most important factor on fracture initiation and propagation criteria, fracture initiation and propagation pressure indeed decrease. It is not hard to conclude that large injection rate may cause fractures to occur more easily. On the other hand, although poro-elastic effect can cancel part of thermo-elastic effect, since poro-elastic effect is much weaker in CO_2 injection process, the impact of thermo-elastic effect is still dominant.

Injection induced fracture differs significantly from hydraulic fracture for stimulation. We summarize several features of injection induced fracture distinct from hydraulic fracture treatment in studies of Clifford et al. (1989) and Saripalli et al. (1999):

1. Injection induced fracture growth is normally determined through an equilibrium with fluid pressure and rock stress field. Since injected

fluid viscosity is low, and timescales are long, there is no restriction on fracture growth due to flow velocity within it.

2. Injected fluid in fracture has a very high leak-off rate (almost 100% of injected fluid leaves fracture very rapidly), which means that pressure in fracture cannot be derived without reference to the whole reservoir.
3. There is strong coupling between injection induced fracture growth, injected fluid cooling and fluid pressurization, and in-situ stresses variations.
4. Injection induced fracture grows slower but in a longer time compared to hydraulic fracturing treatment. The main mechanism for injection induced fractures is the impact of thermally induced stress on fracture criterion pressure. The impact of CO_2 chemical corrosion on rocks is too small in the time scale of CO_2 injection period (less than 100 years), although it plays important role in natural fractures growing process in geological time scale (thousands of years to millions of years).

An example of thermo-elastic effect impact on fracturing is CO_2 injection well KB-503z at In Salah, Algeria (data from In Sarah Project info disc). The temperature change of rock near bottom hole is about 40^{o}C at 1650 m depth (from surface) at injection rate 450 ton/d, corresponding to about 14 MPa thermo-elastic stress (assuming a typical coefficient of thermo-elasticity of 1.5×10^{-5} K^{-1}). The nominal fracture pressure is 30 MPa (before injection) so accounting for thermo-elastic stress reduces the fracture initiation pressure to 16 MPa. In that case, avoiding fracturing the injector would thus impose a severe limitation on injection rate.

As fractures are potential conduits for leakage, they may not be permitted by regulators for CO_2 sequestration in some sites. This may be true even for injection-

induced fractures, which remain in confined storage formation by underburden and overburden sealing formations. Injection induced fractures grow from injector with high conductivity, which could be seen as an extension of injector. When induced fractures grow very fast, they can reach the boundary of storage site rapidly. In this case, fractures resemble high ways directly connecting injector with outside of the storage site. This is one mechanism for potential leakage. The other potential risk is intersections between induced fractures and natural pre-existing fractures or faults. The intersections are exits to outside of storage formation and highly risky. Therefore, regulators may not allow injection induced fractures in CO_2 sequestration projects even if the stored CO_2 tends to stay in storage formation.

Considerations of fracture risk may lead toward lower injection rates, which is not satisfactory in large-scale CO_2 sequestration projects. Therefore, predictions of the maximum injection rate with considering thermo-elastic effect are necessary. Optimizations to overcome impact of thermo-elastic effect and thus to recover injection rate without fracturing storage formation are given in this dissertation.

Even if injection-induced fractures were to be permitted, understanding their propagation is very important to CO_2 sequestration, as fracture growth pattern can affect CO_2 migration in saline aquifer. Fracture growth is directly related to CO_2 flow performance, i.e. the relationship between bottom hole pressure and injection rate, as well as site storage usage efficiency (flow breakthrough time). However, published work on this topic is seldom seen. Fortunately, the gap will be filled by our work in this dissertation.

1.3 RESEARCH OBJECTIVES AND MAJOR CONTRIBUTIONS

In commercial larger-scale commercial CO_2 sequestration, every injection well has to encounter thermal induced fracture, either initiation or propagation. The hypothesis to be tested in this research is that if CO_2 sequestration is implemented at a large scale, the injection induced thermo-elastic stress would greatly impact injection strategy. The objectives of this dissertation are:

1. To determine thermal induced stress by injection, accurately estimate bottom hole temperature through simple analytical wellbore heat transfer model for vertical and horizontal injectors.
2. Analyze field measurements of injection rate and bottom hole temperature to regress the correlation between injection rate and heat transfer coefficient for calibrating heat transfer model.
3. Evaluate maximum injection rate of vertical and horizontal injector for injection projects under rigorous no-fracture regulation.
4. Optimize injection operation to increase maximum injection rate under no-fracture regulation.
5. Provide guidance for screening storage sites which can satisfy high injection rates without fracture occurring.
6. Evaluate fracture growth and its influence on CO_2 migration during injection and discuss effect of system boundary conditions. Compare difference of flow performance and fracture growth between traditional piston-like single-phase flow model and two-phase fractional flow model.

The major contributions of this work are listed in the following:

1. Build wellbore heat transfer models for vertical injector and horizontal injector and against the model with Cranfield measurements.
2. Regress correlation between heat transfer coefficient and injection rate and apply this correlation for injectors with dynamic flow rate scenarios to improve accuracy of model.
3. Provide guidelines on formation properties for CO_2 storage site screening.
4. Restrict maximum injection rate for vertical and horizontal injectors under rigorous no-fracture regulation.
5. Modify fracture propagation criterion for injection induced fracture by incorporating concept of fracture toughness.
6. Improve traditional single-phase injection induced fracturing model with two-phase Buckley-Leverett fractional flow theory to more accurately describe CO_2-brine system migration.
7. Study effect of boundary condition on injection induced fracture growth and corresponding CO_2 migration.

1.4 OVERVIEW OF CHAPTERS

Chapter 1 introduces global warming as a result of continuously increasing anthropogenic CO_2 emission and geological CO_2 sequestration in deep saline aquifer as a technically feasible solution. Large-scale CO_2 injection may induce fracture in storage formation which has have the potential to increase risk of leakage. Fracture avoiding and fracture growth prediction are the key objectives in this dissertation.

Chapter 2 contains a review of literature pertaining wellbore heat transfer and injection induced fracture. It discusses analytical models and commercial software on heat transfer between borehole fluid and surrounding formations for estimating bottom hole temperature in a flowing well. Injection induced fracture has been widely studied in water flooding work. Analytical and numerical simulation approaches by various authors are reviewed.

Chapter 3 first describes injection induced stresses and domination of two types of stresses. After that, we discuss fracture initiation criteria of vertical injector and horizontal injector accounting for the influence of two stresses.

Chapter 4 introduces our heat transfer model for vertical injector and horizontal injector. With measurements of Cranfield CO_2 injector, the heat transfer model of vertical injector has been validated and a correlation between heat transfer coefficient and injection rate is regressed which could be applied in injection with rate variation, such as dynamic injection rate of vertical injector or flow rate variation along horizontal injector.

Chapter 5 describes the restrictions on the maximum injection rate of vertical injector at various injection scenarios under no-fracture regulation. Based on fracture initiation criterion, parametric analysis provides guidance on storage site screening and optimizations to increase the maximum injection rate without fracture occurring in storage formation.

Chapter 6 is analogous to Chapter 5 but applies to horizontal injectors.

Chapter 7 first introduces criterion of fracture propagation for vertical injector and the semi-analytical model for estimating fracture growth as well as CO_2 migration in storage formation. By parametric analysis, it points out the influence of fracture growth on CO_2 flow performance in various injection scenarios. To more practically mimic fracture growth and CO_2 migration in storage system, effects of system boundary

condition are investigated. On the other hand, traditional injection induced fracture model has been improved with two-phase fractional flow theory in elliptical coordinate system. Combining this update with fracture propagation model, we can describe the region with CO_2-brine mutually dissolved mixture and more accurately predict CO_2 migration in storage formation.

Chapter 8 summarizes and concludes the work done towards this dissertation, and also lists recommendations for future work.

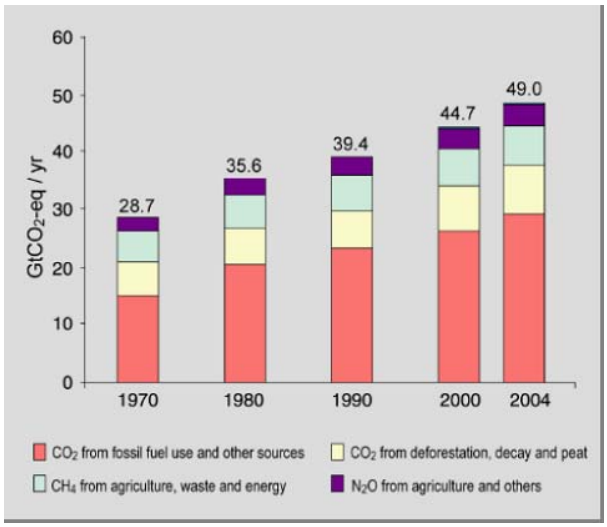

Figure 1.1: (a) Global annual emissions of anthropogenic GHGs from 1970 to 2004 (from IPCC Fourth Assessment Report, 2007).

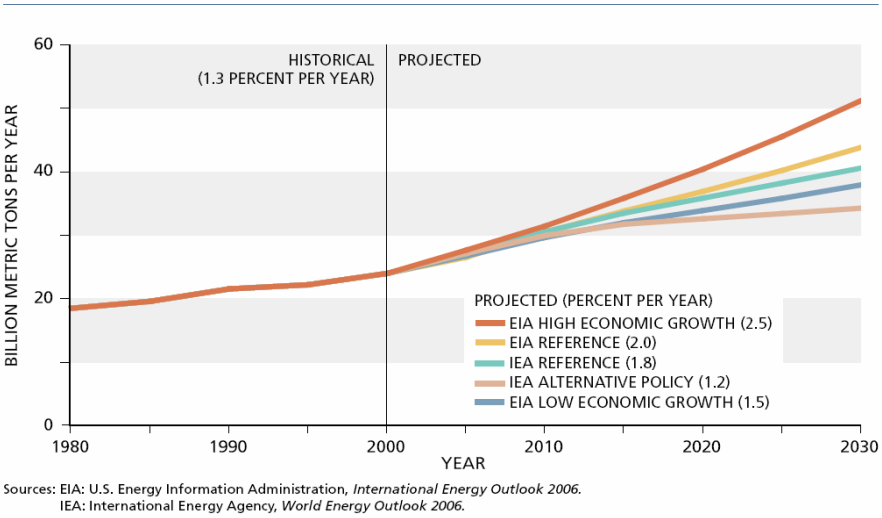

Figure 1.2: World Carbon Dioxide Emissions — Growth Projections (EIA, 2006)

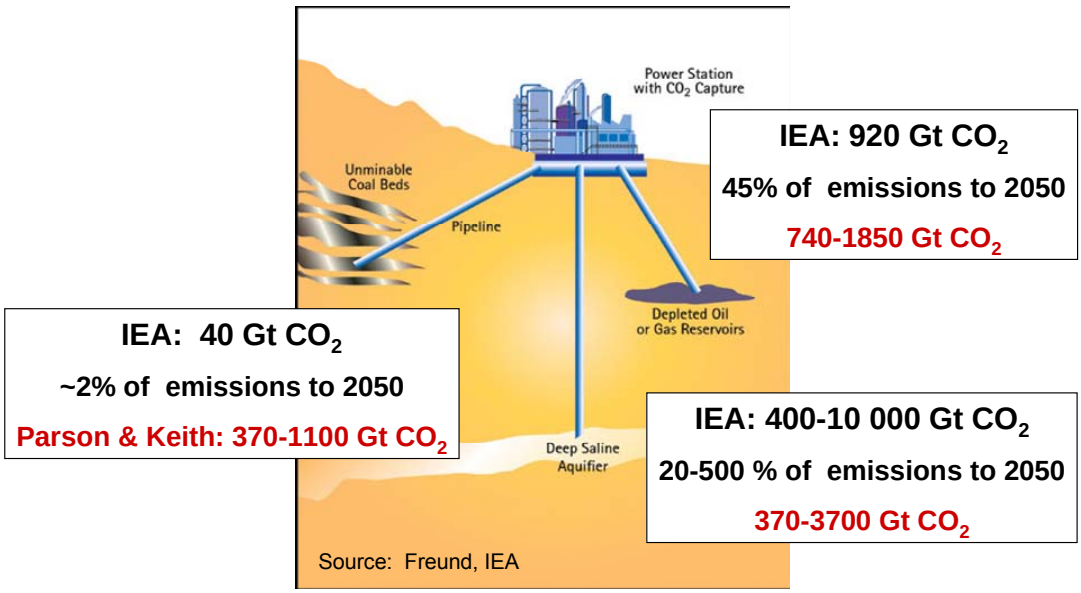

Figure 1.3: Geological storage potential of each type of site for CO_2 (IPCC 2007)

Figure 1.4: Sedimentary basins showing suitability as sequestration sites (IPCC 2005)

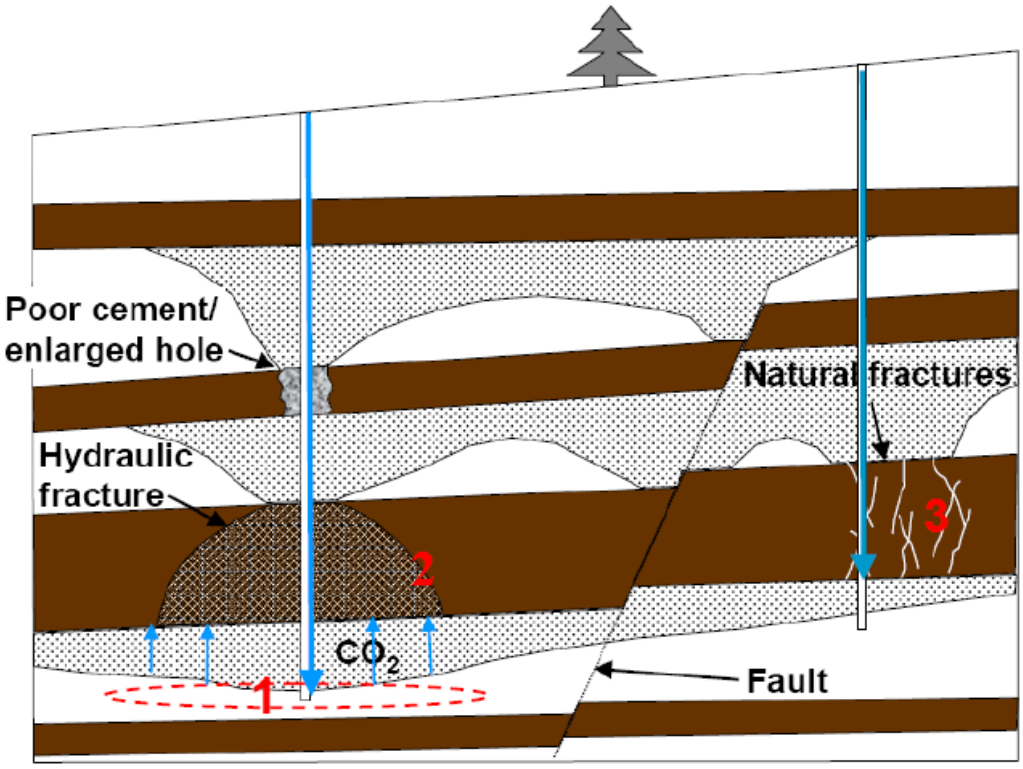

Figure 1.5: Potential leakages of CO_2 sequestration in saline aquifer. Poor cementing may cause CO_2 leaks along high conductivity intervals between wellbore and formation; the red ellipse labeled by "1" stands for injection induced fracture, while may intersect with pre-existing fractures/faults as conduits for leakage; "2" stands for hydraulic fracture in poor cap rock; "3" stands for pre-existed natural fractures in cap rock.

Chapter 2 Literature review

As introduced in Section 1.3, one core objective of this research is to estimate bottom hole temperature of injected CO_2 determining thermo-elastic stress, which is a key factor on fracture initiation and propagation. Therefore, wellbore heat transfer analytical model or numerical simulation is the necessary tool. The other objective is to estimate fracture growth and corresponding CO_2 migration, which couples both fracture modeling and flow dynamics in porous media. In the following, we will review previous work in these two areas.

2.1 WELLBORE HEAT TRANSFER MODELS

Temperature difference causes transfer of heat between different objects or different parts of an object (Lienhard IV et al., 2006). The heat transfer due to temperature difference between wellbore fluid and surrounding formations is the major part of total heat transfer in wellbore system (Hasan and Kabir, 2002). The importance of heat transfer related issues in petroleum industry results in extensive literature on this subject. As early as 1937 by Schlumberger et al., wellbore fluid temperature profile measurements were carried out. A theoretical model for estimating wellbore fluid temperature profile was first presented by Ramey (1962). For 50 years, engineers calculating wellbore heat transfer referred to this classical model. Ramey's formulation is simple and effective but with few limitations, such as only single-phase fluid can be handled. Moreover, in Ramey's model, wellbore heat transfer coefficient is independent of injection or production rate. Later methods have also been proposed to handle two-phase flow (Satter, 1965; Alves et al., 1992). The latest model by Hasan and Kabir (1994)

shows more complex two-phase flow model considering flow kinetic energy and frictional loss in wellbore.

On the other hand, commercial software in recent years, like PROSPER, can comprehensively address wellbore heat transfer problems for complicated situations. However, the cost and the complicated settings of wellbore model make it inconvenient for mass applications when wellbore information is scarce. Further, in PROSPER, heat transfer coefficient is set as a constant rather than a function of flow rate. The latter is important in the horizontal wellbore heat transfer problem.

Finally, published analytical model or software on heat transfer of horizontal wellbore is seldom seen. We fill in this gap in Chapter 4 by an analytical model for both uniform leak-off and non-uniform leak-off case.

2.2 INJECTION INDUCED FRACTURE

Injection induced fracturing widely occurs in water flooding and water re-injection work. It has been widely discussed in previous literature by both analytical models and numerical simulation approaches. Methods have evolved from early simple analytical modeling to recent flow performance and geomechanics coupled complicated simulation program. Numerical simulation allows more realistic description on problems than analytical and has a broadly applicable range.

As early as 1980, Hagoort et al. provided a semi-analytical model for predicting injection induced fracture propagation during water flooding. However, the most important factor, thermally induced stress was ignored and heat transfer between formation and injected fluid was not discussed. Then in 1985, Perkins and Gonzalez presented the famous three-region model by coupling flow performance with fracture

mechanics. This model has been highly cited in later water flooding induced fracture study (Saripalli et al., 1999; Suri et al., 2009; Rahman and Khaksar, 2012). However, almost no obvious improvement on this model has been proposed until Suri et al. (2010) introduced reservoir pressure transient model for fractured injector by Gringarten (1974). The analytical model assumes 1-D fracture growth with infinite conductivity and thus ignores width of fracture. Reservoir geomechanics properties variation due to injection cannot be simultaneously updated in this model. In other words, the fracture mechanics and reservoir flow dynamics are decoupled, which implies it is short of reality for providing precisely quantitative prediction of fracture growth. However, the advantage of this model is that it is simple and low cost for mass applications.

On the other hand, numerical simulation work on fracture propagation developed quickly. From early Settari (1980, 1988) simple decoupled approach, to one-way coupling simulation by Hustedt (2008), two-way coupling simulation by Ji (2007), and fully coupling approach by Chin (2000), these numerical approaches are computationally complex and time consuming. Especially, Rodrigues (2009) externally coupled commercial software STARS (reservoir simulator produced by CMG) and FLAC3D (geomechanics simulator produced by ITASCA) for dynamic fracture growth and flow performance simulation. This could be the most powerful but time consuming approach known.

In this work, we base on Perkins and Gonzalez model but improve it with various boundary conditions and add two-phase flow into the model through introducing Buckley-Leverett fractional flow theory in elliptical coordinate system. The details of this work will be discussed in Chapter 7.

Chapter 3 Injection induced stresses and criteria for injection induced fracture initiation

3.1 INTRODUCTION

As previous discussed in Chapter 1, in large-scale CO_2 sequestration, a huge amount of CO_2 is injected into formation at high rate over a long period of time. CO_2 would be transported along pipelines from power plants to injection well, then down the wellbore into the storage formation. Time for heat transfer between fluid and surrounding formations is very short when injection rate is high and thus temperature of injected CO_2 may be remarkably lower than that of formation. Therefore, CO_2 would cool the formation rocks.

This cooling effect can cause rocks to contract and can induce deformation (strain) of rock with cooler fluid in it near wellbore (Sadd 2009). This is referred to as injection induced thermo-elastic stress (Perkins and Gonzales et al., 1985; Garon et al., 1988; Clifford et al. 1991). Similarly, pore pressure change due to injection may induce poro-elastic stress in formation rock. These two types of induced stresses modify in-situ stresses in storage formation, which are the determinant factors of fracture initiation and propagation.

We categorize CO_2 injection projects to two classes based on tolerance of fracture occurrence at injection wells in storage formations: (I) fracture occurrence is rigorously forbidden in storage formations by regulators; (II) fractures are not forbidden but should be under control. For the first class, fracture criterion is studied based on the worst/most pessimistic case (criterion with lowest fracture initiation pressure), in which poro-elasticity is ignored. Because poroelasticity increases tangential stress at bore hole wall,

and partially compensating the effect of thermoelasticity on fracture initiation pressure, neglect of poro-elastic stress would result in lower criterion pressure for fracturing. Meanwhile, for the second class, we introduce a more practical and generic description, which accounts for the impact of poro-elastic stress that should be overcome if fracture grows.

In this chapter, we first introduce definitions of thermo-elastic stress and poro-elastic stress and then discuss the significance of two stresses at various injection strategies. After this, we deduce criteria for vertical and horizontal injectors at various circumstances with influence of the two stresses mentioned above. Finally, we discuss the influence of formation properties on fracture initiation criterion.

3.2 THERMO-ELASTIC STRESS AND PORO-ELASTIC STRESS

According to its definition in Eq. (3.1), thermo-elastic stress in tangential direction at borehole wall is linear to temperature change of formation rock, which is for intact borehole (Fjaer et al., 2008).

$$\Delta\sigma^T = \frac{\alpha_T E \Delta T}{1-v} \tag{3.1}$$

where $\Delta\sigma^T$ is thermo-elastic stress at borehole wall in Eq. (3.1), α_T is thermoelasticity coefficient, E is Young's modulus, v is Poisson's ratio, and ΔT is temperature difference between current state and initial state, as $\Delta T = T_{current} - T_{initial}$. This is a general form of thermo-elastic stress in 3-D isotropic condition. However, in early period of CO_2 sequestration project, when volume CO_2 cooled region is small, storage formation is confined by underburden and overburden formations in vertical direction. Strain only occurs in radial and tangential direction. Therefore, thermo-elastic stress only impacts in-situ horizontal stresses.

However, in the analytical stress expressions provided by Perkins and Gonzalez (1985) with injection induced fracture, thermo-elastic stress at fracture tip is affected by the geometry of cooling region in storage aquifer with finite thickness (Eq. 3.2).

$$\Delta\sigma^T = \frac{\alpha_T E \Delta T}{1-v} \bullet f(a_0, b_0) \tag{3.2}$$

In Eq. (3.2), $f(a_0, b_0)$ is geometry factor due to finite thickness of storage aquifer, a_0 and b_0 are half length of major axis and minor axis of cooled region by injected fluid, respectively (see in Fig. 7.3). For the application to CO_2 injection wells, the temperature difference of interest is between the storage aquifer and the CO_2 as it leaves the well (the flow bottom hole temperature). The latter is a strong function of injection rate because it depends on heat transfer between wellbore fluid and surrounding formations along the wellbore (see in Fig. 3.1). Similarly, we have poro-elastic stress at wellbore wall as (Biot, 1957),

$$\Delta\sigma^P = \alpha_p \Delta P \tag{3.3}$$

and with the effect of geometry of thermal front,

$$\Delta\sigma^P = \alpha_p \Delta P \bullet f(a_0, b_0) \tag{3.4}$$

when the poroelasticity at fracture tip is considered. Here poroelasticity coefficient is defined as, $\alpha_p = Biot \cdot \frac{1-2\nu}{1-\nu}$ (Hagoort et al., 1980; Fjaer et al., 2008), v is Poisson's ratio, *Biot* is Biot's number of formation (Biot, 1957), ΔP is pressure change between current state and initial state, as $\Delta P = P_{current} - P_{initial}$. ΔP is determined by injection rate, formation permeability, storage formation drainage radius, borehole radius, and formation thickness.

Considering formation temperature is declining and pressure is rising, thermo-elastic stress is negative and poro-elastic stress is positive. Therefore thermo-elasticity

and poro-elasticity have contrary effects on in-situ stresses. In the next section, we will discuss competition of the two effects at various CO_2 injection scenarios.

3.3 COMPETITION BETWEEN THERMO-ELASTICITY AND PORO-ELASTICITY

From the definitions of thermo-elastic stress and poro-elastic stress and injection/flooding mechanism, we know they may diminish effect of each other because of negative value of $\Delta\sigma^T$ and positive value of $\Delta\sigma^P$ in the expressions for fracture initiation pressure (Eq. (3.10)) and fracture propagation pressure (Eq. (7.5)). Large $\Delta\sigma^T$ decreases fracture initiation pressure, which is upper bound for injector bottom hole pressure. Hence, allowable maximum injection rate reduces in large $\Delta\sigma^T$ situation. In fracture growth process, large $\Delta\sigma^T$ lowers fracture propagation pressure and thus fracture propagates fast. Fig. 3.2 illustrates relative magnitude of each effect at different injection scenarios described in Table 3.1.

In Fig. 3.2, the dash blue line indicates the case with equal thermoelasticity and poroelasticity. We see thermoelasticity is dominant in most CO_2 injection cases in Table 3.1 with points below the dash line, as the pore pressure of borehole wall during CO_2 injection for sequestration purpose does not increase as high as that in energized fluid hydraulic fracture treatment. In Table 3.1, in the base column, $\Delta\sigma^T$ is almost four times of $\Delta\sigma^P$. In cases A and B, $\Delta\sigma^P$ is inversely linear to permeability. In case C, $\Delta\sigma^T$ shows proportional increase with Young's modulus (E). In case D, lowering injection rate results in smaller $\Delta\sigma^P$ and $\Delta\sigma^P$, but only $\Delta\sigma^P$ declining is linear to injection rate. In case E, high Poisson's ratio causes low α_P and thus low $\Delta\sigma^P$; meanwhile, according to definition of $\Delta\sigma^T$, reducing v means increasing $\Delta\sigma^T$. In case F by α_T increasing 50% as that for E in case C, it shows α_T plays the same role as E on $\Delta\sigma^T$. In case G, storage aquifer radius also

affects bottom hole pressure as well as $\Delta\sigma^P$. In case H, low α_P is the reason for low $\Delta\sigma^P$. In case I, gathering all factors can cause $\Delta\sigma^T$ increase and ignoring poroelasticity, the extreme high magnitude of $\Delta\sigma^T$ can reduce fracture initiation pressure from 15.6 MPa to 8.95 MPa for storage formation at 1000m depth.

From the above analysis, we can conclude several parameters, namely injection rate and Poisson's ratio, may both control $\Delta\sigma^T$ and $\Delta\sigma^P$. Table 3.1 could provide a general outlook about the competition between $\Delta\sigma^T$ and $\Delta\sigma^P$ for various injection scenarios. On the other hand, this table also guides the properties should be investigated for injection operation and site screening in CO_2 sequestration projects.

In the following section, we will compare influence of $\Delta\sigma^T$ and $\Delta\sigma^P$ on fracture initiation pressure. To simplify the study and estimate the possible lowest of fracture initiation pressure (the worst scenario), we ignore $\Delta\sigma^P$ and focus on the impact of $\Delta\sigma^T$ on fracture criterion and maximum safe injection rate.

3.4 BOREHOLE BREAKDOWN AND FRACTURE INITIATION CRITERION

The criteria for fracture initiation at an injection well can be understood from borehole stability analysis. In borehole stability analysis, we treat the well as a hole in an infinite plane as 2-D plane strain problem and predict maximum pressure at the bottom of injector to cause borehole breakdown. Stresses around borehole wall are instantaneously variable according to borehole pressure and temperature, where borehole is assumed initially intact. The stability of borehole depends on rock properties and borehole fluid pressure. Injection changes pressure and temperature of borehole wall, and thus in-situ stresses. If borehole fluid pressure causes effective tangential stress of borehole wall over rock tensile strength, tensile failure may occur.

3.4.1 Fracture initiation criterion on vertical well

As shown in Fig 3.3, it is the top view of borehole and surrounding formations for stress analysis. Here we only consider the initiation of Mode I fracture, tensile open fracture, in normal faulting stress regime ($\sigma_h<\sigma_H<\sigma_v$). We directly introduce the solution of tangential stress at borehole wall as the following (Fjaer et al., 2008),

$$\sigma_\theta = \sigma_H + \sigma_h - 2(\sigma_H - \sigma_h)cos2\theta - P_w \tag{3.5}$$

where P_w is borehole fluid pressure, θ is the angle measured from the direction of maximum horizontal stress, σ_θ is tangential stress at the borehole wall, σ_H and σ_h are maximum and minimum horizontal stress, respectively.

In Eq. (3.5), when θ equals 0 and 180^o, σ_θ at the two red labeled points at borehole wall in Fig. 3.2 have the minimum values as,

$$\sigma_\theta = 3\sigma_h - \sigma_H - P_w \tag{3.6}$$

The condition for fracture initiation compares effective tangential stress with rock tensile strength for open hole wellbore is(Fjaer et al., 2008),

$$\sigma_\theta - P_f \leqslant -\sigma_s \tag{3.7}$$

where σ_s is rock tensile strength, P_f is pore pressure at the borehole wall ($r=r_w$). Given permeability of storage formation is much higher than micro-darcy, storage formation is considered as fully permeable (Detournay and Cheng, 1992). This means pore pressure of borehole wall equals to borehole pressure ($P_f=P_w$). If Eq. (3.7) is satisfied, borehole would breakdown and fracture may initiate from borehole wall. With the sign convention in petroleum engineering, positive sign means compressive stress; while negative sign here means tensile stress.

As mentioned before, depending on regulatory tolerance on fractures in storage formation, the criteria can be separated to a rigorous one (no fracture initiation) and a flexible one (fracturing allowed). The rigorous one ignores poro-elastic stress ($\Delta\sigma^P$) contribution. Thermo-elastic stress is added to tangential stress (Eq. (3.6)) based on superposition principle since governing equations of bore hole stability analysis in 2-D plane strain problem are linear (Fjaer et al., 2008)

$$\sigma_\theta = 3\sigma_h - \sigma_H - P_w + \Delta\sigma^T \tag{3.8}$$

Rearranging Eq. (3.8), we obtain borehole breakdown and fracture initiation criterion for fully permeable formation as,

$$P_{frac}^T = \frac{3\sigma_h - \sigma_H + \Delta\sigma^T + \sigma_s}{2} \tag{3.9}$$

where P_{frac}^T is the upper bound of fluid pressure in the bottom hole which would cause a fracture initiate from borehole wall. The superscript T indicates that this pressure accounts for contribution of thermo-elastic stress.

On the other hand, if fracture is allowable in storage formation, a more practical fracture initiation criterion with consideration of poro-elastic stress is,

$$P_{frac}^T = \frac{3\sigma_h - \sigma_H + \Delta\sigma^T + \Delta\sigma^P + \sigma_s}{2} \tag{3.10}$$

in which poro-elastic stress is,

$$\Delta\sigma^P = \alpha_p \Delta P = \alpha_p (P_w - P_R) \tag{3.11}$$

where P_R is initial formation pressure.

In our work, the two criteria are applied in different analysis depending on the regulation of tolerance on fracture. For regulations that forbid fracture initiation, we estimate fracture initiation pressure (P_{frac}^T) based on the worst case, that is, using Eq. (3.9). This is a worst case because it neglects poro-elastic stress, which counterbalances the effect of thermo-elastic stress and raises the value of P_{frac}^T. For regulations that

permit fracture initiation and propagation, we use the practical borehole wall model and thus Eq. (3.10) determines the criterion for fracture initiation.

In the following study, for convenience, we assume formations for CO_2 storage is isotropic in horizontal direction, which means $\sigma_H = \sigma_h$. However, this assumption is not conservative to estimate lowest pressure for fracture initiation. We will discuss effect of anisotropy of formation in-situ stresses on pressure for fracture initiation in next section.

Under this assumption, minimum horizontal stress here is calculated from empirical data of the U.S. Gulf Coast region (Breckels and van Eekelen, 1982),

$$\sigma_h = 0.0053D^{1.145} + 0.46(P_f - P_{hydrostat}) \quad (D<3500 \text{ m}) \tag{3.12}$$

Fig. 3.4 provides a typical example of stresses and pressures versus depth in subsurface. Pore pressure and vertical stress are linear to formation depth while horizontal stress and nominal fracture initiation pressure are non-linear to depth. The relation between them is $\sigma_v > P_{frac} > \sigma_h > P_f$. In 1000m depth formation, nominal fracture initiation pressure is 15.6 MPa. From values of $\Delta\sigma^T$ and $\Delta\sigma^P$ in Table 3.1, it is clear that thermo-elastic effect is generically stronger than poro-elastic effect in CO_2 sequestration projects. Large thermo-elastic stress (case I in Table 3.1) could significantly decrease fracture initiation pressure (from 15.6 MPa to 9.0 MPa), which is the upper bound of bottom hole pressure. Pore pressure of at 1000m is 10.3 MPa which is even higher than bottom hole pressure. It is not hard to obtain the conclusion that fracture definitely initiates in that formation at current condition unless reducing injection rate to diminish impact of thermo-elastic effect.

3.4.2 Effect of anisotropy of horizontal stress on fracture initiation pressure of vertical injector

In normal faulting regime, σ_h is lower than σ_v and σ_H is higher than σ_h. However, the highest magnitude of σ_H could be as high as σ_v in more compressional environments (Zoback 2010). In that case, isotropic horizontal stress assumption for Eq. (3.9) would overestimate fracture initiation pressure for vertical injectors, which is upper bound of bottom hole pressure of injectors. Consequently, the evaluation may still result in injection induced fracture.

One such extreme case is as shown in Fig. 3.6 with $\sigma_H \approx \sigma_v$. Fracture initiation pressure reduces in formation with anisotropic horizontal stresses compared to that of isotropic case. The reduction increases with depth but the increasing speed declines. After a certain depth (2500m in this example), the reduction almost does not vary. It is not hard to conclude that the influence of anisotropy of horizontal stress is declining with depth to a certain magnitude after sufficient depth.

3.4.3 Fracture initiation criterion on horizontal well

By treating a vertical borehole as a two dimensional plane strain problem, we deduce fracture pressure for borehole wall tensile failure. Similarly, we could acquire borehole breakdown criterion for horizontal wellbore by replacing maximum principal stress (σ_H) in Eq. (3.9) and Eq. (3.10) with σ_v. In the following chapters for borehole breakdown analysis of horizontal injectors, we use the equation below by considering the worst case with no poro-elasticity,

$$P_{frac}^{T} = \frac{3\sigma_h - \sigma_v + \Delta\sigma^{T} + \sigma_s}{2} \tag{3.13}$$

where $\sigma_v = \int \rho_{fm} g z dz$, z is the depth of storage formation and ρ_{fm} is formation bulk density.

Nominal fracture initiation pressure of horizontal injector ($P_{frac,H}$) is lower compared with that of vertical injector ($P_{frac,V}$) in formation of any depth, as shown in Fig. 3.5. This implies the upper bound of bottom hole pressure of horizontal injector is lower than that of vertical injector even without impact of thermo-elastic effect. At 1000 m depth, the reduction is 2.5 MPa. Nevertheless, this case does not consider impact of thermo-elastic effect. The result will be totally distinct when thermo-elastic effect is considered in Chapter 5 and Chapter 6.

3.4.4 Influence of formation properties and operation parameters on fracture criterion

Here we use parametric analysis to discuss the range of rock properties and their influence on factors in fracture criteria. From fracture criterion Eq. (3.9), Eq. (3.10), and Eq. (3.16), we know that the determinant factors on fracture initiation pressure are σ_H and σ_h (or for horizontal wells σ_v and σ_h), $\Delta\sigma^T$, $\Delta\sigma^P$ and σ_s.

In Table 3.2, we summarize formation properties and operation factors affecting individual terms in the fracture criteria. Vertical principal stress σ_v depends on formation bulk density (ρ_{fm}) above storage formation and depth from surface to storage formation (D). To estimate horizontal stress, Eaton (1969) assumed rock is under linear elasticity theory and it is bilaterally constrained. In other words, there is no lateral deformation. We treat σ_h, σ_H, and σ_v as three principal stresses and they are mutually orthogonal. According to Hooke's law, we have

$$\sigma'_h = \frac{\nu}{1-\nu}\sigma'_v \tag{3.14}$$

where the prime symbol indicates effective stress is defined as $\sigma'_m = \sigma_m - p_f$.

The reason we only consider effective stress is that mechanics properties (E and ν) used here belong to rock framework. Moreover, physically the solid framework carries

the part σ' of the total stress, while the remaining part p_f is carried by pore fluid. Therefore, Hooke's law is applied to analyze stress-strain relation of rock framework. Although in this study, we actually calculate σ_h by empirical formula of the U.S. Gulf Coast area (Eq. (3.12)), the above model for estimating σ_h shows it is related to v, σ_v and P_f. Other authors, like Zoback (2010), provided critically stressed crust theory for estimating σ_h in other regions.

Determining factors for other terms of fracture criterion in Table 3.2 are easy to explain except $\Delta\sigma^T$. The determining factor for $\Delta\sigma^T$ is fairly complicated because it is proportional to ΔT, which is controlled by wellbore/earth heat transfer as CO_2 flows from wellhead to bottom hole. Details of heat transfer along wellbore will be described and discussed in Chapter 4. $\Delta\sigma^P$ is ignored for the worst case with no-fracture tolerance. However, when considering fracture propagation for cases with fracture allowance, bottom hole pressure should be high enough to overcome fracture initiation pressure with $\Delta\sigma^P$, in which ΔP is taken as the pressure change from P_R to P_w. σ_s is rock tensile strength, which directly determines rock fracture toughness. From literature we know that rock fracture toughness (K_{IC}) is linearly to rock tensile strength (σ_s). For rocks in Saudi Arabia, the proportional relation is with a factor of 0.3057 (Al-Shayea et al., 2001).

In the following chapters, we build models on heat transfer along wellbore to concretely discuss the influence of $\Delta\sigma^T$ on fracture initiation and propagation.

3.5 SUMMARY

Starting from two dimensional plane strain problem, we have analyzed borehole stability for vertical and horizontal CO_2 injectors for various injection circumstances. Depending on regulatory tolerance of fracture initiation from injection wells into a

storage formation, we built up two different criteria for fracture initiation, which would be applied in the following chapters as limitations to control injection rate and as startup condition for fracture growth. Influence of rock thermo-elastic is accounted for in the fracture criteria. Detailed parametric analysis points out related factors on each individual term in fracture criterion formula, which is the guide for sensitivity analysis and optimizations to improve safe injection rate in the following chapters.

Table 3.1: Injection operation parameters and aquifer properties

	base	A	B	C	D	E	F	G	H	I
k(md)	50	10	500	50	50	50	50	50	50	500
h(m)	30	30	30	30	30	30	30	30	30	30
Injection Rate(ton/d)	1000	1000	1000	1000	100	1000	1000	1000	1000	1000
r_e(m)	1000	1000	1000	1000	1000	1000	1000	10000	1000	1000
E(Gpa)	20	20	20	30	20	20	20	20	20	30
v	0.3	0.3	0.3	0.3	0.3	0.45	0.3	0.3	0.3	0.45
$\alpha_T\,(\mathrm{K}^{-1})$	1.0E-05	1.0E-05	1.0E-05	1.0E-05	1.0E-05	1.0E-05	1.5E-05	1.0E-05	1.0E-05	1.0E-05
α_P	0.45	0.45	0.45	0.45	0.45	0.17	0.45	0.45	0.35	0
ΔT(^{o}C)	-24.4	-24.4	-24.4	-24.4	-5.99	-24.4	-24.4	-24.4	-24.4	-24.4
ΔP(Mpa)	2.40	12.02	0.24	2.40	0.240	2.40	2.40	3.00	2.40	2.40
$\Delta\sigma^T$ (MPa)	-6.97	-6.97	-6.97	-10.46	-1.71	-8.87	-10.46	-6.97	-6.97	-13.31
$\Delta\sigma^P$ (Mpa)	1.08	5.42	0.11	1.08	0.11	0.41	1.08	1.35	0.84	0

Table 3.2 Determining factors for each term in fracture criterion

σ_v	D, ρ_{fm}
σ_h	$v,\ \sigma_v, P_f$
$\Delta\sigma^T$	$E, v,\ \alpha_T, \Delta T$
$\Delta\sigma^P$	$Biot, v, \Delta P$
σ_s	σ_s

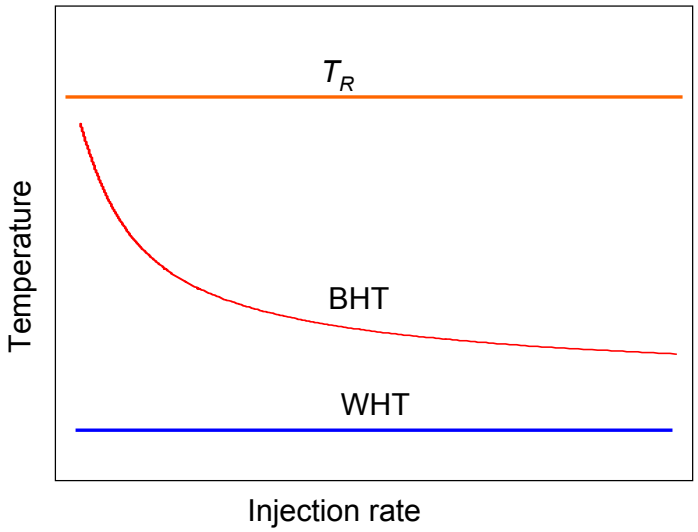

Figure 3.1: Injected CO_2 bottom hole temperature (BHT) is a strong function of injection rate. In comparison, WHT and T_R are well head temperature and formation temperature, respectively.

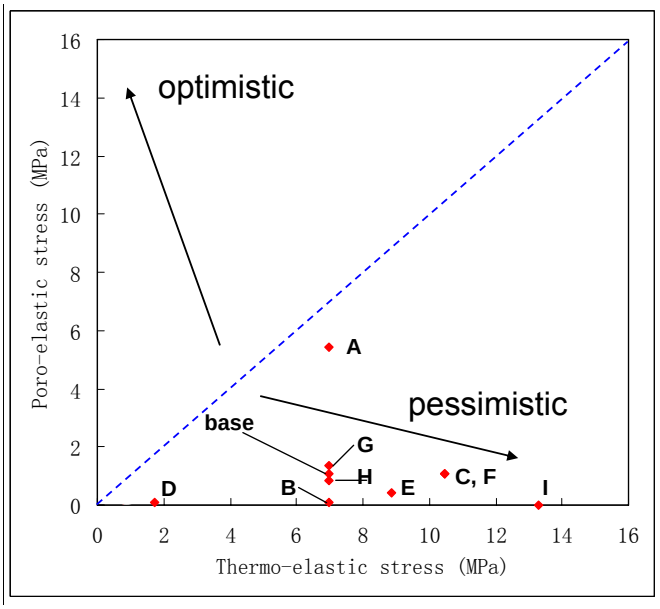

Figure 3.2: Thermo-elastic stress and poro-elastic stress at different injection scenarios given in Table 3.1. "Optimistic" means a larger threshold pressure for fracture initiation; while "pessimistic" indicates the opposite case.

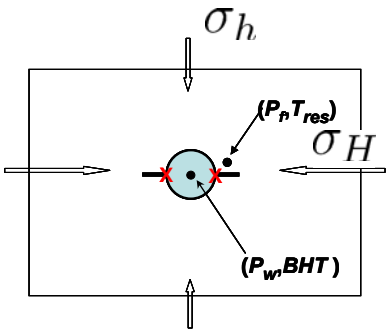

Figure 3.3: Top view of borehole and surrounding formation

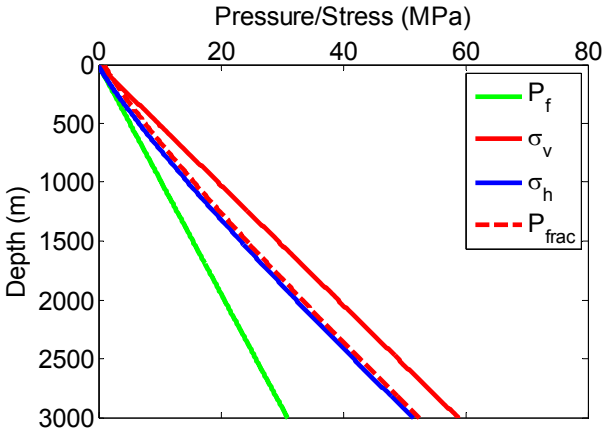

Figure 3.4: Stresses versus depth. Pore pressure (P_f) of this formation is hydrostatic and pore fluid density is 1.05 g/cm^3; the formation belongs to normal faulting regime and bulk density (ρ_{fm}) of formation is 2.0 g/cm^3; minimum horizontal stress (σ_h) is calculated as formation in the U.S. Gulf coast area; P_{frac} is nominal fracture initiation pressure for vertical injector. Here we consider rock tensile strength (2 MPa) in fracture initiation pressure.

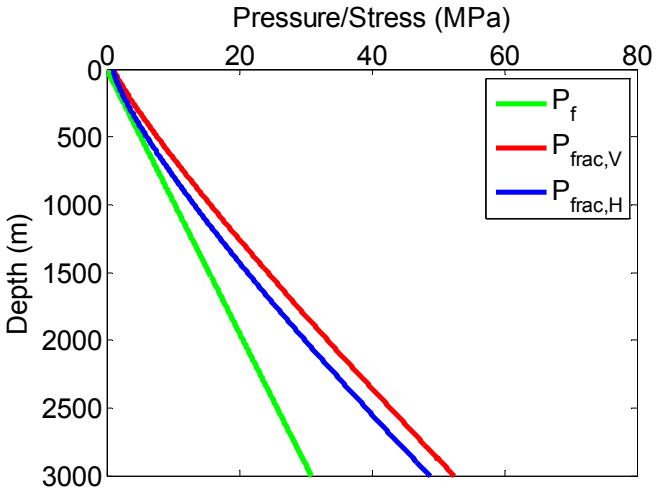

Figure 3.5: Fracture pressure for vertical injector and horizontal injector. The properties for calculation are referred as Fig. 3.4.

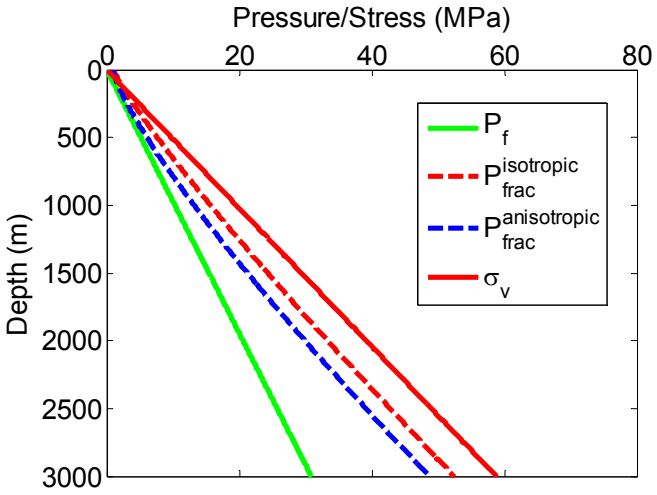

Figure 3.6: Comparison of fracture initiation pressure of formation with isotropic horizontal stress and extreme anisotropic stresses ($\sigma_H \approx \sigma_v$). Other formation properties are referred as Fig. 3.4.

Chapter 4 Wellbore Heat Transfer Model

4.1 INTRODUCTION

From the analysis in last chapter, we know that thermo-elastic stress ($\Delta\sigma^T$) is a major determinant factor in fracture initiation criterion. Temperature change in near wellbore formation (ΔT) is essential to $\Delta\sigma^T$. In this chapter, models of heat transfer between wellbore fluid and surrounding formation has been built to estimate temperature change due to injected fluid at bottom hole.

We first built heat transfer model for vertical well with constant injection rate by setting overall heat transfer coefficient of entire wellbore to a constant. After this simplest case, we consider more realistic case with dynamic injection rate, including a case taken from real operations. In this circumstance, overall heat transfer coefficient is a function of injection rate. The model assumes that fluid properties do not change drastically along wellbore, and in this case both dimensional analysis and field measurements show that overall heat transfer coefficient depends only on injection rate. Further, by applying regression on those measurements, power law correlation between mass injection rate and overall heat transfer coefficient has been found for wide scale of injection rate. The correction could be applied either for vertical injector with dynamic rates or for horizontal injector with flow rate variation along wellbore.

By extending the above model to horizontal lateral, we can estimate temperature profile for horizontal injector from surface to the toe of horizontal well. As horizontal laterals are entirely or partially perforated, flow rate along wellbore is variable and thus heat transfer coefficient is not constant in this model. For horizontal wellbore, two types of wellbore fluid leak-off model are discussed: (i) uniform leak-off along perforated

wellbore; (ii) non-uniform leak-off along perforated wellbore. However, due to low viscosity of CO_2, friction is not very important and thus only uniform leak-off model is considered for discussions in further chapters.

4.2 VERTICAL WELLBORE HEAT TRANSFER MODEL

As shown in Fig. 4.1, when CO_2 flows along wellbore, it transfers heat with surrounding formations due to temperature difference. To evaluate the range of thermo-elastic stress during CO_2 storage, it is useful to consider the bounds on temperature profile $T(z)$, the temperature of the CO_2 as a function of its depth z in the wellbore. The bounds correspond to two limiting cases of heat transfer between wellbore fluid and surrounding formations.

The upper bound of the temperature profile along wellbore is formation geothermal profile. This bound applies when heat transfer between CO_2 in the well pipe and surrounding formation is very fast compared to the flow rate. In this case, temperature change in the storage formation due to CO_2 injection is zero and thus there is no influence of thermo-elastic effect to fracture initiation pressure.

The lower boundary of CO_2 temperature profile can be determined by assuming an adiabatic process during injection. In an ideal adiabatic process, there is no heat exchange with surrounding formations and the specific entropy of the fluid does not vary with depth in the wellbore. Hence, the temperature change is only due to enthalpy change from wellhead to well bottom. To describe the ideal adiabatic process, we can assume heat transfer coefficient equals zero in the governing equation, described below. This adiabatic assumption can approximately describe the heat transfer process when the injection rate is sufficiently high and heat transfer coefficient of the equipment is

relatively small. It must be emphasized that adiabatic state is different from isothermal state; because of potential energy changes, it is possible for the temperature of CO_2 to change from wellhead to bottom hole in the adiabatic case.

4.2.1 Heat transfer model with static flow rate

As CO_2 is injected and stored in supercritical state, a single phase flow model is proper to describe CO_2 flow and heat transfer in the wellbore. We assume no radial temperature gradient in the fluid within the wellbore and we ignore friction losses. Applied to this process the energy balance reads (Hasan and Kabir, 1994),

$$\Delta H + \Delta\left(\frac{mv^2}{2}\right) - \Delta mgz - \Delta Q = 0 \tag{4.1}$$

or for a differential element of fluid,

$$\frac{d\hat{H}}{dz} = \frac{d\hat{Q}}{dz} + g - v\frac{dv}{dz} \tag{4.2}$$

where H, v, m, and z are enthalpy, average velocity, mass of control volume, depth of an element of CO_2 in the wellbore, respectively, Q is heat transferred between CO_2 and surroundings, and the caret ^ indicates a specific quantity (per unit mass). The heat transfer process can be described as,

$$\frac{d\hat{Q}}{dz} = -\frac{2\pi r_w U}{\dot{m}}\left(T(z) - T_{fm}(z)\right) \tag{4.3}$$

where U accounts for the radial flux of heat through the tubing containing CO_2, and the successive annuli of completion fluid, casing, mud, cement etc. to the surrounding formation, r_w is wellbore radius, T_{fm} is surrounding formation temperature, and $\dot{m}$ is mass injection rate. Both T and T_{fm} are functions of depth. We take $T_{fm} = T_{fm}(0) + Gz$ where $T_{fm}(0)$ is surface temperature, and G is geothermal gradient.

By ignoring the small change in kinetic energy in Eq. (4.2) and using the definition of enthalpy per mass $\hat{H}$,

$$d\hat{H} = c_p dT \tag{4.4}$$

then substituting Eq. (4.3) into Eq. (4.2) and combining Eq. (4.4), we obtain

$$\frac{dT}{dz} = \frac{2\pi r_w U\left(T_{fm} - T\right)}{c_p \dot{m}} + \frac{g}{c_p} \tag{4.5}$$

Specific heat capacity (c_p) of CO_2 is a function of pressure and temperature and thus it varies with position in the wellbore. For conditions typical of CO_2 storage, the variation is not dramatic from well head to well bottom. As shown in Fig. 4.2(a), ρ-T-P diagram shows the path of typical T and P variation along a wellbore (solid black line presents the value of ρ) does not cross many contours. The value of ρ within the wellbore can be approximated with a constant for depths as great as 2000 m. We thus use an average value of ρ in the model. Specific heat capacity of CO_2 (c_p) has c_p -T-P similar contour diagram in Fig. 4.2(b) and thus average density is used in this model.

By setting $U = 0$ as the adiabatic process, the solution of Eq. (4.5) at depth D is

$$T(D) = T(0) + \frac{g}{c_p} D \tag{4.6}$$

Although no heat is exchanged along the wellbore path, the gravity term in Eq. (4.2) increases the enthalpy of the fluid when it flows from the wellhead to well bottom. From Eq. (4.6), we can see the temperature is not constant with depth. Thus the assumption of an isothermal temperature profile, though convenient, is not a valid approximation of the adiabatic limit.

For nonzero heat transfer coefficients, the solution to Eq. (4.5) at depth D is:

$$T(D) = (T(0) - T_{fm}(0) - \frac{g}{c_p}\frac{r_w}{2\beta} + \frac{Gr_w}{2\beta})e^{-\frac{2\beta D}{r_w}} + \frac{g}{c_p}\frac{r_w}{2\beta} - \frac{Gr_w}{2\beta} + T_{fm}(0) + GD \tag{4.7}$$

Here β is the dimensionless ratio of the rate of heat transfer to the rate of advective transport of enthalpy defined as $\beta = \frac{\pi r_w^2 U}{c_p \dot{m}}$, as known as Stanton number.

Since the value of β is very small in CO_2 injection process, to facilitate the following of analysis, we modify it by multiplying a dimensionless number for fixed depth D as

$$\beta' = \left(\frac{\pi r_w^2 U}{c_p \dot{m}}\right)\left(\frac{2D}{r_w}\right) = \frac{2\pi r_w U D}{c_p \dot{m}} \tag{4.8}$$

From now we will use β' instead of β in the following analysis for fixed depth cases. We specify temperature difference at depth D as $\Delta T = T_{fm}(D) - T(D)$ and temperature difference at surface $\Delta T(0) = T_{fm}(0) - T(0)$, then we have temperature difference at depth D with dimensionless form,

$$\frac{\Delta T}{\Delta T(0)} = (1 - \frac{\alpha}{\beta'})\exp(-\beta') + \frac{\alpha}{\beta'} \tag{4.9}$$

also ΔT is expressed as,

$$\Delta T = (T_{fm}(0) - T(0))\left[\left(1 - \frac{\alpha}{\beta'}\right)e^{-\beta'} + \frac{\alpha}{\beta'}\right] \tag{4.10}$$

where $\alpha = \frac{G - g/c_p}{T_{fm}(0) - T(0)} D$ is a dimensionless temperature gradient.

4.2.2 Sensitivity of bottom hole temperature

To illustrate, we assume the depth of storage aquifer is 1000 m (the minimum depth for storage is conventionally set at 800 m where pressure and temperature could be above the point of supercritical state of CO_2), which will be set for the following parametric analysis on temperature profile and temperature difference ΔT. Among all parameters in Eq. (4.10), G, r_w, and c_p are fixed and others are contained in β'. Moreover, we know the magnitude of ΔT, and correspondingly of $\Delta\sigma^T$, is mainly related to D, β', and $\Delta T(0)$. In the following, the influence of the three parameters will be discussed.

(i) Depth (D)

In Eq. (4.10), the only term relevant to depth is the exponent term containing β' in index. With depth increasing, the exponential term declines and asymptotically trends to a constant. Thus the temperature profile $T(D)$ gradually trends toward and finally parallels to the formation geothermal profile $T_{\mathrm{fm}}(D)$ after certain depth no matter its initial temperature at wellhead, as shown in Fig. 4.3. In other words, for sufficiently deep formations the temperature difference between fluid and storage formation becomes independent of depth. The definition of 'sufficiently deep' depends on the other parameters; the higher the value of injection rate, the greater the 'sufficient depth'.

(ii) β'

This dimensionless parameter is Stanton number (β) at fixed depth D, which contains the influence of U and $\dot{m}$. From next section, we would know that U is a function of $\dot{m}$ under certain assumptions in CO_2 sequestration projects. Therefore, to reduce the number of study parameter, we only consider the influence of $\dot{m}$ on ΔT. The value of ΔT is sensitive to $\dot{m}$, as depicted in Fig. 4.4. Consider a target storage formation at a depth of 1000 m with an injection well of fixed values of r_w. Since c_p is set with average value as a constant (as discussed in section 4.2.1), β' will vary inversely with $\dot{m}$ (as shown in Fig. 4.13 (b)). For pilot test with low injection rate (several metric tons per day), ΔT is nearly zero. At very high injection rate, ΔT will over 25°C. Consequently, ΔT is likely to be over 30°C. For commercial storage rates, β' is between 0.2 and 2 and ΔT is between 15 °C and 30°C.

(iii) $\Delta T(0)$

This parameter is the difference between surface temperature $T_{fm}(0)$ and CO_2 temperature at well head $T(0)$. Often $T(0)$ is lower than $T_{fm}(0)$ and thus $\Delta T(0)$ is positive. However, if CO_2 is pre-heated before injection, $\Delta T(0)$ could be negative. As shown in

Fig. 4.5, without pre-heating, $T(0)$=15°C, and ΔT at bottom hole monotonically increases with injection rate increasing and β' decreasing (blue curve). If CO_2 is preheated to 30°C, then ΔT keeps monotonicity but the increasing rate is not as high as the former case. If we pre-heat CO_2 to 45°C before injection, ΔT (green curve) shows non-monotonic behavior. At low injection rate with β' larger than 1.7, ΔT increases with injection rate as for the other cases. But at high injection rate with β' less than 1.7, ΔT decrease with increasing injection rate. This unique result implies that ΔT is even lower with high injection rate if CO_2 is preheated to threshold temperature. In that case, CO_2 transfers heat to surrounding formations at the beginning portion of wellbore. Therefore, the higher the injection rate, the shorter time for CO_2 transfers heat and the less heat loss to surrounding formations. As a result, ΔT is lower.

On the other hand, the three curves coincide for low injection rate (large β'). This means heat exchange is fast enough to at low injection rate no matter its initial temperature. In this situation, the value of the exponent term trends to zero and the second term in Eq. (4.9) determines ΔT. Since the second term does not contain $\Delta T(0)$, the value $\Delta T(0)$ is not relevant on ΔT at small injection rates.

4.2.3 Relation between heat transfer coefficient and injection rate

A steady-state heat transfer model with constant (independent of depth) heat transfer coefficient (U) can accurately describe temperature profile of vertical injector with constant injection rate ($\dot{m}$). The appropriate value of the heat transfer coefficient for a wellbore must be inferred from field data, but the main assumptions of the model appear reasonable at a fixed injection rate. The model (Fig. 4.1) can calculate bottom hole temperature (BHT) and apply the value to predict thermo-elastic stress in near wellbore

formations. However, in field operations, injection rate often varies with time and with storage strategies. Hence, a model with single value of heat transfer coefficient for all flow rates is not enough accurate to predict BHT. In this section, we deduce from classic dimensional analysis theory the relation between heat transfer coefficient and injection rate, as $U = U(\dot{m})$. This correlation is not only applied in vertical injector with dynamic injection rate but also to improve horizontal wellbore heat transfer model. Because CO_2 flows through perforation holes along horizontal wellbore, mass flow rate in the wellbore decreases from heel to toe. Hence, along horizontal segment of wellbore, U becomes a function of position, assigned a value based on the local mass flow rate.

It is helpful to apply classic dimensional analysis on heat transfer to anticipate the form of the correlation between U and $\dot{m}$. From the definition of Nusselt number, $\mathrm{Nu} = \frac{UD}{k}$, where D is diameter of wellbore and k is thermal conductivity of the injected CO_2, we have $U = \frac{\mathrm{Nu} \cdot k}{D}$. Nusselt number for flow in a pipe may be written as (Sieder, 1936), $\mathrm{Nu} = \mathrm{Nu}(\mathrm{Re}, \mathrm{Pr}, L/D, \mu_b/\mu_0)$. Reynolds number ($Re$) and Prandtl number ($Pr$) are defined as,

$$\mathrm{Pr} = \frac{c_p \mu_0}{k}, \quad \mathrm{Re} = \frac{\rho \langle v \rangle D}{\mu_0} \tag{4.11}$$

where the fluid properties c_p, ρ, μ_0, μ_b, $\langle v \rangle$ are specific heat capacity, bulk density of injected CO_2, viscosity at bulk fluid temperature, viscosity at wellbore boundary temperature, mean flow velocity in wellbore, respectively. In our model, CO_2 fluid bulk temperature is assumed equal to wellbore boundary temperature, so $\mu_b = \mu_0$. We finally may obtain heat transfer coefficient (U) as a function of

$$U = U(c_p, L/D, \mu_b, \mu_0, k, D, \rho, \langle v \rangle) \tag{4.12}$$

For typical injected conditions and geothermal gradients, the pressure-temperature path for CO_2 flow in wellbore does not cross boundaries on the CO_2 phase diagram (as

show in Fig. 4.2). Thus our model assumes single phase of supercritical state CO_2 fluid from wellhead to bottomhole (Lindeberg, 2011). As we discussed in section 4.2.1 there is no large variation of properties of CO_2 and we can use average values for density, viscosity, heat conductivity and specific heat capacity. Therefore, $c_p, L/D, \mu_b, \mu_0, k, D, \rho$ are constants for a given injector and the only variable for typical operating conditions is flow mean velocity in wellbore $\langle v \rangle$, where $\langle v \rangle = \frac{4\dot{m}}{\pi D^2 \rho}$. Hence, heat transfer coefficient is only a function of mass injection rate, i.e. $U = U(\dot{m})$.

Measurements of heat transfer in smooth circular tubes with nearly constant wall temperature for highly turbulent flow show an empirical power law relation between Nu (contains *U*) and Re (contains $\dot{m}$) with exponent value 0.8 (Re > 20,000), the relation being (Sieder, 1936)

$$\mathrm{Nu} = 0.026\,\mathrm{Re}^{0.8}\,\mathrm{Pr}^{1/3}\left(\frac{\mu_b}{\mu_0}\right)^{0.14} \tag{4.13}$$

4.2.4 Calibrations of heat transfer model for dynamic flow rate

Here we apply field measurements of a CO_2 injector in Cranfield, Mississippi to inversely run wellbore heat transfer model to acquire the correlation between overall heat transfer coefficient and injection rate. By incorporating the correlation in our model, we can estimate bottom hole temperature of injector with dynamic rate. Further, we successfully validate the updated model with measurements (Luo and Bryant 2012).

Before enter the procedure for data processing, we first talk about the source of CO_2 injection well data measurements, which are from Denbury Resources Inc courtesy of GCCC (Gulf Coast Carbon Center). As shown in Fig. 4.6 (a), CO_2 injector CFU 31 F1 is in the Detailed Area of Study (DAS) at Cranfield in southwest Mississippi. Fig. 4.6 (b) illustrates the sketch of vertical CO_2 injector CFU 31 F1. Parameters of CFU 31 F1 and

the model are listed in Table 4.1. This injection well is instrumented with a continuously operating downhole temperature gauge placed 108 ft above perforated interval between 10,450 ft and 10,506 ft depth. Flow rate is measured at a gauge 12 ft upstream of the wellhead at ten minutes interval and the wellhead temperature is taken from a flow line temperature gauge 52 inches above ground level at the top of second section of wellhead.

In this Cranfield injector, *Re* is from 81,000 to 430,000, which belongs to highly turbulent flow. Thus from Eq. (4.13) we expect an almost first-order dependence of U on $\dot{m}$ to emerge from the data.

Following Eq. (4.13), a power law function with exponent 0.8 was fit to the inferred values of U and the measured values of $\dot{m}$. In the following section, we will discuss this correlation and its influence on BHT predictions.

4.2.4.1 Work flow of acquiring correlation

The process to obtain correlation between U and $\dot{m}$ is illustrated as flow chart in Fig. 4.7. The data logging at Cranfield occurs at different intervals for different sensors. Measurements of injection rate, wellhead temperature (WHT) and BHT at common times were extracted into a single file. These were used with the heat transfer model to determine the values of U that would be consistent with the measurements. Repeating this inverse modeling at each measurement time yields a large set of values U and $\dot{m}$. Under the assumption that overall heat transfer coefficient depends only on mass flow rate, we then examine power function regressions between the values of U and $\dot{m}$. We then run the model in forward mode, calculating BHT from measured WHT and $\dot{m}$ using U calculated from the empirical formula. The computed BHT is then compared with measured BHT to determine how much error the empirical correlation introduces. In all

cases, the correlation produces much better results than the assumption that U is independent of flow rate.

By re-arranging Eq. (4.7), we have solution of BHT as,

$$BHT = (T(0) - T_{fm}(0) - \frac{g}{c_p}\frac{\dot{m}}{\pi DU} + \frac{Gc_p\dot{m}}{\pi DU})e^{-\frac{\pi DLU}{c_p\dot{m}}} + \frac{g}{c_p}\frac{\dot{m}}{\pi DU} - \frac{Gc_p\dot{m}}{\pi DU} + T_{fm}(0) + GD \qquad (4.14)$$

where $T_{fm}(0)$, g, G, D are formation temperature at surface, acceleration due to gravity, geothermal gradient, and wellbore length. In this work we treat Eq. (4.14) as an implicit equation for the unknown U for each measurement of BHT, WHT and $\dot{m}$.

4.2.4.2 Power law correlation and heat transfer model validation

The data of CO_2 injector CFU 31 F1 used here are provided by Denbury Resources Inc. We investigated the data gathered between 2009-6-25 and 2011-2-8. Over this period CO_2 was injected at rates varying from 100 to 1000 ton/d.

In Fig. 4.8, we first compare the measurement to the BHT predicted from the heat transfer model with constant U. We consider two values of U (13 W/m^{2}K and 20 W/m^{2}K) in this exercise. Clearly neither value of U can match the measurements for the entire range of injection rate. This is consistent with expectation above that U is a function of injection rate. The difference between prediction and measurement can be over 10^{o}C when the injection rate is changed by a factor of 4, as occurred on 2010-12-11 (red oval in Fig. 4.8). Since typical differences between BHT of injected fluid and formation temperature are a few tens of degrees Celsius, an error of ten degrees is non-negligible.

11953 pairs of ($U, \dot{m}$) data with injection rate range from 100 ton/D to 1000 ton/D were collected by inversely running the wellbore heat transfer model for regression analysis (Fig. 4.7). Most of values of U fall between 5 and 25 W/m^{2}K. Although outliers exist (associated with the relaxation time after step changes in flow rate), the trend of

increasing U with increasing flow rate is clear, and for the purposes of our application quantifying that trend is the main goal. Due to the uneven distribution of data points at different injection rate, we need to unify the weight of U corresponding to different $\dot{m}$. By setting bins of width 1 ton/d, we average all values of U for flow rates in each bin and use this averaged U for the regression analysis with $\dot{m}$ (Fig. 4.9). Considering the format of power law function from dimensional analysis, we set the format of fitting function as $U = b\dot{m}^{0.8} + c$. As shown in Fig. 4.9, we obtain a reasonable fit with b = 0.0795 and c = 5.3963.

We input the above correlation with WHT and injection rate measurements to steady-state model as Eq. (3.14) to predict BHT and compare with corresponding measurements. As shown in Fig. 3.10, the black line indicates predictions equal to measurements. Two red lines give bounds for 2^{o}C errors and two green lines give bounds for 5^{o}C errors. Blue points show the relative accuracy between prediction and measurements. Most points are inside the 2^{o}C bounds except some points within the green oval. Those points are selected from the zone with large injection change as shown in the big red oval of Fig. 4.8. Since the steady-state model responds instantaneously to injection rate change, it overestimates the BHT for a few hours until the transients decay. Statistically, in histogram figure (Fig. 4.11), we see 68.3% predictions are within 1^{o}C of the measurement and cumulatively 87.6% is within 2^{o}C error. In total 99.5% predictions are within 5^{o}C error.

In sum, this work establishes and analyzes correlations between overall heat transfer coefficient and CO_2 injection rate into a vertical well using field measurement of CO_2 injector CFU 31 F1 in Cranfield field. Accounting for the fact that larger flow rates cause larger overall heat transfer coefficients enables a steady-state heat transfer model to predict BHT of vertical CO_2 injector much more accurately when the injection rate varies

substantively (a factor of two or more). Assuming a power-law dependence on flow rate taken from process engineering (i.e. exponent 0.8) gives a reasonably good correlation for flow rates between 100 ton/D and 1000 ton/D. Over 87% of predictions with this correlation and a steady state model are within 2°C of measurements. Therefore, it is confident to say the correlation and our heat transfer model is accurate enough to capture temperature response to dynamics injection rate.

4.3 HORIZONTAL WELLBORE HEAT TRANSFER MODEL

In this section, we first introduce the model used to calculate temperature profile along horizontal segment of wellbore, and then discuss temperature difference between wellbore fluid and formation at typical injection strategies.

4.3.1 Model introduction

As shown in Fig. 4.12, an injector wellbore is separated to a vertical and a horizontal segment with different models. Temperature difference between wellbore fluid and surrounding formations exists in both segments. Steady-state assumption is applied for fluid flow in entire wellbore. The base case for horizontal segment of wellbore model is open hole or entire wellbore perforated (Luo and Bryant, 2011).

The model includes two cases, uniform flux through perforation and non-uniform flux through perforation. For uniform leak-off flux case, wellbore pressure of horizontal segment is constant and flow rate inside wellbore ($\dot{m}$) linearly declines from maximum rate at heel to zero at toe of horizontal well, as

$$\dot{m} = \dot{m}_0(1 - x/L) \tag{4.15}$$

For non-uniform leak-off flux case, which arises usually because of high viscosity of fluid or high flow rate in wellbore, there is a pressure drop between heel and toe. Thus, flow rate ($\dot{m}$) is non-linearly declines from maximum rate at heel to zero at toe.

4.3.1.1 Uniform flux through perforation

In horizontal segment of wellbore, fluid flux from wellbore into formation is assumed uniform along the perforated zone as injected fluid is low viscous Newtonian fluid if wellbore is not too rough (Joshi, 1991). Hence, bottom hole pressure in the horizontal well is constant. Bottom hole pressure is calculated by Borisov's model (1984).

Temperature at the heel of horizontal segment is assumed equal to bottom hole temperature of vertical wellbore model in section 4.2.1. This is reasonable for wells constructed with a small build radius between segments. By introducing the improved model with heat transfer coefficient as a function of mass injection rate from section 4.2.4.2, we have temperature difference at the heel of horizontal wellbore as in Eq. (4.10). Considering the flow rate variation in horizontal segment of wellbore, overall heat transfer coefficient is a function of flow rate thus it varies along wellbore. Here, we use the correlation as in Fig. 4.9,

$$U = 0.0795\dot{m}^{0.8} + 5.3963 \tag{4.16}$$

an empirical correlation regressed from Cranfield measurements with injection rate between 100 and 1000 ton/d in Section 4.2.3. We assume the extrapolation of this correlation is valid for injection rate from 1000 to 10,000 ton/d (Fig. 4.13(a)). The exponent of 0.8 in Eq. (4.16) makes Stanton number β' a weak function of injection rate

at large rates, and β' has a fairly narrow range from 0.25 to 2 for injection rates greater than 100 ton/d (Fig. 4.13(b)).

To describe the steady state balance between advection of heat along the wellbore and radial transfer of heat from the surroundings into the wellbore along the horizontal section, we use the equation:

$$\frac{dT}{dx} = \frac{2\pi r_w U\left(T_R - T\right)}{c_p \dot{m}(x)} \tag{4.17}$$

Compared with the one for vertical well in Eq. (4.5), we can see in this horizontal heat transfer model, $\dot{m}$ is no longer constant and T_R instead of T_{fm} is constant. Because of no depth change of horizontal segment, gravity term disappears.

As flow rate within the wellbore decreases from heel to toe, overall heat transfer coefficient also decreases according to the above empirical correlation (Eq. (4.16)). As U has the format of $U = b\dot{m}^{0.8} + c$, Eq. (4.17) can be written as,

$$\frac{dT}{dx} = \frac{2\pi r_w b\left(T_R - T\right)}{c_p \dot{m}_0^{0.2}(1 - x/L)^{0.2}} + \frac{2\pi r_w c\left(T_R - T\right)}{c_p \dot{m}_0 (1 - x/L)} \tag{4.18}$$

By solving Eq. (4.18), we have

$$\Delta T(x_D) = T_{res} - T(x) = \left(T_{fm}(0) - T(0)\right)(1 - x_D)^{\frac{2\pi r_w cL}{c_p \dot{m}_0}} \cdot \left[\left(1 - \frac{\alpha}{\beta'}\right)e^{-\beta'} + \frac{\alpha}{\beta'}\right]\exp\left\{\frac{5}{2}\frac{\pi r_w bL}{c_p \dot{m}_0}\left[(1 - x_D)^{0.8} - 1\right]\right\} \tag{4.19}$$

The process of acquiring the solution of Eq. (4.17) is attached in Appendix A.

4.3.1.2 Non-uniform flux through perforation

Here we consider the non-uniform flux due to friction losses that reduce pressure inside of wellbore along with distance. This case may not occur in CO_2 injection due to fluid properties and injection strategies. However, we here briefly provide the solution for

temperature profile along horizontal segment of wellbore, in which the derivation process is provided in Appendix A.

When the injection rate is very high or the radius of the wellbore is small, the Reynolds number (*Re*) of flow in the horizontal well is very large. In this condition, we cannot ignore the friction loss along the wellbore, especially when fluid is viscous, like gel. Friction loss causes pressure gradient along the wellbore; if we assume that the reservoir pore pressure does not vary along the wellbore, then the flux of fluid into the reservoir is no longer uniform. In this model, we assume the entire wellbore is perforated. The wellbore fluid pressure near the heel would be higher than that near the toe of the horizontal well, which implies that the flux near the heel is higher than that near the toe. The heat transfer along the wellbore is strongly coupled with the non-linear mass flow rate. Hence, the temperature profile in non-uniform flux model differs from that in uniform model. The solution of temperature profile along horizontal well for non-uniform flux model is from the Appendix A,

$$\Delta T(x_D) = T_R - T(x) = \exp\left[-\left(\frac{2\pi r_w bL}{c_p \dot{m}_0^{0.2}} \int_0^{x_D} \frac{dx_D}{\dot{m}_D^{0.2}(x_D,\gamma)} + \frac{2\pi r_w cL}{c_p \dot{m}_0} \int_0^{x_D} \frac{dx_D}{\dot{m}_D(x_D,\gamma)} \right) \right] \cdot \left[\left(1 - \frac{\alpha}{\beta'} \right) e^{-\beta'} + \frac{\alpha}{\beta'} \right] \left(T_{fm}(0) - T(0) \right) \tag{4.20}$$

where γ is dimensionless friction factor of entire horizontal wellbore as $\gamma = \dfrac{2fk_H \dot{m}_0 L^2}{\pi \mu r_w^5 \left[\dfrac{L}{h} \ln \dfrac{4r_{eH}}{L} + \ln \dfrac{h}{2\pi r_w} \right]}$ and f is the conventional friction factor for flow along the horizontal section of the wellbore. The dimensional symbol expression of γ can be $\dfrac{[\mathrm{L}]^2[\mathrm{M/T}][\mathrm{L}]^2}{[\mathrm{M/(LT)}][\mathrm{L}]^5}$, therefore γ is dimensionless.

4.3.2 Parametric analysis of temperature profile along horizontal wellbore

In this section, we study the sensitivity of temperature difference between injected CO_2 and formation rocks based on uniform flux model. After combining factors related to $\Delta T(x)$ in partial dimensionless format (Eq. (4.19)), we finally find only two factors, such as β (Stanton number of vertical segment of wellbore) and L (length of horizontal segment of wellbore), are determinant to ΔT.

(i) β'

We know β' decreases with increasing injection rate (Fig. 4.13(b)) at fixed r_w, D, c_p. Here, we select three values of β' (2, 1, and 0.5) by changing injection rate (100 ton/d, 292.9 ton/d, and 1048 ton/d) in Fig. 4.14 to investigate its influence on the temperature difference profile along horizontal wellbore. In all cases, wellhead temperature is set as $T(0)=15^oC$ and other properties are listed in Table 4.2. For each case, the largest temperature difference occurs at the heel of horizontal wellbore ($x_D = 0$). The results also show that ΔT in various cases are not linearly declining along wellbore and decline patterns of each curve are different. At low injection rate (100 ton/d, β'=2), $\Delta T(x)$ falls faster near the heel of horizontal wellbore; while the blue curve (1048 ton/d, β'=0.5), $\Delta T(x)$ falls slowly until a sudden drop at the final segment of horizontal wellbore near toe with high injection rate. The dimensionless analysis on impact of β' implies $\Delta T(x)$ could be small only when β' is large in two cases: (1) low injection rate; (2) deep storage formation.

(ii) L/D

The influence of horizontal wellbore length (L) is shown by the ratio of L/D with fixed β' in Fig. 4.15 for uniform flux model. When β' is low (β'=0.1), corresponding to high injection rate, almost entire wellbore is under high temperature difference (over 10^oC) no matter the length of wellbore; while β' is high (β'=10), corresponding to low

injection rate, temperature difference of each case has almost the same distribution no matter the length of wellbore. Only when β' is at medium value (β'=1), temperature difference pattern shows distinction for each wellbore with different length.

As β'=1 stands for the typical injection scenario, we focus on Fig. 4.15 (b). With horizontal wellbore length increasing (*L/D* increase from 0.5 to 2.0), the absolute length of wellbore above 10°C increases (from 340m to 480m) while the proportion decreases (0.68 to 0.24). Physically, it implies that the longer the horizontal wellbore, the longer part with high temperature difference with surrounding formations, corresponding to thermo-elastic stress.

4.4 JOULE-THOMSON COOLING EFFECT ACROSS PERFORATIONS

When CO_2 flows through the perforations in the casing, if the injection rate is sufficiently high, there is a large pressure drop between the inside and outside of the casing. The influence of Joule-Thompson effect is significant when CO_2 is injected to depleted natural gas field, in which CO_2 expands into depleted reservoir with low pressure (Mathias and Oldenburg, 2010). The expansion of CO_2 may induce a reduced temperature near injection wellbore. This effect is independent of the arrival of cool CO_2 at the perforations, modeled in Sections 4.1-4.3 of this chapter. In this study, saline aquifers are considered as storage formation, where the pressure is approximately at hydrostatic level, in contrast to depleted gas reservoirs. The following study is conducted to test Joule-Thomson effect at different operation strategies.

The calculation of pressure drop due to flow of CO_2 through a perforation is based on the formula by Kraemer (1959)

$$\Delta P_{perf} = 0.00012 \rho v_p^2 \tag{4.21}$$

The flow velocity through a perforation hole v_p is calculated according to the flow rate ($q=\dot{m}/\rho$) balance between perforation holes and wellbore,

$$q = v_p A_{p,tot} = v_{bh} A_w \tag{4.22}$$

where A_w, $A_{p,tot}$ and v_{bh} are wellbore cross-section, total perforation hole area, and flow velocity, $v_{bh} = q/A_w$. The perforation area per foot (A_p) is the product of a single perforation hole area and the perforation density (shots per foot), and $A_{p,tot} = A_p h_p$, where h_p is the length of perforated wellbore.

Due to the short distance of flow path in the holes, we can assume flow in the perforation holes as an isenthalpic process (no change in kinetic energy and no work done). During this process, the temperature of real gas will decrease (Burnett, 1910). This is a Joule-Thomson expansion process and the temperature drop can be calculated from the definition of Joule-Thomson coefficient,

$$\Delta T_{perf} = \mu_{JT} \Delta P_{perf} \tag{4.23}$$

where $\mu_{JT} = 0.9$ K/atm (Table VII of Burnett, 1910).

For the example storage formation and wellbore of Table 4.2, the Joule-Thomson cooling effect is appreciable only at very high injection rate (10000 ton/D), small diameter of perforation holes (1/8 inch diameter), and low perforation density (4 shots/foot) about 6^{o}C. By increasing the diameter of perforation holes and the density of perforation holes, it is easy to minimize Joule-Thomson cooling at a target injection rate for this example (Fig. 4.16).

4.5 SUMMARY

In this chapter, we build heat transfer models to calculate bottom hole temperature for various injection scenarios. The difference between storage formation temperature

and bottom hole fluid temperature is the base for calculating thermo-elastic stress around wellbore. By the heat transfer model for a vertical injector, we first bound temperature profile of fluid in wellbore with two extreme cases, adiabatic profile limit and geothermal profile limit. From parametric analysis with typical injection project conditions, we test three dominant factors on bottom hole temperature difference: as formation depth (D), Stanton number (β), and wellhead temperature difference ($\Delta T(0)$). Temperature difference decreases with storage depth increasing, until a critical depth then it trends to a constant. The critical depth depends on other parameters, like Stanton number. Stanton number, which indicates the ratio of the rate of heat transfer to the rate of advective transport of enthalpy, decreases as injection rate increases. Larger Stanton number yields smaller temperature difference. Wellhead temperature has a first order influence; pre-heating fluid before the wellhead can reduce or even entirely cancel temperature difference at bottom hole, which could substantially increase maximum injection rate as discussed in Chapter 5 and Chapter 6.

In heat transfer model for horizontal injector, we apply uniform leak-off flux model to describe CO_2 injection process along perforated/open horizontal segment. The three factors in the analysis of vertical wellbore also control temperature at heel of horizontal wellbore, at which temperature difference has the highest value along the whole horizontal segment. Additionally, length of horizontal well as the key factor for temperature profile along horizontal segment has been studied. In sum, the longer the horizontal wellbore, the longer part with high temperature difference along wellbore.

The influence of dynamic injection rate of vertical injector or variable flow rate of horizontal injector on heat transfer efficiency has been investigated theoretically by dimensional analysis and empirically by regression of measurements from Cranfield

injection. Empirical power law correlation with exponent 0.8 between heat transfer coefficient and injection rate gives a reasonable heat transfer model for CO_2 injector.

Joule-Thomson cooling effect has been studied for CO_2 injection and storage in saline aquifer. The analysis shows that temperature drop can be ignored or avoid if injection rate for typical injection operation.

In the following two chapters we will analyze and optimize strategy to maximize injection rate under no-fracture safe regulation.

Table 4.1: Conditions for Injection Well

Wellhead temperature, WHT	27.2 °C - 40.5 °C
Well bottom temperature, BHT	computed or measured
Earth surface temperature, $T_0(0)$	15 °C
Geothermal gradient, G	33 °C/km
Wellbore diameter, d	0.16 m
Heat transfer coefficient, U	computed
Thermal conductivity of CO_2, k	0.10-0.12 W/m·K
Viscosity of CO_2, μ	4.6×10^{-5} Pa·s
Mean density of CO_2, ρ	800 kg/m^3
Mean heat capacity of CO_2, C_p	2500 J/kg·K
Mean flow velocity in wellbore, $\langle v \rangle$	computed from flow rate
Length of wellbore, L_w	10486 ft

Table 4.2: Conditions for Vertical Injection Well

Wellhead temperature, $T(0)$	15 °C
Wellhead pressure, P_{WH}	7.0 MPa
Earth surface temperature, $T_{fm}(0)$	20 °C
Geothermal gradient, G	30 °C/km
Wellbore radius, R	0.1 m
Young's modulus, E	30 GPa
Poisson's ration, v	0.45
Thermoelasticity coefficient, α_T	1.5×10^{-5} K^{-1}
Heat transfer coefficient, U	20 $W/m^2\cdot K$
Formation thickness, h	40 m
Formation permeability, k	100 md
Formation depth, D	1000 m
Length of horizontal well, L	1000 m
CO_2 viscosity, μ	4.6×10^{-5} Pa·s
Drainage radius, r_e	2000 m
Skin factor, s	1.0
Mean density of CO_2	800 kg/m^3
Mean heat capacity of CO_2	2500 J/kg·K

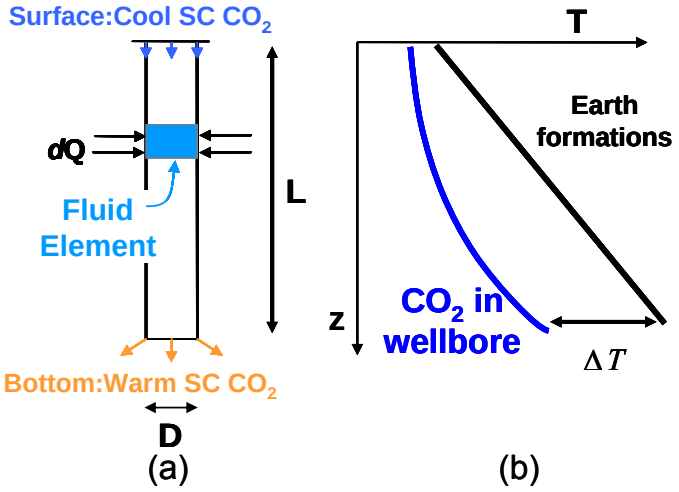

Figure 4.1: (a) Steady-state heat transfer model of vertical CO_2 injector. At wellhead cool supercritical (SC) CO_2 is injected and then CO_2 fluid is being heated along the wellbore. When CO_2 fluid arrives bottom hole, it is warmer than at wellhead but still cooler than formation rocks. (b) Temperature profiles in the earth and in the wellbore.

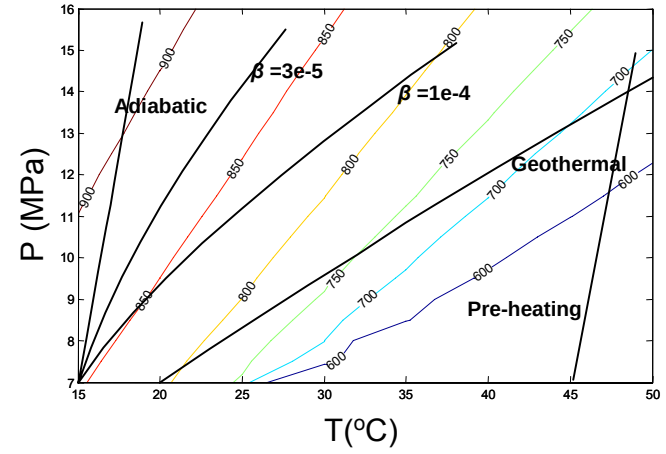

(a)

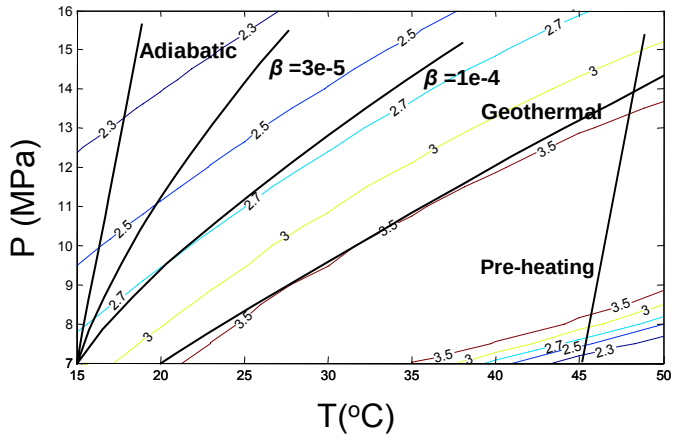

(b)

Figure 4.2: (a) Variation of ρ of pure CO_2 for temperature and pressure range from well head to well bottom; (b) variation of c_p of pure CO_2 for temperature and pressure range from well head to well bottom; model parameters are given in Table 4.2 and data are from NIST. The black solid curves are the paths (T, P) of CO_2 fluid in injection wells with various β. This shows c_p does not change dramatically in this study. The units of ρ and c_p are kg/m^3 and kJ/(kg-K), respectively.

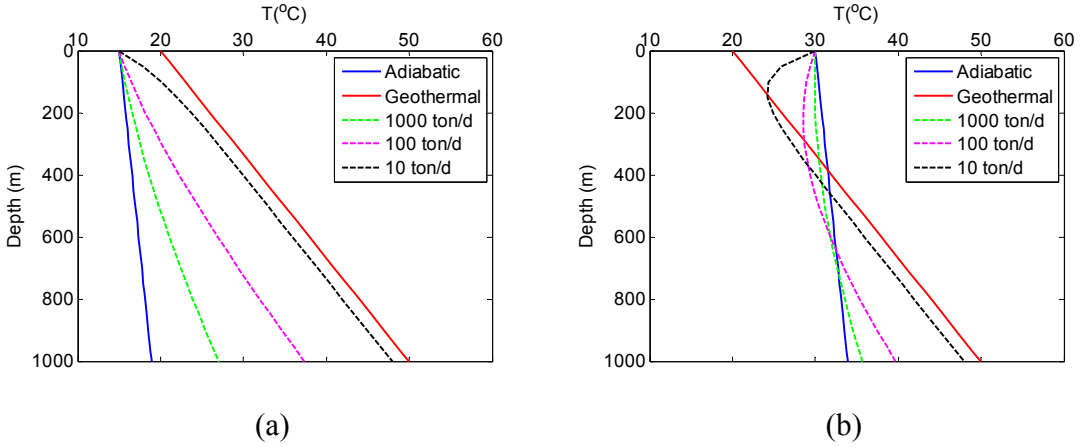

Figure 4.3: Temperature profiles of the model at different injection cases: (a) $T(0)$=15 °C < $T_{fm}(0)$=20 °C; (b) $T(0)$=30 °C > $T_{fm}(0)$=20 °C. Model parameters are given in Table 4.2.

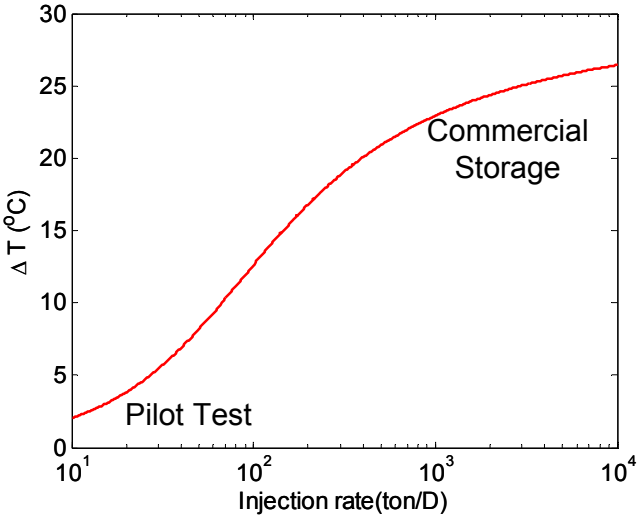

Figure 4.4: ΔT variation with injection rate at 1000 m depth storage formation. For pilot test injection, injection rate is low and ΔT is small, which means thermo-elastic stress is correspondingly low. At commercial scale with high injection rate, ΔT could be as high as over 25°C. This means thermo-elastic stress is relatively high and cannot be ignored. Model parameters are given in Table 4.2.

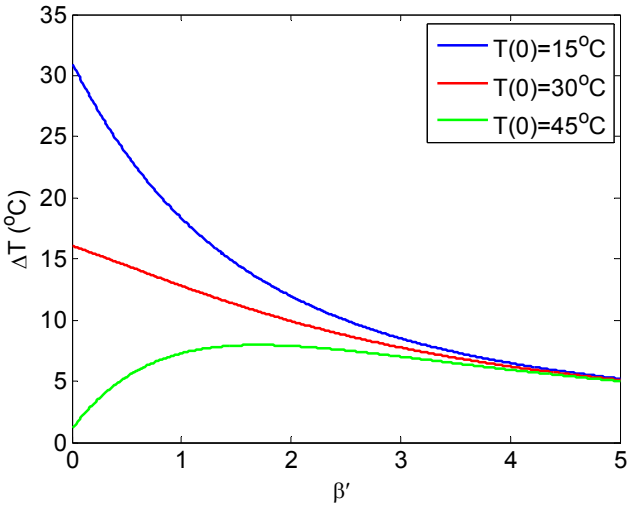

Figure 4.5: Temperature difference at bottom hole versus Stanton number at 1000 m depth (β') of vertical well at different wellhead temperature. Model parameters are given in Table 4.2.

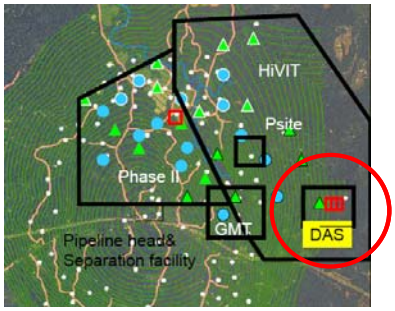

Location-Data Analysis Study (DAS)

(a)

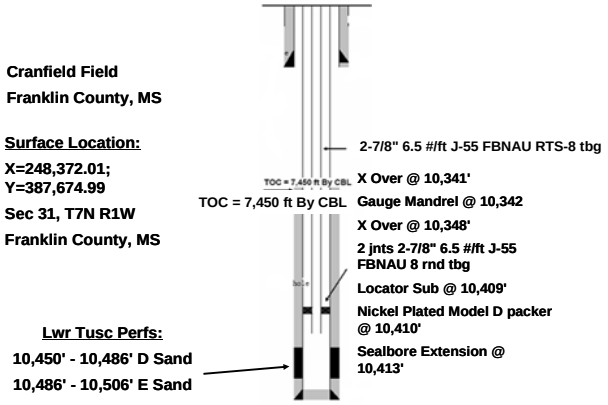

(b)

Figure 4.6: (a) Location of Cranfield and CO_2 injector CFU 31 F1 in DAS district at Cranfield; (b) CFU 31 F1 CO_2 injector sketch.

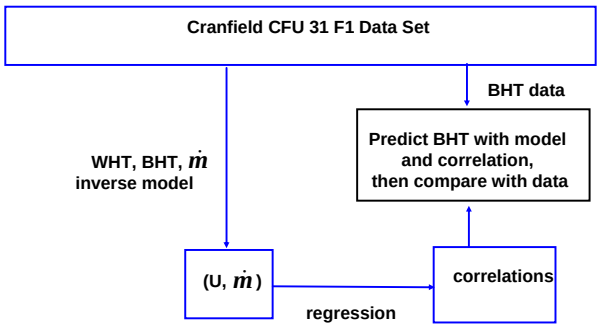

Figure 4.7: Flow chart of calculating heat transfer coefficient as a function of mass injection rate.

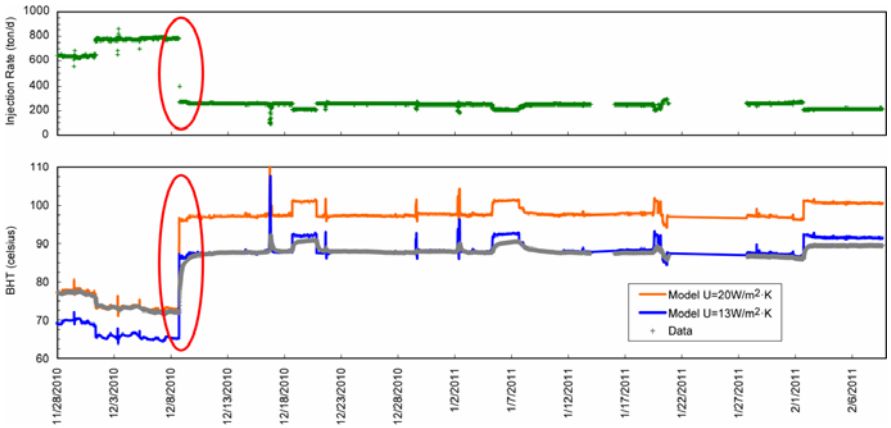

Figure 4.8: Inaccurate BHT prediction by model with overall heat transfer coefficient U assumed independent of flow rate; data from CFU 31 F1 CO_2 injector at Cranfield DAS (cf Fig. 4.6). Red ovals show the variations of injection rate corresponding to the variation of BHT. The prediction by model with U=13 W/m^2·K can only match low injection region and U=20 W/m^2·K can only match high injection rate region.

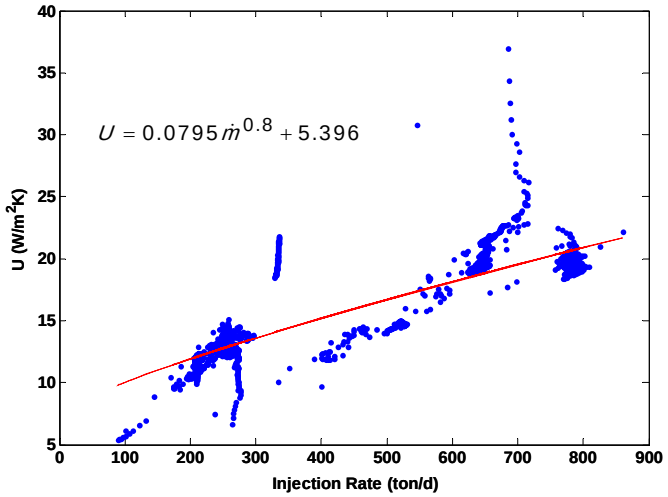

Figure 4.9: Power function correlation between mass injection rate and overall heat transfer coefficient inferred from steady-state model and BHT measurements of well CFU 31 F1. To weight the measurements uniformly with respect to injection rate, we set bins with injection rate 1 ton/d and average the values of heat transfer coefficients of data points in each bin.

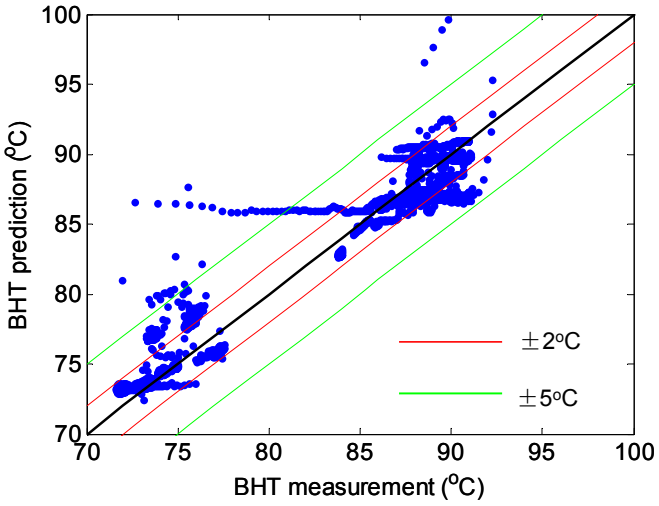

Figure 4.10: Comparisons of BHT predictions with BHT measurements. Red lines bound the errors of 2°C and green line bound the errors of 5°C. The group of points within green oval are transients after sudden large injection rate changes, which our steady state model fails to capture.

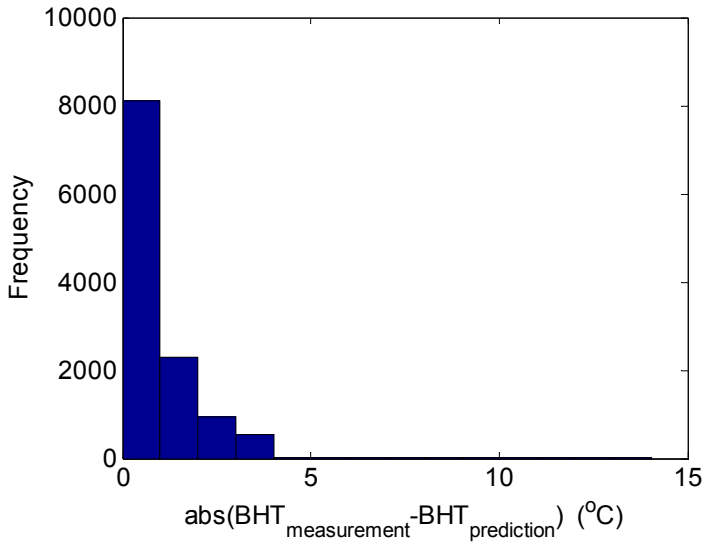

Figure 4.11: Histogram of absolute difference between BHT measurements and BHT predictions using steady state model with power law correlation (cf. Fig. 4.9)

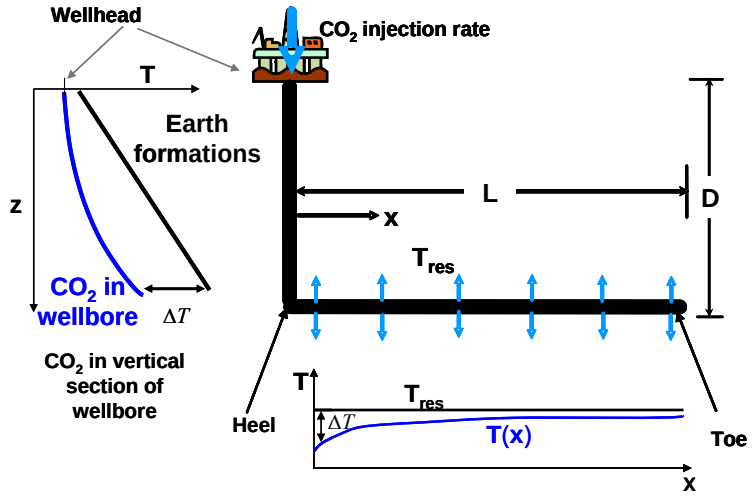

Figure 4.12: Sketch of horizontal CO_2 injection well with uniform flux into formation

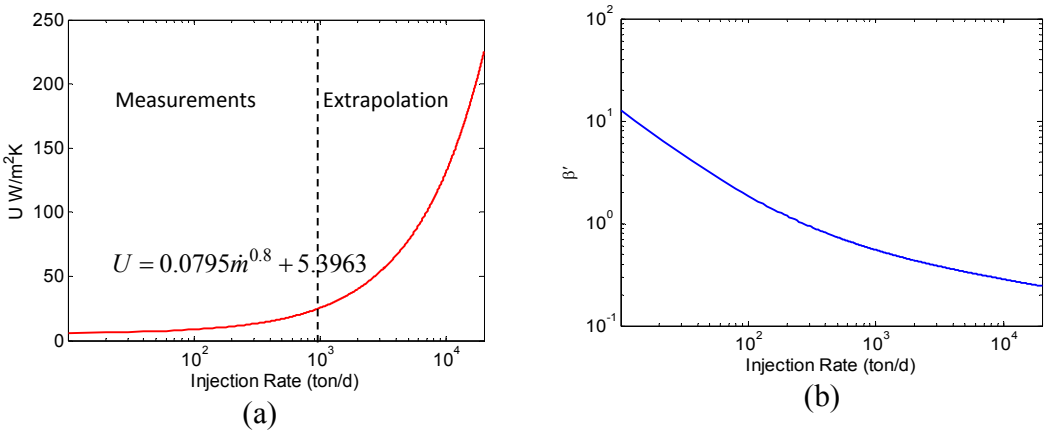

Figure 4.13: (a) heat transfer coefficient as a power law function of injection rate by regression of Cranfield measurements from 100 to 1000 ton/d; (b) Stanton number of 1000-meter deep vertical section of the well (β') versus mass injection rate based on correlation in (a). Model parameters are given in Table 4.2

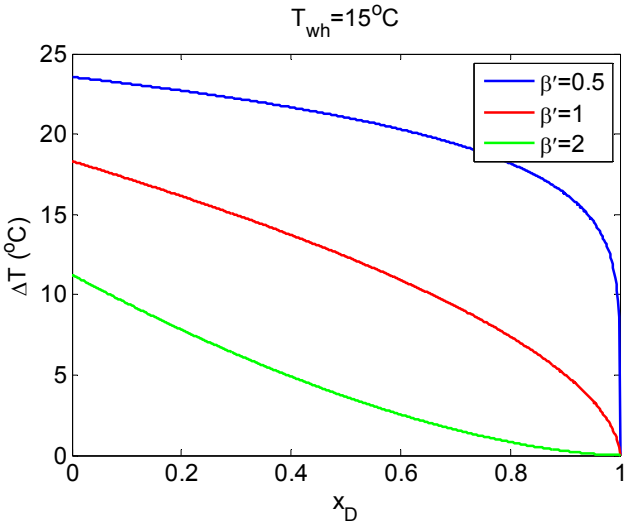

Figure 4.14: Temperature difference along horizontal wellbore at various Stanton number (β') for a 1000 m-deep vertical section of the well: β'=2 (100 ton/d); β'=1 (292.9 ton/d); β'=0.5 (1048 ton/d). Model parameters are given in Table 4.2.

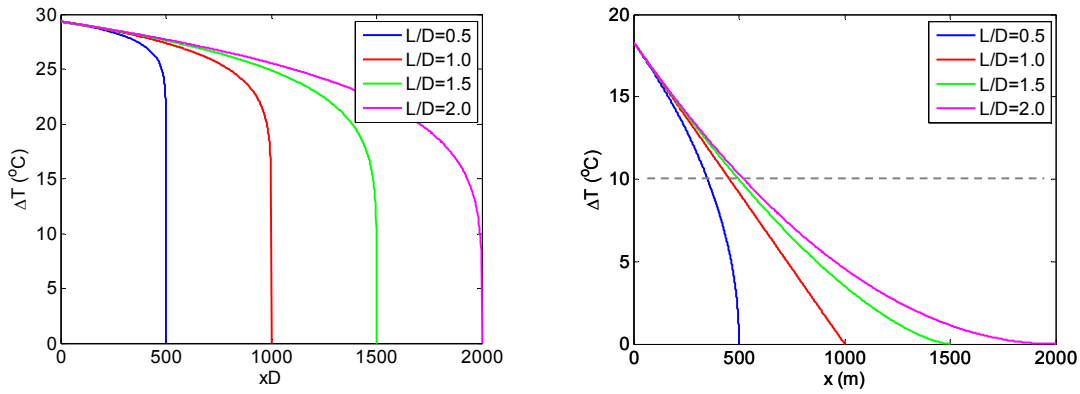

(a) β'=0.1 (b) β'=1

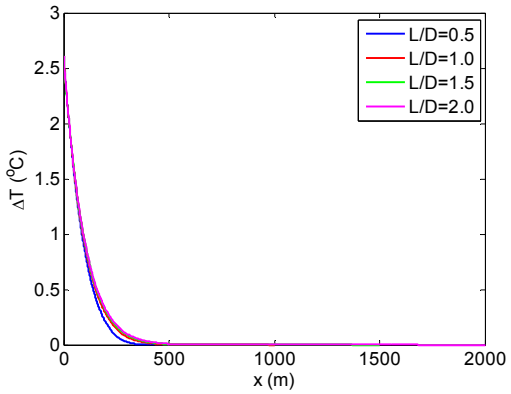

(c) β'=10

Figure 4.15: Sensitivity of ΔT profiles along horizontal wellbore with uniform flux model to L/D for several values of Stanton number (β') in 1000m-deep formation. Model parameters are given in Table 4.2.

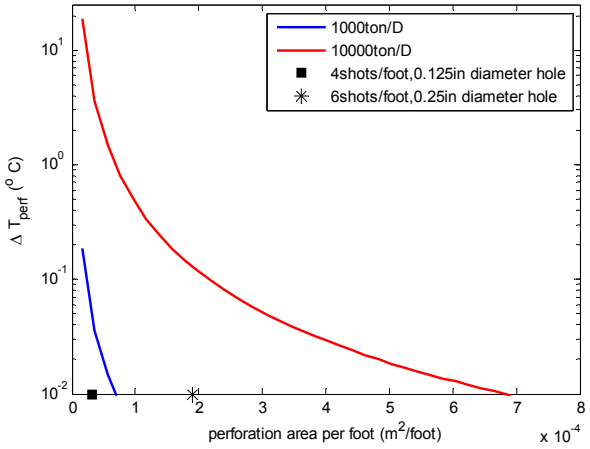

Figure 4.16: Temperature drop due to Joule-Thomson effect in perforation holes for the well and formation parameters of Table 4.2. Only with large injection rate (10000 ton/D) and small perforation area (4 shots/foot and 1/8 inch diameter of perforated hole, black square on x-axis), the temperature drop is as high as 6 °C

Chapter 5: Influence of injection induced fractures initiation on vertical well injection

5.1 INTRODUCTION

Considering the cost and technical convenience, vertical injectors have been widely used in most CO_2 sequestration projects. To avoid unpredictable leakage events during injection and storage, some regulators have zero tolerance on fracture initiation. In this chapter, we apply the conservative fracture initiation criterion in chapter 3, ignoring poro-elastic stress, to evaluate maximum safe injection rate into a vertical well, which is determined by bottom hole pressure and fracture initiation pressure.

Based on vertical wellbore heat transfer model in chapter 4, we can accurately estimate temperature difference between bottom hole fluid and formation rocks, given the injection rate and the geothermal gradient. We can then estimate the corresponding thermo-elastic stress in formation rocks and the resulting reduction in the fluid pressure needed to initiate a fracture in the formation. Consequently, fracture initiation pressure is set as the upper bound for bottom hole pressure, which is standard to calculate maximum safe injection rate. Besides studying the limitation of fracture initiation pressure, we also investigate the influence of various reservoir properties and injection operations on bottom hole pressure.

It is important to screen out storage sites which have good geological conditions for large-scale high rate CO_2 injection and storage projects. Parametric analysis is very useful to storage site screening under no-fracture regulation. The analysis in this chapter also provides several optimizations to overcome the impact of thermo-elastic effect, such as deep formation storage and pre-heating at surface, to improve injection rate for

satisfying requirements of large-scale CO_2 commercial sequestration. Among these options we find pre-heating CO_2 before injection is the most effective and feasible way to realize high injection rate. In this study, energy consumption on pre-heating is estimated.

5.2 IMPACT OF INJECTION INDUCED FRACTURE ON MAXIMUM INJECTION RATE

To keep the number of equations consistent, we recall Eq. (3.9), the conservative criterion for fracture initiation, and write it here as Eq. (5.1),

$$P_{frac}^{T} = \frac{3\sigma_h - \sigma_H + \Delta\sigma^T + \sigma_S}{2} \tag{5.1}$$

To calculate bottom hole pressure of CO_2 injector, we consider long time injection process as steady state. When the CO_2 is injected into a brine-saturated formation, three regions arise and travel outward wellbore radius direction, such as pure CO_2, brine and CO_2 mixture, and pure brine. Brine and CO_2 mixture region displaces brine region because of fractional flow and CO_2 region displaces two-phase region because of CO_2 dissolved in irreducible brine.

The fluid mobility in each region is different (Burton *et al*., 2008). To simplify the calculation of bottom hole pressure, we treat the injection as an equivalent single phase steady state flow, using an effective viscosity (μ_{eff}) to account for entire CO_2-brine system. Because of the size variation of three regions due to CO_2 migration, the effective mobility of the entire region is increasing as Burton tested. We take the value when mobility is almost stable (2.5 cp^{-1}) and take an effective relative permeability of 1.0 by assuming single phase flow. Then the effective viscosity is 0.4cp. As viscosity is function of pressure and temperature, which vary with depth, effective viscosity varies with depth.

By steady-state flow model, bottom hole pressure is

$$P_w = P_{res} + \frac{\dot{m}\mu_{eff}}{2\pi\rho kh}\ln\left(\frac{r_e}{r_w}\right) \tag{5.2}$$

where P_{res} stands for far field reservoir pressure and also means initial reservoir pressure; ρ is CO_2 density in subsurface; r_e is storage reservoir radius and r_w is wellbore radius.

We know when bottom hole pressure P_w is equal or higher than fracture initiation pressure, fracture may be induced due to injection. The mathematical equation of this criterion is expressed in Eq. (5.3),

$$P_w = P_{frac}^T \tag{5.3}$$

Eq. (5.3) is a non-linear transcendental equation of $\dot{m}$, which is hard to solve analytically. The left hand side is linear to $\dot{m}$ (Eq. (5.2)), while the right hand side is implicitly related to $\dot{m}$ by $\Delta\sigma^T$ (Eq. (5.1)), which is non-linear to $\dot{m}$. Here we obtain the engineering solution by observing the intersection of two curves, $P_w(\dot{m})$ and $P_{frac}^T(\dot{m})$. The obtained pressure is fracture initiation pressure which is also upper bound of bottom hole pressure. Correspond to this pressure, the injection rate is maximum injection under no-fracture regulation.

As shown in Table 5.1, to investigate factors which affect maximum injection rate ($\dot{m}$), we consider parameters of rock mechanics perspective in Eq. (5.1) and of reservoir flow performance perspective in Eq. (5.2) respectively. To simplify the analysis, we assign typical values of those parameters used for this analysis; these are shown in Table 5.2.

(i) Young's Modulus (E)

Young's modulus of formation is a determinant factor on thermo-elastic stress which severely reduces fracture initiation pressure as analyzed in chapter 3. In Fig. 5.1, P_w rises and P_{frac} is constant. However, P_{frac}^T, decreases rapidly at low injection rate due to the rapid increase in ΔT as flow rate increases, resulting in rapid increase in thermo-elastic stress. This is caused by the non-linear relation between bottom hole temperature difference (ΔT) and injection rate ($\dot{m}$) as discussed in Chapter 4 (in Fig. 4.4). At rate

above 2000 ton/d, ΔT almost keep stable (Fig.5.1(b)) and thus P_{frac}^{T} curve is almost parallel to each other, which means the difference between each P_{frac}^{T} does not rise with injection rate any more. Comparing formations with distinct Young's modulus (*E*), the three red solid curves P_{frac}^{T} decrease with *E* increasing. As discussed the solution of Eq. (5.3), intersections between the P_{frac}^{T} curves and the P_w curve stand for the upper bound of bottom hole pressure and corresponding maximum safe injection rate for each injection case. Comparing maximum injection rate of the four intersections in Fig 5.1(a), thermo-elastics stress causes the maximum safe injection rate to decreases from nominal value 6300 ton/d to 4100 ton/d, 2070 ton/d, or 663 ton/d corresponding to formation Young's modulus 10 GPa, 20 GPa, and 30 GPa respectively. The values of Young's moduli taken here are in the range of typical values of sandstone (Fjaer et al., 2008). Physically, the influence of thermo-elastic effect becomes stronger in formation with higher Young's modulus and thus maximum injection rate is largely limited. This result implies that sites with formation rock of high Young's modulus are less desirable if injection induced fractures are not allowed in CO_2 sequestration projects.

(ii) Poisson's ratio (v)

In Fig. 5.2, with formation Poisson's ratio increasing from 0.25 to 0.45, which is the typical range of sandstone rocks, maximum safe injection rate decreases from 2570 ton/d to 1440 ton/d with the impact of thermo-elastic effect. It shows the change of P_{frac}^{T} due to v variation is much smaller compared to that in Fig. 5.1 respective to different *E*. Therefore, Poisson's ratio may be treated as minor factor for CO_2 injection sites screening.

(iii) Thermo-elasticity coefficient (α_T)

Thermo-elasticity coefficient describes how the size of an object changes with a change in temperature. In typical range of thermo-elasticity coefficient ($5\sim15\times10^{-6}$ K^{-1}),

the curves show the same influence on maximum injection rates (4100 ton/d, 2070 ton/d and 663 ton/d) as those of Young's modulus (in Fig. 5.3), which is due to the same role in the definition of thermo-elastic stress as that of Young's modulus (Eq. (3.1)).

(iv) Rock tensile strength (σ_s)

Rock tensile strength is an internal property of formation rocks. When we consider induced fracture initiation, firstly tensile failure occurs at borehole wall. Tensile strength exists only when rock is intact or no pre-existing faults/fractures in rock. The typical value of σ_s for sedimentary rocks is between 0 to 25 MPa, in which generally σ_s of limestone is higher than that of sandstone. Since natural formations usually contain pre-existing faults/fractures, to insure no fracture occurrence, in CO_2 injection project, we assume σ_s equals to zero for maximum injection rate estimation. In Fig. 5.4(a), it illustrates that intact formations with tensile strength (σ_s=2 MPa) could increases fracture initiation pressure (P_{frac}) for certain $\dot{m}$ by exact σ_s/2 (1 MPa) according to Eq. (5.1). The effect of σ_s is not diminished by the non-linear curve on P_{frac}^{T} in the case shown here. However, if P_w rises very quick with injection rate, the incremental maximum injection rate due to effect of σ_s would be very limited.

(v) Formation depth (D)

As we discussed in Chapter 4, bottom hole temperature of injected fluid depends on heat transfer between formation and borehole fluid, in which wellbore length, or formation depth, is an essential factor as shown in Fig 4.3.

As shown in Fig. 5.5, intersections stand for 3 pairs of nominal and real maximum injection rates for storage formations with different depth, such as 1000m, 2000m, and 3000m. We calculate the injection rate drop proportion for each formation. For example, in 1000m depth formation, the nominal maximum injection rate is 6300 ton/d and real injection rate is 2070 ton/d, where the drop is 4230 ton/d. We know the

proportion of injection rate drop is 67%. Similarly, in formation of 2000m and 3000m, the drop proportion is 37% and 28%, respectively. As the deeper the formation, the longer path for bore hole fluid heat transfer with surrounding formation and less temperature difference between them and thus lower impact of thermo-elastic effect. Therefore, the deeper the formation is, the smaller portion of injection rate drop. As can be seen, for CO_2 injection sites selection, deep formations are prior to shallow formations for acquiring high injection rate without fracturing formation.

(vi) Geothermal gradient (G)

Usually geothermal gradient does not have wide range and it averages from 25°C/km to 35°C/km. In Fig. 5.6, we can see maximum injection rate decreases from 2720 ton/d to 1500 ton/d when geothermal gradient increases from 25°C/km to 35°C/km. High geothermal gradient means quicker temperature raise in formations and larger temperature difference between borehole fluid and formation rock. Therefore, high G strengthens the effect of thermo-elastic stress due to high temperature difference.

(vii) Wellhead CO_2 temperature ($T(0)$)

From the definition of thermo-elastic stress ($\Delta\sigma^T$), we know ΔT is the only operationally controllable factor affecting $\Delta\sigma^T$ in a given formation. According to the analysis of wellbore heat transfer in Chapter 4 (as shown in Fig. 4.5), we remember high wellhead temperature of CO_2 significantly reduces bottom hole temperature difference (ΔT), especially at high injection rate (low β). In order to achieve high injection for large-scale CO_2 storage project, pre-heating CO_2 before injection is designed for controlling CO_2 wellhead temperature to overcome impact of thermo-elastic effect. After pre-heating, CO_2 still keeps supercritical state. Our assumption of constant density and specific heat capacity of CO_2 in wellbore is weakened as these properties vary with depth

from wellhead to bottom hole as shown in Fig. 4.2. However, average values of above two properties could partially reduce the influence of this assumption.

As shown in Fig. 5.7, we compare pre-heating for two storage formations with different Young's modulus, 10 GPa and 30 GPa. The former in Fig. 5.7(a) shows no big improvement on maximum injection rate (from 4060 ton/d to 5900 ton/d) when $T(0)$ rises 20^oC, as the impact of thermo-elastic effect is not strong; while in Fig. 5.7(b) it shows great increment on maximum injection rate from 663 ton/d to 5150 ton/d, which returns over 80% nominal injection rate (6300 ton/d). Definitely, if $T(0)$ keeps rising, extra injection rate could be achieved and even the real injection rate could be higher that nominal one. However, the energy cost should be accounted. The power cost of this example optimization, pre-heating 20^oC rise on $T(0)$, is 1910 KW, as 71KW for 100ton/d increment.

The high injection rate achieved by pre-heating CO_2 could save drilling expense for more wells to satisfy storage project requirements. On the other hand, pre-heating needs surface facilities and energy, which means extra capital and operating cost. Therefore, single well injection rate plays an important role in CO_2 injection and storage projects.

(viii) Formation permeability (k)

Permeability is a main factor on flow performance in reservoir and directly reflect P_w. Under criterion of P_{frac}, maximum injection rate is linear with permeability as intersections illustrated in Fig. 5.8(a), such as 625 ton/d, 6250 ton/d, and 62500 ton/d in 10 md, 100 md and 1000 md formation respectively.

The constraint of thermo-elastic effect on injection rate is even greater when the permeability of the storage formation is greater. In Fig. 5.8(b), with considering influence

of thermo-elastic effect, the intersections show real maximum injection rate is 305 ton/d, 2073 ton/d, and 16400 ton/d in 10 md, 100 md and 1000 md formation respectively. We can see high permeability does not bring the expected proportional increment benefit on maximum injection rate. On the contrary, injection rate drop proportion in higher permeability formation is larger, such as 41.4%, 66.3%, and 73.5% in the three above formations. Here we know the same results for formation thickness (h), which plays the same role as permeability (k) in bottom hole pressure calculation (Eq. (5.2)).

(ix) Single well drainage radius (r_e)

The size of storage formation (r_e) determines bottom hole pressure (P_w) at certain injection rate. However, neither P_{frac} nor P_{frac}^T is related to r_e. In Fig. 5.9, to compare the sensitivity of P_{frac}^T to r_e at formations with different Young's modulus, we consider formations with E equal to 10 GPa and 30 GPa. When the intersections locate at low injection rate (smaller than 2000 ton/d), such as the blue curve (formation Young's modulus 30GPa) with group of P_w, the influence of r_e is fairly low due to the linear behavior of P_w to injection rate. On the contrary, maximum injection rate is remarkably sensitive to r_e in formation with low Young's modulus (10GPa, red solid curve), where it varies from 5050 ton/d to 3400 ton/d corresponding to r_e from 1km to 100km. We can conclude maximum injection rate for a single injector at larger storage site is lower than that of smaller site in weak formations (low Young's modulus) because of the rise on P_w. Hence, maximum injection rate is higher in smaller drainage area of each injector.

(x) Formation fluid density (ρ_f)

Reservoir pressure (P_{res}) depends of formation fluid density. From flow performance model in Eq. (5.2) and Fig. 5.10 we know that P_w varies slightly at the same injection rate due to pore pressure change. Moreover, σ_h slightly varies according to Eq. (3.12). As seen, the dash lines almost overlap each other. Hence, the difference of

maximum injection rate for each case is mainly because of P_w. Injection rate drop is slightly smaller in hydrostatic pressure formation (drop 67%) than in overpressure formation (drop 72% and 77%). Therefore, the impact of maximum injection rate is slightly larger in overpressured storage formations.

5.3 SUMMARY

In this chapter, we apply fracture initiation criterion with considering the impact of thermo-elastic effect to estimate maximum injection rate for various scenarios. Based on the results of parametric analysis, we provide some conclusions on storage sites screening and operation optimizations for large-scale CO_2 sequestration projects.

Site screening is the first step for the whole CO_2 injection and storage projects. The purpose is to pick up appropriate sites to avoid potential dangers for high rate CO_2 injection projection, like fracture occurrence. Based on parametric analysis in last section, we may identify ideal formations for large-scale CO_2 injection and storage with following characters: (i) low Young's modulus; (ii) low Poisson's ratio; (iii) low thermo-elasticity coefficient; (iv) intact formation with high rock tensile strength; (v) deep formation; (vi) low geothermal gradient; (vii) formation with high permeability and large thickness; (viii) small drainage area for single well; (iv) hydrostatic pore pressure formation. Among these characters, Young's modulus and thermo-elasticity coefficient are major determinant factors on thermo-elastic effect and strongly influence maximum injection rate. The difference of maximum injection rate could be over 80% for typical formations with different Young's moduli. Especially, the large impact of thermo-elastic effect due to high Young's modulus of formation is not easily to be cancelled by the advantage provided by other parameters. For example, injection rate increment benefit due to formation permeability is drastically cancelled by the influence of thermo-elastic effect.

Single well drainage area is remarkably important on maximum injection rate especially at high rate stage.

To overcome natural defects of formations and increase injection rate, diminishing the influence of thermo-elastic effect is inevitable. From the above analysis, we know CO_2 bottom hole temperature itself is a function of CO_2 wellhead temperature and wellhead temperature may be the most feasible factor we can modify by operation. Pre-heating CO_2 before injection could largely decrease the influence of thermo-elastic effect and recover most injection rate back in some formations with high Young's modulus. On the other hand, the benefit of pre-heating is built on the capital of facility and energy consumption. Therefore, a balance between the cost and injection rate raise may need to be assessed as in the example we have done.

Table 5.1: Parameters that influence maximum injection rate $\dot{m}$ in Eq. (5.3)

Eq. (5.1)	$\sigma_h(D)$, E, v,α_T, $\Delta T(\alpha,\beta, \Delta T(0))$, σ_s
Eq. (5.2)	μ_{eff}, kh, r_e/r_w, p_{res}

Table 5.2: Base case value for sensitivity analysis

Young's modulus, E	20 GPa
Poisson's ratio, v	0.35
Thermoelasticity coefficient, α_T	1.0×10^{-5} K^{-1}
Rock tensile stress, σ_s	2 MPa
Wellhead CO_2 temperature, $T(0)$	15 °C
Earth surface temperature, $T_{fm}(0)$	20 °C
Geothermal gradient, G	30 °C/km
Wellbore radius, r_w	0.1 m
Formation thickness, h	50 m
Formation depth, D	1000 m
Formation permeability, k	100 md
Effective viscosity, μ_{eff}	4.0×10^{-4} Pa·s
Formation fluid density, ρ_f	1000 kg/m^3
Storage formation radius, r_e	10,000 m
Skin factor, s	0
Mean density of CO_2, ρ	800 kg/m^3
Mean heat capacity of CO_2, c_p	2500 J/kg·K

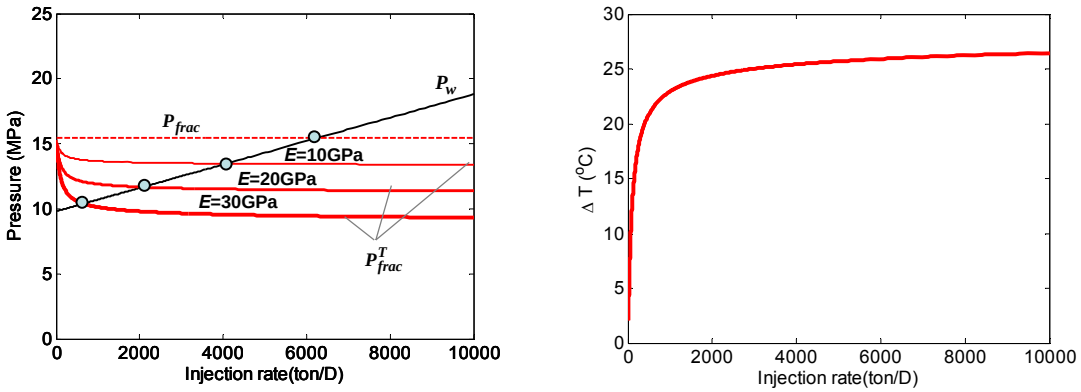

Figure 5.1: (a) The influence of thermo-elastic effect on maximum injection rate into formation rocks with different values of Young's modulus (E); other rock properties are given in Table 5.2. The black line indicate to bottom hole pressure of CO_2 injector; the red dash(s) line indicates to *nominal pressure for fracture initiation*, P_{frac}(ignoring thermo-elastic effects); the group of red solid lines stand for *real pressure for fracture initiation*, P_{frac}^T (thermo-elastic effect considered) at different formations. The intersection of black solid and red dash line indicates the nominal maximum bottom hole pressure and nominal maximum injection rate. The intersections of black line and red lines indicate the real maximum bottomhole pressure and real maximum injection rate. (b) Temperature difference versus injection rate.

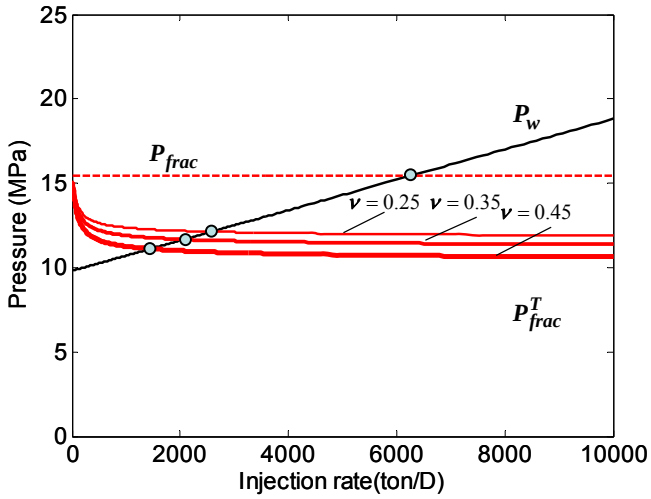

Figure 5.2: The influence of thermo-elastic effect on maximum injection rate at formation rocks with different Poisson's ratios (ν). The meaning of each curve and intersection are the same as in Fig. 5.1(a). Other rock properties are given in Table 5.2.

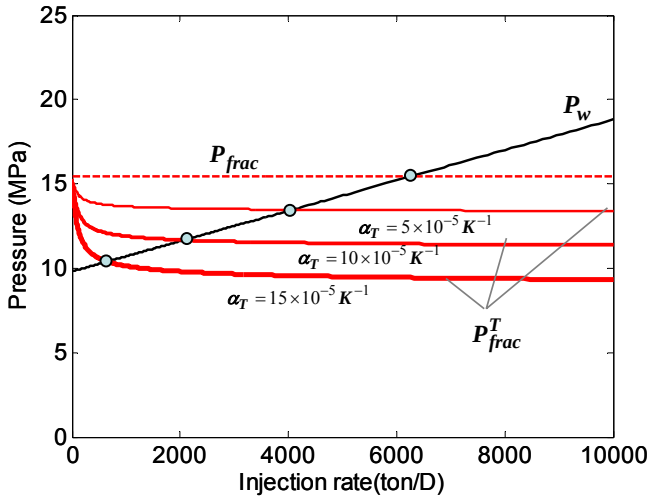

Figure 5.3: The influence of thermo-elastic effect on maximum injection rate at formation rocks with different thermo-elasticity coefficients (α_T). The meaning of each curve and intersection are the same as in Fig. 5.1(a). Other rock properties are given in Table 5.2.

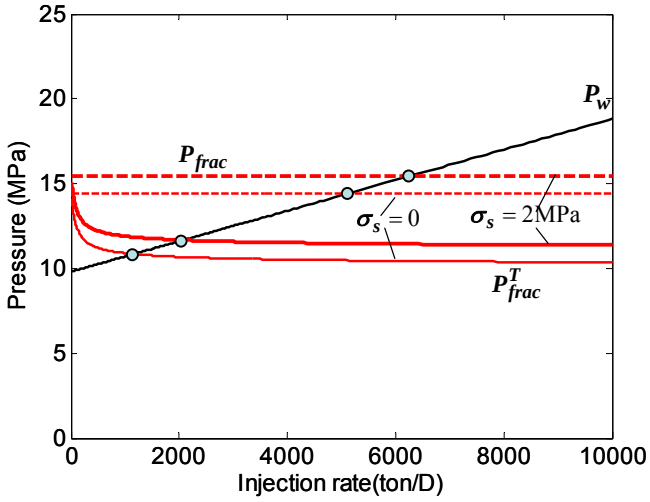

Figure 5.4: (a) The influence of thermo-elastic effect on maximum injection rate at formation rocks with different rock tensile strength (σ_s) The meaning of each curve and intersection are the same as in Fig. 5.1(a). Other rock properties are given in Table 5.2.

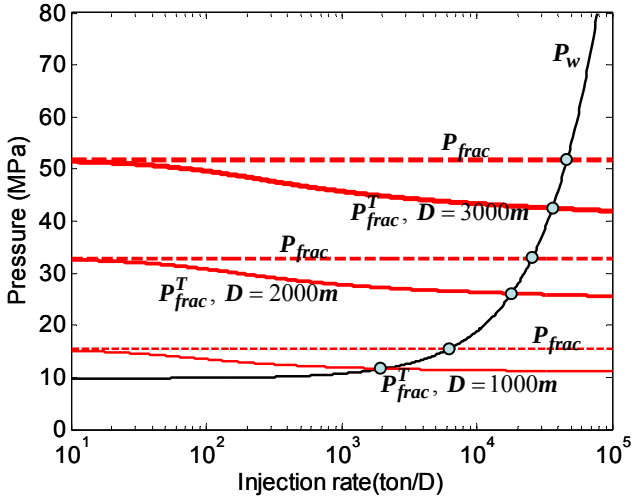

Figure 5.5: The influence of thermo-elastic effect on maximum injection rate at formations with different depth (D). The meaning of each curve and intersection are the same as in Fig. 5.1(a). Other rock properties are given in Table 5.2.

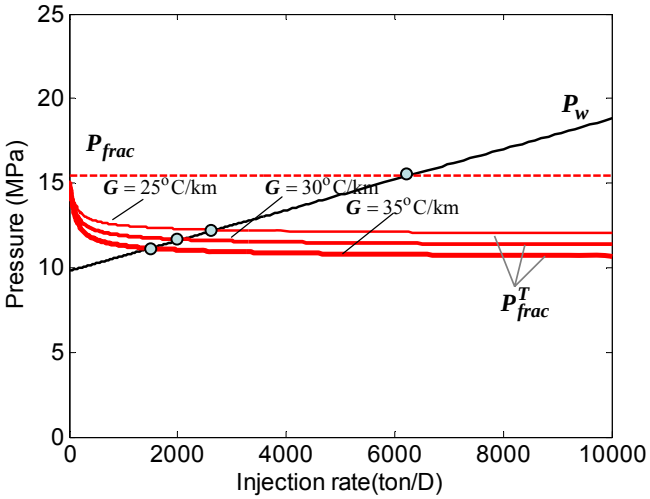

Figure 5.6: The influence of thermo-elastic effect on maximum injection rate at formations with different geothermal gradient (G). The meaning of each curve and intersection are the same as in Fig. 5.1(a). Other rock properties are given in Table 5.2.

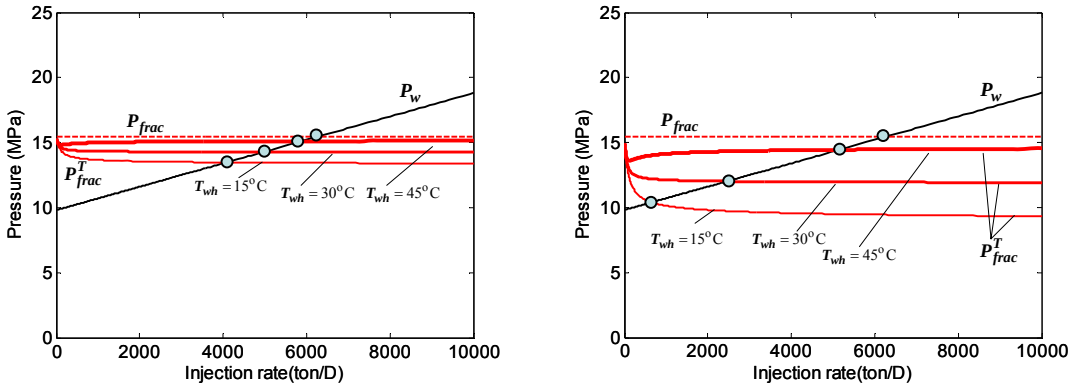

Figure 5.7: The benefit of pre-heating CO_2 before injection to reduce impacts of thermo-elastic effect on fracture initiation pressure and increase maximum injection rate for formations with different rock Young's modulus :(a) E=10 GPa; (b) E=30 GPa. The meaning of each curve and intersection are the same as in Fig. 5.1(a). Other rock properties are given in Table 5.2.

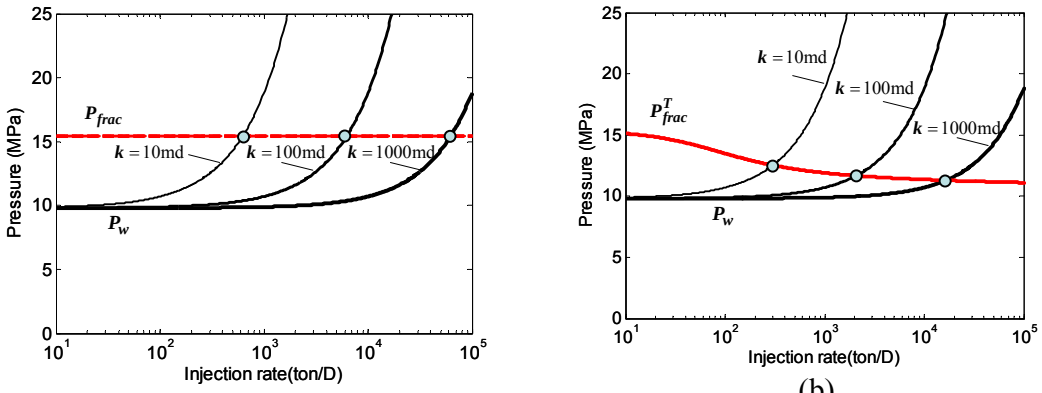

Figure 5.8: The influence of thermo-elastic effect on maximum injection rate at formations with different permeability (k). (a) injection rate under nominal fracture criterion without influence of thermo-elastic effect; (b) injection rate under fracture criterion with influence of thermo-elastic effect. The meaning of each curve and intersection are the same as in Fig. 5.1(a). Other rock properties are given in Table 5.2.

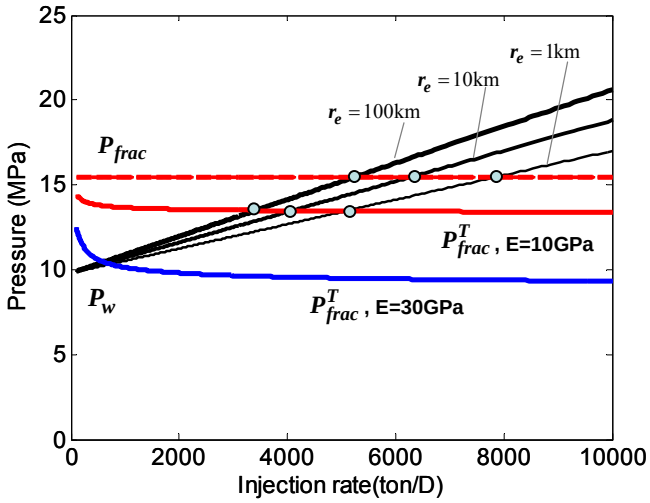

Figure 5.9: The influence of thermo-elastic effect on maximum injection rate at storage formations with different drainage radius (r_e). The groups of red solid curves and blue solid curves indicate to P^T_{frac} at formation with Young's modulus of 10GPa and 30GPa. The meaning of each curve and intersection are the same as in Fig. 5.1(a). Other rock properties are given in Table 5.2.

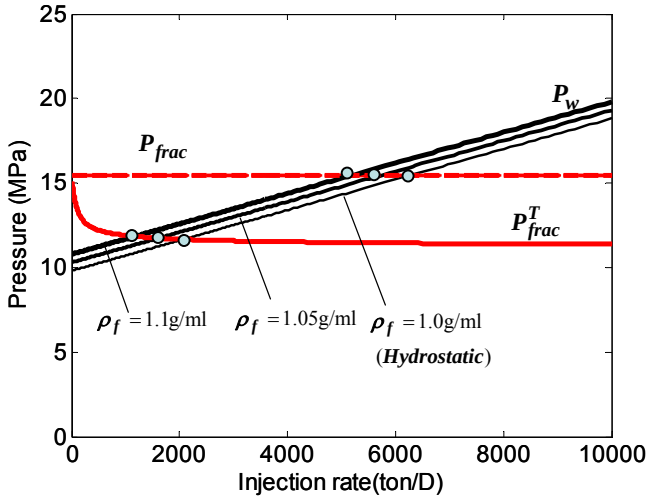

Figure 5.10: The influence of thermo-elastic effect on maximum injection rate at storage formations with different pore pressure (pore fluid density) (ρ_f). Curves for P_{frac} (red dash curves) and P_{frac}^T (red solid curves) at all scenarios almost overlap together. The meaning of each curve and intersection are the same as in Fig. 5.1(a). Other rock properties are given in Table 5.2.

Chapter 6: Influence of injection induced fractures initiation on horizontal injector

6.1 INTRODUCTION

Large-scale geological CO_2 storage requires high injection rate of single injector for economic considerations, which will save the cost of drilling. Compared to traditional vertical injection wells, horizontal injectors are more attractive to CO_2 storage projects due to large injectivities. However, when the bottom hole pressure is sufficient to overcome critical fracture pressure (Luo and Bryant, 2010), fractures would initiate and propagate. Such injection induced fracturing is a concern in risk assessment, as it may increase risk of leakage or unexpected plume migration. The large injectivity of horizontal injection wells makes them attractive for reducing the risk of induced fracturing by reducing bottom hole pressure, but thermo-elastic effects can drastically reduce the advantage of horizontal wells. Thermo-elastic stress induced by high injection rate can cause fracture initiation pressure to decrease and reduces maximum injection rate under no-fracture regulation.

In this chapter, by comparing injectivities of vertical injectors and horizontal injectors, we show the benefit of horizontal injectors for different injection scenarios. However, that benefit is challenged by thermo-elastic effect. Similar to Chapter 5, geological and operational parameters, such as reservoir permeability, horizontal wellbore length, storage drainage area, and vertical formation stress etc., are investigated for their influence on maximum injection rate. According to parametric analysis, applicability of horizontal injectors in CO_2 sequestration projects is concluded and

optimizations on horizontal injectors are designed to overcome the impact of thermo-elastic effect and thus recover the benefit of high injectivity of horizontal well.

6.2 INJECTIVITY BENEFIT OF HORIZONTAL INJECTION WELLS

Typically, the cost of a horizontal well is 1.4 to 3 times more than a vertical well, depending on drilling technology and field circumstance. Therefore, the expected injectivity of a horizontal injector should be at least 1.4 to 3 times more than a vertical injector. The injection well injectivity J is defined as,

$$J=q/\Delta P \tag{6.1}$$

where q is volume injection rate and ΔP is the difference between bottom hole pressure and reservoir pressure.

To simplify the description of CO_2 flow around horizontal injector, fluid flux from wellbore into formation is assumed uniform along the perforated zone and formation is assumed homogeneous and isotropic. The outflow performance is described by Borisov's model (1984),

$$P_w = P_{res} + \frac{\dot{m}\mu_{eff}}{2\pi\rho kh}[\ln(\frac{4r_{eH}}{L}) + (\frac{h}{L})\ln(\frac{h}{2\pi r_w})] \tag{6.2}$$

where L is perforated length of the horizontal wellbore, r_{eH} is horizontal well equivalent drainage radius, as

$$\pi r_{eH}^2 = \pi r_e^2 + 2Lr_e \tag{6.3}$$

The flow state is assumed as steady-state. The relation between bottom hole pressure and mass flow rate can be easily replaced by other models to predict the performance of steady-state flow in horizontal well with complex characteristics of the anisotropic and heterogeneous storage formation. Additionally, we assume the toe of horizontal well is closed. Hence, the pressure in the horizontal wellbore is constant.

By comparing with bottom hole pressure in Eq. (5.2), the ratio of horizontal well injectivity over vertical well injectivity J_h/J_v as shown below,

$$\frac{J_h}{J_v} = \frac{\ln(\frac{r_e}{r_w})}{\ln(\frac{4r_eH}{L})+(\frac{h}{L})\ln(\frac{h}{2\pi r_w})} \tag{6.4}$$

where r_e, L, and h are determinant factors. The values of parameters for injectivity analysis are set as in Table 6.1.

Fig. 6.1(a) illustrates injectivity of horizontal well declines with drainage area radius increasing. The injectivity benefit of single horizontal injector is not as high as might be expected for large storage site. In Fig. 6.1(b), we see the injectivity rising rate turns down after wellbore length over 700m. From economic perspective, wellbore length should be estimated both on drilling cost and expected injectivity. In Fig. 6.1(c), horizontal injector shows its great benefit for thin (small formation thickness) storage formation. Conversely, for storage formation with large thickness, injectivity of horizontal injector is not much higher than that of vertical injector. Therefore, vertical well is more economic for storage in thick formations.

6.3 IMPACT OF THERMO-ELASTIC EFFECT ON HORIZONTAL INJECTORS

Here we first describe the work flow to determine maximum injection rate with accounting for thermo-elastic effect. We cite the conservative criterion for fracture initiation to limit injection rate (bottom hole pressure) from Chapter 3. To keep the numbering of equations consistent, we recall Eq. (3.16), the conservative criterion for fracture initiation, and write it here as Eq. (6.5),

$$P_{frac}^{T} = \frac{3\sigma_h - \sigma_v + \Delta\sigma^T + \sigma_s}{2} \tag{6.5}$$

It is important to notice that in Eq. (6.5) $\Delta\sigma^T$ is a function of the distance (x) from heel of horizontal wellbore. Hence, P_{frac}^{T} varies along wellbore. Moreover, ΔT profile in

Fig. 4.14 shows that the highest temperature difference occurs at heel of horizontal injectors. The same trend occurs to the profile of $\Delta\sigma^T$, as shown in Fig. 6.2. On the other hand, nominal fracture initiation pressure (P_{frac}) and bottom hole pressure are constants from heel to toe of horizontal wellbore. As a result, the lowest value of $P_{frac}^T(x)$, most possible location for fracture initiation, is at the heel of horizontal injector (x_D=0), if wellbore is open hole or entirely perforated. In sum, once P_w is higher than P_{frac}^T at the heel of horizontal injector, fractures would initiate.

For simplicity, in the following discussion, for all open hole wellbore and entirely perforated horizontal wellbore, we use P_{frac}^T to stand for true fracture initiation pressure at heel of wellbore. On the contrary, for some special cases, like partial perforation, we will consider P_{frac}^T for the whole wellbore. All properties are listed in Table 5.2 and Table 6.1 unless specified.

If horizontal wellbore is an open hole or entirely perforated, true maximum injection rate can be solve from

$$P_w = P_{frac}^T \tag{6.6}$$

High injectivity of horizontal well brings the benefit of less energy consumed for pumping at the same injection rate. Although horizontal wells can provide high injectivity, injection rate is still limited by fracture initiation pressure (upper bound for bottom hole pressure) which may drastically decrease in some injection scenarios by the impact of thermo-elastic effect. Moreover, this impact is stronger for horizontal well injection compared to vertical well injection.

We first compare nominal maximum injection rates of horizontal injectors and vertical injectors. For the same injection rate, bottom hole pressure in horizontal well is lower than that of vertical well and this difference increase with injection rate, which are shown by the solid red and blue lines in Fig. 6.3(a). The two dash lines show nominal

fracture initiation pressure for vertical and horizontal injector respectively. The intersection of blue lines indicates to nominal maximum injection rate and corresponding bottom hole pressure of vertical injector (6300 ton/d and 15.4 MPa); while the intersection of red lines indicates to those of horizontal injector (9890 ton/d and 12.8 MPa). The injection rate increment is not as high as expected, since fracture initiation pressure of horizontal well is lower than that of vertical well due to different directions of bore hole plane and stresses in the plane.

From analysis in Chapter 5, we know that Young's modulus is a major factor determining thermo-elastic effect. Here, we compare two formations with Young's modulus 20GPa and 10GPa, as shown in Fig. 6.3(b) and Fig. 6.3(c). The impact of thermo-elastic effect is stronger in rock formation with higher Young's modulus (Fig. 6.3(b)), in which maximum injection rate drops from 6300 ton/d to 2070 ton/d for vertical injector (drop 67%); while for horizontal injector it drops from 9890 ton/d to 320 ton/d (drop 96.8%). In weak rock formation (Fig. 6.3(c)), maximum injection rate drops to 4070 ton/d for vertical injector (drop 35.4%) and 3570 ton/d for horizontal injector (drop 63.9%). In sum, no matter Young's modulus, the impact of thermo-elastic effect on injection rate drop for horizontal injector is much higher that that for vertical injector. In other words, in CO_2 sequestration projects with horizontal injectors, more attentions are inevitable on how to overcome the impact of thermo-elastic effect.

Similar to Chapter 5, we carry out parametric analysis about the impact of thermo-elastic effect on maximum injection rate. As conclusions obtained from geological parameters analysis (E, v, α_T, σ_s, D, G, ρ_f) in Chapter 5 are qualitatively applicable to horizontal injectors. Therefore, here we only focus on flow performance parameters unique for horizontal well injection, such as formation permeability (k), formation thickness (h), horizontal wellbore length (L), drainage radius of storage

formation (r_e), and formation bulk density (ρ_{fm}). These parametric analysis is on the scenario of injection into slight weak rock formation (E=10 GPa) which is more suitable for high rate injection projects.

(i) Formation permeability (k)

In Fig. 6.4(a), bottom hole pressure rises quickly with injection rate at formation with low permeability (10md) case. Maximum injection rate drops from 990 ton/d to 470 ton/d (drop 52.5%). In high permeability case (100md), Fig. 6.4(b), maximum injection rate drops from 9890 ton/d to 3570 ton/d (drop 63.9%). Accordingly, we can conclude the impact of thermo-elastic effect is stronger on injection rate in formation with larger permeability.

(ii) Formation thickness (h)

Storage formation thickness has a wide range of values among all CO_2 sequestration projects. In Chapter 5, we find h plays the same role as k in bottom hole pressure calculation of vertical injectors. However, for horizontal well, as in Eq. (6.2), P_w is no longer linear to h. In that case, even nominal maximum injection rate is not proportional to formation thickness. As shown in Fig. 6.5 (a) and (b), nominal maximum injection rate is 9890 ton/d and 18440 ton/d for 50m and 100m thickness formation, respectively.

Comparing true injection rates in two injection cases, we find impact of thermo-elastic effect is stronger in thicker formation. This is shown in Fig. 6.5 (a) and (b). In 50m thickness formation, maximum injection rate drop from 9890 ton/d to 3570 ton/d (drop 63.9%); while in 100m thickness formation, it drops from 18440 ton/d to 6330 ton/d (drop 65.7%). Furthermore, we know that injectivity of horizontal injector in thin storage formation is higher from Fig. 6.1(c). Given these points, we believe horizontal injectors are more appropriate for thin formations storage than for thick formation.

(iii) Horizontal wellbore length (L)

In Fig. 6.6(a) and (b), we compare two horizontal injector with different length, 1000m and 500m. The longer the wellbore, the lower the bottom hole pressure, and higher injectivity. Due to the impact of thermo-elastic effect, for the former case, maximum injection rate decreases from 9890 ton/d to 3570 ton/d (drop 63.9%); meanwhile for the latter case, maximum injection rate drops from 8100 ton/d to 3080 ton/d (drop 61.0%). The injection rate drop portion does not vary much for the two cases, since neither bottom hole pressure nor fracture initiation pressure varies a lot with wellbore length variation. In brief, the impact of thermo-elastic effect is not sensitive to horizontal wellbore length if it is open hole or entirely perforated.

(iv) Drainage radius of storage formation (r_e)

Drainage radius determines both bottom hole pressure and fracture initiation pressure. As shown in Fig. 6.7(a) and (b), nominal maximum injection rate for 10km and 100km storage formation is 9890 ton/d and 6250 ton/d. When we compare with vertical injector, in Fig. 6.7 (c) and (d), we find its nominal maximum injection rates are 6250 ton/d and 5220 ton/d, respectively. We may point out that the injection rate advantage of horizontal injector compared to vertical injector is gradually disappearing with drainage formation area increasing.

On the other hand, the impact of thermo-elastic effect on injection rate does not change much with drainage area. As it illustrated, for formation with 10km drainage radius, it is 3570 ton/d (Fig. 6.7(a)); which for formation with 100km drainage radius, it is 2300 ton/d (Fig. 6.7(b)). The drop portion of maximum injection rate for two cases both are about 63%. In contrast, injection for formations with 10km and 100km drainage radius by vertical injector (Fig. 6.7(c)), maximum injection rate is 4070 ton/d and 3400 ton/d and they both drops 34.8%. Given the comparisons of impact of thermo-elastic

effect and nominal maximum injection rate of both horizontal and vertical inject, we may conclude that horizontal well does not economically provide benefit on injection rate for CO_2 storage in formations with large drainage area.

(v) Formation bulk density (ρ_{fm})

Formation bulk density directly determines fracture initiation pressure through vertical stress in formations, which is a function of bulk density. From literatures, we know typical formation bulk density of some common rocks as listed in Table 6.2. In the two panels of Fig. 6.8, bottom hole pressure does not vary with formation bulk density change. However, nominal fracture initiation pressure drops 4.9MPa with formation bulk density increasing from 2.0g/cm^3 to 2.5g/cm^3. As a result, nominal maximum injection rate drops from 9890 ton/d to 1920 ton/d (drop 80.6%). Even without the impact of thermo-elastic effect, the huge reduction on maximum injection rate makes formations with high bulk density is improper for large-scale CO_2 sequestration projects.

Comparing true maximum injection rate with impact of thermo-elastic effect in two formations, we see in loose formation it drops from 9890 ton/d to 3570 ton/d (drop 63.8%); while in dense one is from 1930 ton/d to 45 ton/d (drop 97.7%). This result furthermore confirms that formation with high bulk density is not proper for large-scale CO_2 sequestration.

From the above qualitative analysis on geological parameters related to fracture initiation criterion or flow performance of horizontal well, we can summarize several advantages and disadvantages of horizontal injector for high rate injection projects as the following:

(i) Although injectivity of horizontal injector is higher than that of vertical injector, it does not mean true maximum injection rate of horizontal injector is higher. True maximum injection rate is determined by both bottom hole pressure and fracture

initiation pressure with impact of thermo-elastic effect, which both are lower for horizontal injector.

(ii) The impact of thermo-elastic effect on maximum injection rate is stronger in high permeability formations.

(iii) Horizontal well is more desirable for large-scale CO_2 storage in thin formations due to high injectivity and relatively small impact of thermo-elastic effect.

(iv) Considering drilling cost and maximum injection rate, we may conclude that short horizontal well is more suitable in CO_2 sequestration projects.

(v) Comparing maximum injection rate of single vertical or horizontal injector for CO_2 sequestration in large drainage area, it points out that horizontal injector is not a favorable option.

(vi) Since in-situ vertical stress relies on formation bulk density, from the definition of fracture initiation criterion for horizontal injector, maximum injection rate is determined by formation bulk density. Further, we find fracture initiation pressure in formations with high bulk density is extremely low compared to bottom hole pressure and it severely restricts injection rate. Hence, it should screen out high formation bulk density site for CO_2 storage projects.

6.4 OPTIMIZATIONS OF HORIZONTAL INJECTORS

Because of the huge impact of thermo-elastic effect, maximum injection rate of horizontal injectors drop drastically. To overcome the negative impact and recover injection rate, several operational approaches are discussed here. To emphasize the benefit of each approach, we select the case in Fig. 6.3(b), in which true maximum injection rate drops severely (from 9890 ton/d to 320 ton/d) due to strong impact of thermo-elastic effect in formation with higher Young's modulus (20 GPa).

(i) Partial perforation

We can diminish impact of thermo-elastic effect by perforating only between the toe and some location intermediate between toe and heel. In effect, this strategy uses the part of the horizontal wellbore between heel and the beginning of the perforations as a heat exchanger to warm up CO_2 before it flows into the formation. For example, by only perforating last half of horizontal wellbore, we can increase maximum injection rate about 3.6 times from 320 ton/d in the fully perforated wellbore to 1150 ton/d, as indicated in Fig. 6.9(a). By shortening perforated portion of horizontal wellbore, we may acquire high maximum injection rate, which is shown in Fig. 6.9(b). For 20% perforation, maximum injection rate can be as high as 2150 ton/d (5.7 times increment). This injection rate is still below requirements of large-scale commercial sequestration. Therefore this approach should be combined with other approaches discussed below to be feasible.

(ii) Pre-heating before injection

To overcome the impact of thermo-elastic effect on fracture initiation pressure, as well as maximum injection rate, pre-heating has been demonstrated to work well for vertical injector (cf. Chapter 5). Therefore, this approach is also discussed for horizontal injector.

As shown in Fig. 6.10, before pre-heating, maximum injection rate with no-fracture criterion restriction is only 320 ton/d. By pre-heating CO_2 at wellhead to 30^{o}C and 45^{o}C, maximum injection rate could be 2500 ton/d and 7800 ton/d.

As an illustration, by pre-heating CO_2 from 15^{o}C to 45^{o}C at wellhead, as shown in Fig. 6.11(a), temperature difference between formation and injected fluid at the heel (ΔT_{heel}) of horizontal wellbore is between 4^{o}C and 8^{o}C. For sufficiently large injection rate (1000 ton/d, 5.6^{o}C and 7800 ton/d, 4.1^{o}C), ΔT_{heel} is even smaller than that of lower injection rate (100 ton/d, 8^{o}C). Correspondingly, in Fig. 6.11(b), it demonstrates 7800

ton/d is a safe injection rate: the entire bottom hole pressure profile is below fracture initiation pressure.

The behavior of ΔT_{heel} in Fig. 6.11(a) is counterintuitive: larger injection rate can have a smaller temperature difference. The reason is illustrated in Fig. 6.12, which shows the temperature difference at heel of horizontal well varies non-monotonically with flow rate when the wellhead temperature is 45°C (green curve). The physical reason is as follows. First, the more the CO_2 is pre-heated, the deeper the intersection between the geothermal profile and the adiabatic profile, as shown in Fig. 6.13(a). This means the CO_2 is losing heat to the surroundings in most of the well. Large flow rates are advantageous in this situation because the CO_2 loses less heat and arrives at the bottom of the hole warmer, as shown in Fig. 6.13(a). The opposite is the case when the geothermal/adiabatic intersection is shallow: the CO_2 is gaining heat from the surroundings in most of the well, and small flow rates enable greater heat gain, so that the CO_2 arrives warmer at the bottom of the hole. This situation applies when $T(0)$=30°C (Fig. 6.13(b)) or 15°C, and consequently the corresponding trend of ΔT_{heel} with flow rate is monotonic in Fig. 6.12. On the other hand, the sequence of series of P_{frac}^{T} at heel of horizontal well (Fig 6.11(b)) is consistent with that of ΔT_{heel} (it stands for $\Delta\sigma^{T}$) (Fig 6.12(a)). Therefore, P_{frac}^{T} is not simply monotonic with injection rate.

Here it must be pointed out that bottom hole temperature of the case by pre-heating CO_2 before injection for high injection rate (7800 ton/d) in our model is an approximate prediction. Density and specific heat capacity of CO_2 vary with depth from wellhead to bottom hole as shown in Fig. 4.2, while our model approximates each value with a constant, average values.

The effect of pre-heating on maximum injection rate of horizontal injectors is non-linear with wellhead temperature of injected CO_2 (Fig. 6.14). The curve shows that

there is a threshold wellhead temperature and above that temperature maximum injection rate start to rise up quicker than that of vertical injectors. On the contrary, for vertical injectors, only linear relation was found between maximum injection rate and wellhead temperature. Thus, as calculated in Chapter 5, 71KW energy is consumed by pre-heating CO_2 to obtain extra injection rate per 100 ton/d for vertical injectors. However, energy consumption is also non-linear to incremental injection rate, as shown in Fig. 6.15.

6.5 SUMMARY

In this chapter, based on model of fracture initiation criterion with impact of thermo-elastic effect and horizontal well flow performance, we carry out parametric analysis to evaluate maximum safe injection rate for CO_2 storage projects under no-fracture regulation. By limiting maximum injection rate, we may avoid fracture occurrence in CO_2 sequestration projects. We have discussed pros and cons of horizontal injectors through parametric analysis and comparisons with vertical injectors. Although horizontal well is famous for high injectivity, it does not assure high injection rate, which depends on both bottom hole pressure and fracture initiation criterion. Impact of thermo-elastic effect is strong for horizontal injector and thus injection rate drop usually is unacceptable unless optimizations of the operating conditions are applied. Horizontal injector is undesirable for thick formations, formations with high permeability, formation with high bulk density, and uneconomic for storage formation with large drainage radius compared with vertical injectors. Additionally, length of horizontal wellbore does not obviously benefit maximum injection rate from economic perspective.

Several optimizations have been provided to overcome impact of thermo-elastic effect and increase maximum injection rate. Partial perforation can increase injection rate several times by making the first portion of the horizontal well function as a heat

exchanger for the CO_2. Maximum injection rate declines with length of perforated wellbore. Pre-heating is valid and effective for improving maximum injection rate for horizontal well injection. A threshold level of pre-heating for CO_2 is necessary to lessen temperature difference in the formation and thus lower impact of thermo-elastic effect. Fracture initiation pressure at heel of horizontal injector is non-monotonic versus injection rate in some pre-heating cases with high wellhead temperature. In other words, high injection rate is necessary to diminish impact of thermo-elastic effect once CO_2 is pre-heated above a certain temperature at wellhead. Incremental maximum injection rate of horizontal injectors is non-linear to wellhead temperature; while it is linear for vertical injectors. As a result, the higher the increment of injection rate is, the more energy consumed per unit increment.

Table 6.1 Parameters of horizontal injector for injectivity comparison with vertical injector

Wellbore radius, r_w	0.1m
Storage formation radius, r_e	10,000m
Formation thickness, h	50m
Horizontal wellbore length, L	1000m

Table 6.2 Typical bulk density of some common rocks

Sandstone	2.0-2.65 g/cm^3
Limestone	1.4-2.9 g/cm^3
Shale	2.3-2.8 g/cm^3

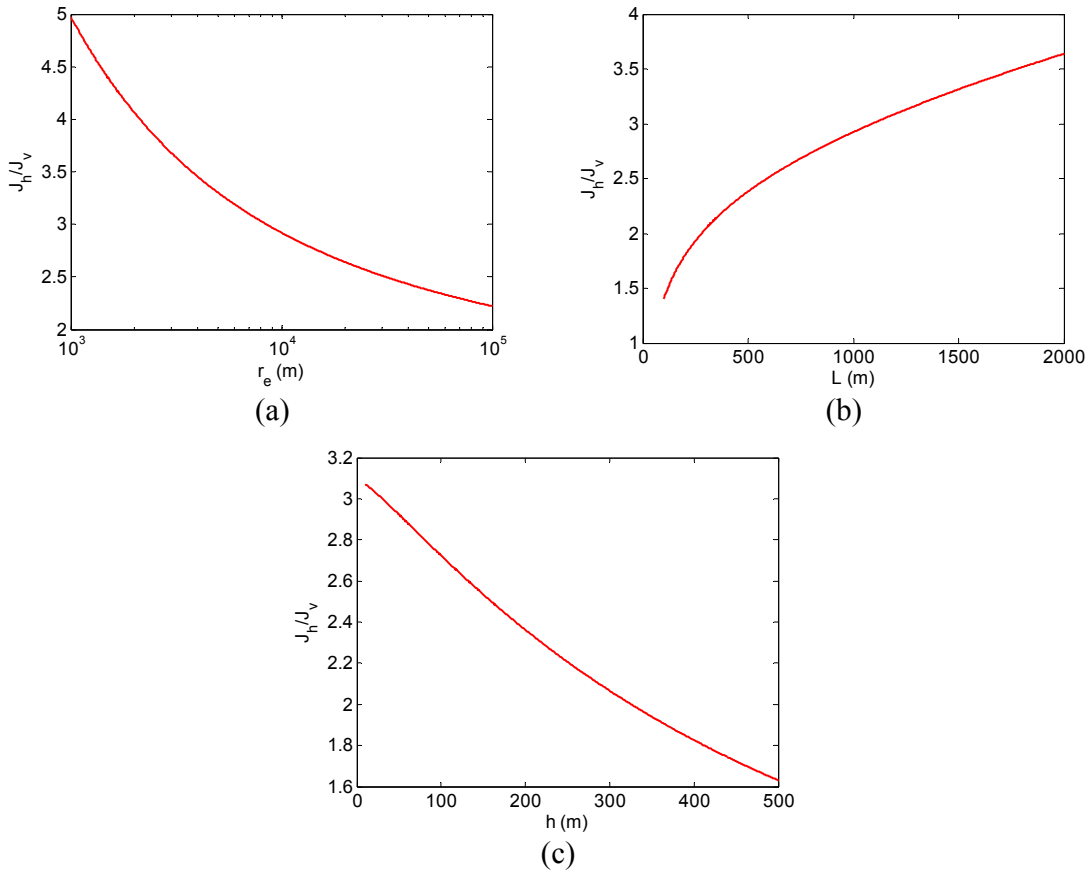

Figure 6.1: Injectivities of horizontal well and vertical well versus (a) drainage area radius; (b) horizontal wellbore length; (c) storage formation thickness. All parameters are given to Table 6.1.

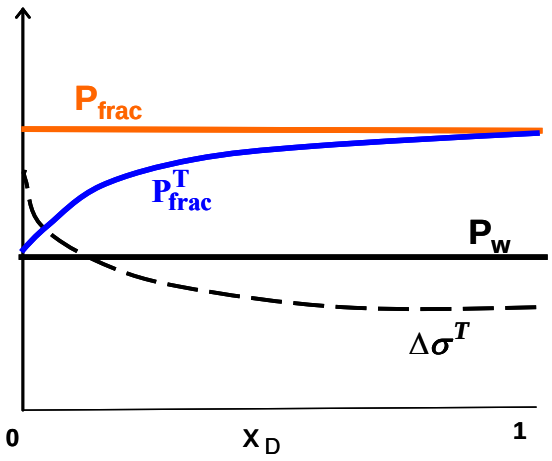

Figure 6.2: Profile of thermo-elastic stress (black dash line), bottom hole pressure (black line), nominal fracture initiation pressure (orange line), and true fracture initiation pressure that accounts for thermo-elastic stress (blue curve) vs. dimensionless distance along horizontal wellbore.

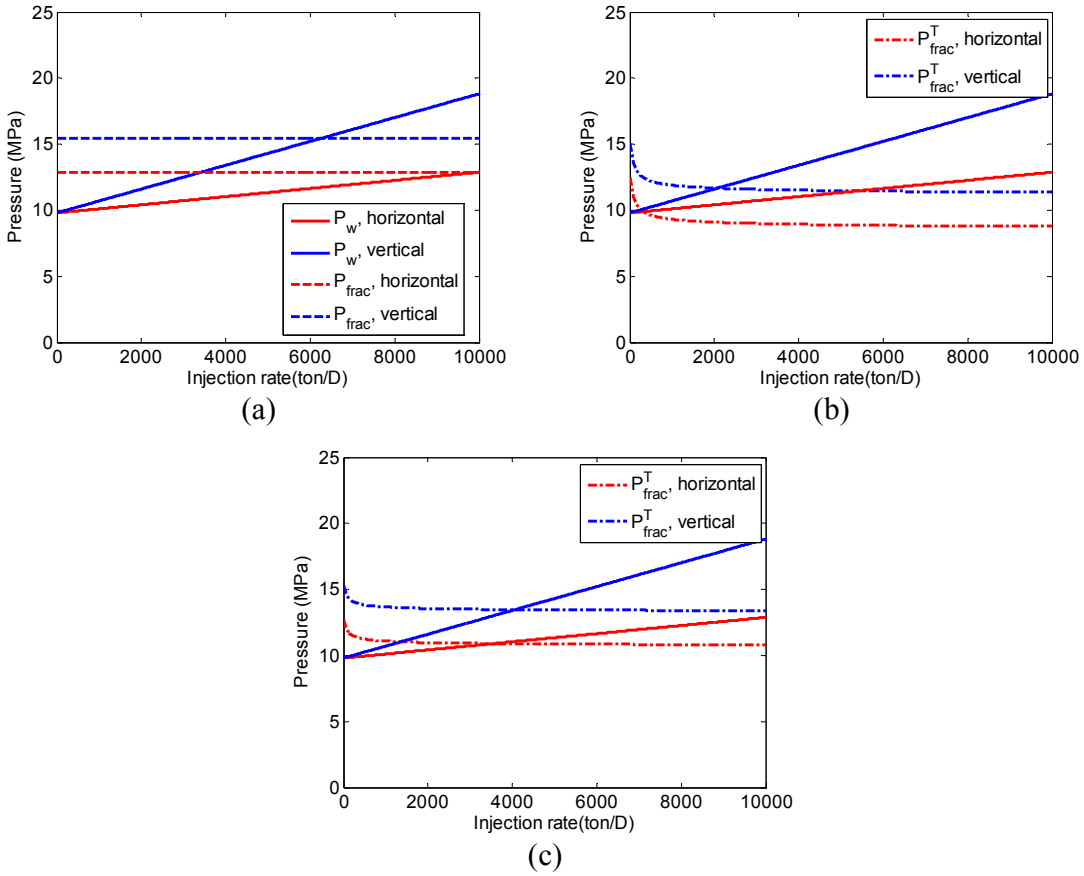

Figure 6.3: (a) Comparison on nominal injection rates of horizontal well and vertical well. Blue curves indicate to bottom hole pressure (solid line) and nominal fracture initiation pressure (dash line) of vertical well versus injection rate; while red curves indicate to bottom hole pressure (solid line) and nominal fracture initiation pressure (dash line) of horizontal well versus injection rate. (b) Comparison on true injection rates of horizontal well and vertical well by accounting thermo-elastic effect with formation Young's modulus E=20 GPa, where dot dash curves indicate to true fracture initiation pressure. (c) Comparison on true injection rates of horizontal well and vertical well by accounting thermo-elastic effect with formation Young's modulus E=10 GPa. Meanwhile, in each panel, intersections of the same color curves stand for maximum injection rate and corresponding bottom hole pressure.

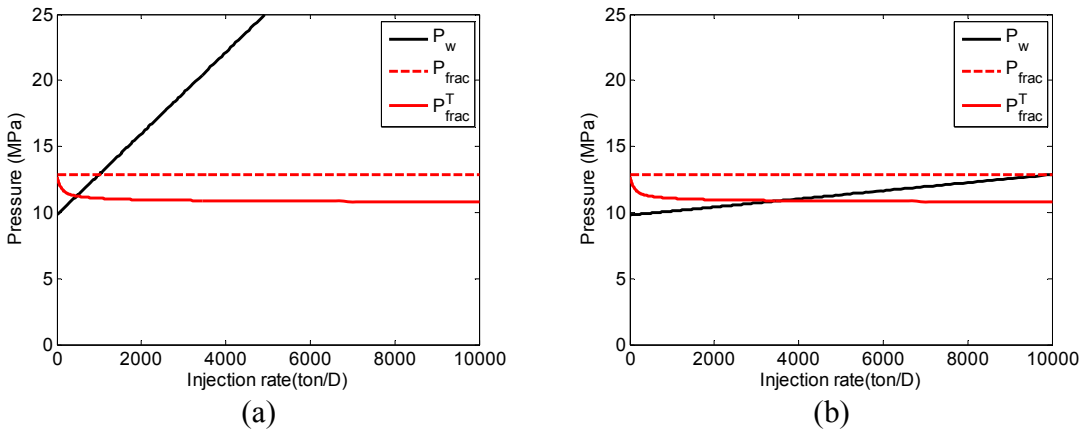

Figure 6.4: The influence of thermo-elastic effect on maximum injection rate of horizontal injectors with formation permeability (*k*) at (a) 10md; (b) 100md. In each panel, the intersection of red dash line with black line stands for nominal maximum injection rate and bottom hole pressure; while the intersection of red solid line with black line stands for true maximum injection rate and bottom hole pressure with the influence of thermo-elastic effect.

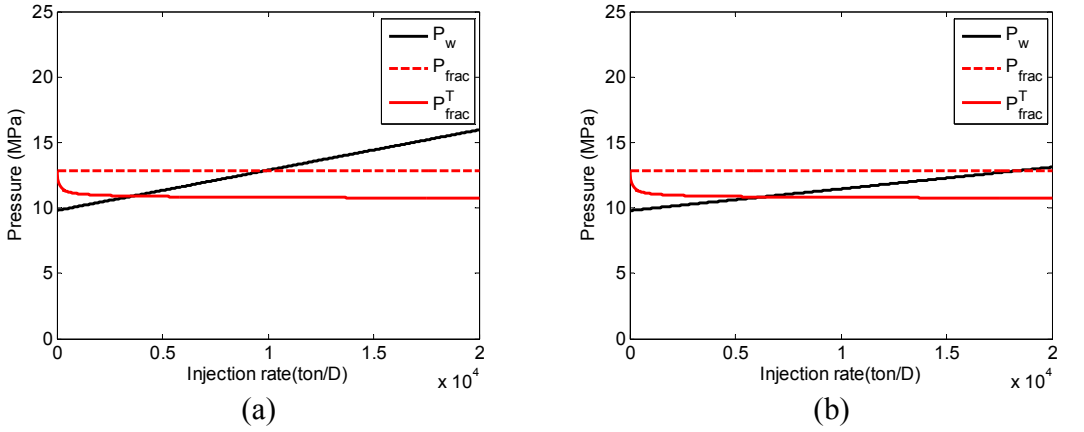

Figure 6.5: The influence of thermo-elastic effect on maximum injection rate of horizontal injectors with formation thickness (a) *h*=50m; (b) *h*=100m. The meaning of each curve and intersection could be referred in Fig. 6.2.

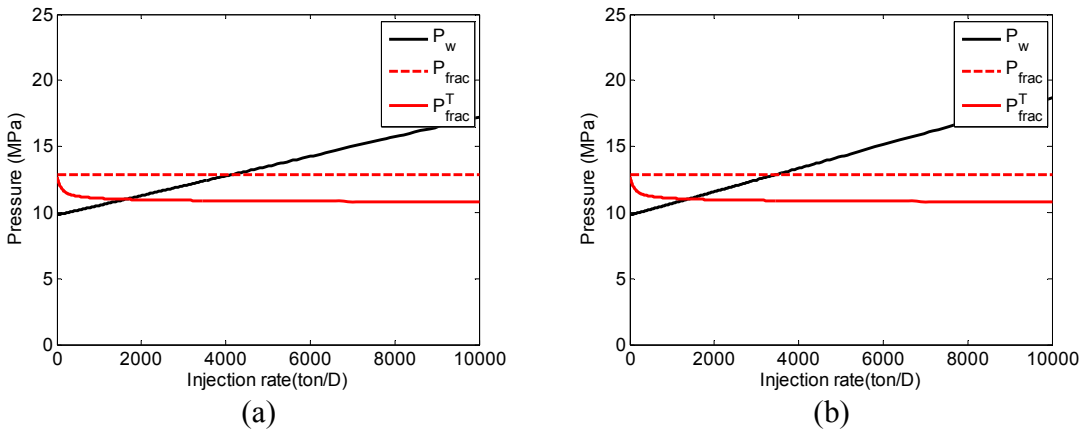

Figure 6.6: The influence of thermo-elastic effect on maximum injection rate of horizontal injectors with wellbore length (a) L=1000m; (b) L=500m. The meaning of each curve and intersection could be referred in Fig. 6.2.

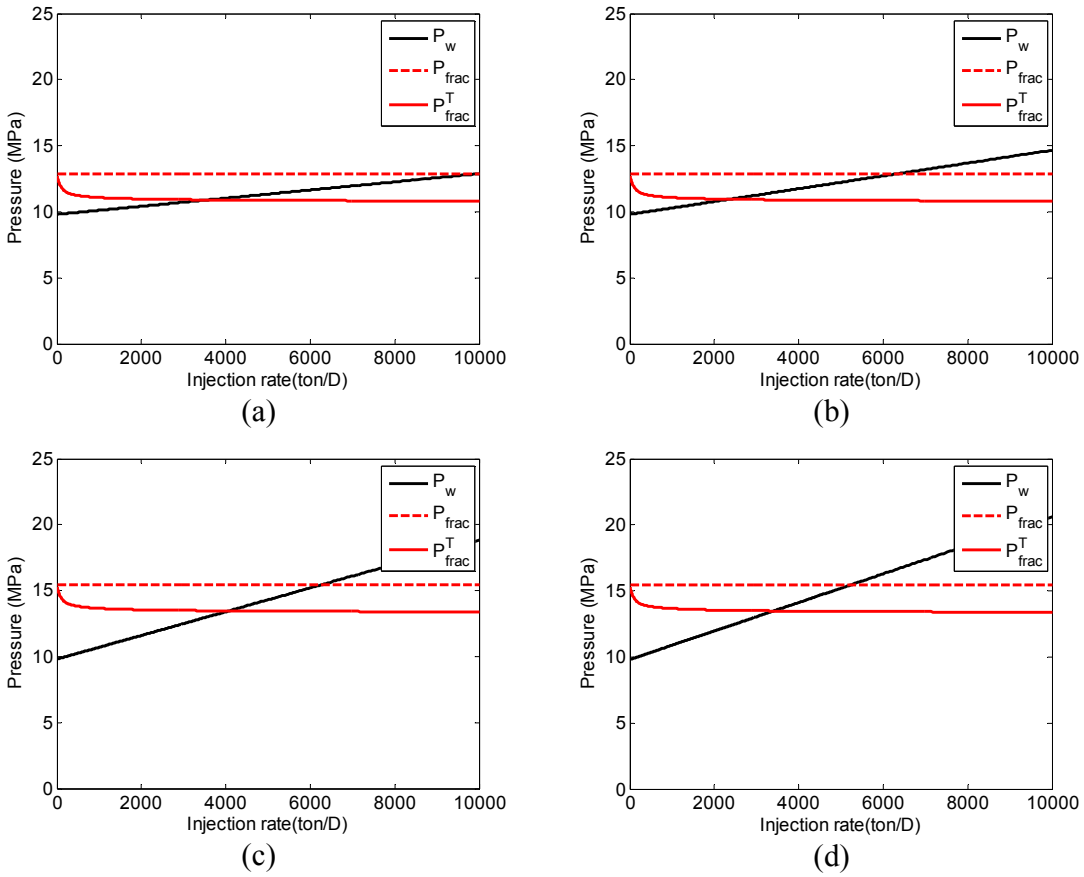

Figure 6.7: The influence of thermo-elastic effect on maximum injection rate of horizontal injectors with drainage radius of storage formation (a) r_e =10 km; (b) r_e=100 km; (c) injection into storage formation with (c) r_e =10 km and (d) r_e=100 km by vertical injector. The meaning of each curve and intersection could be referred in Fig. 6.2.

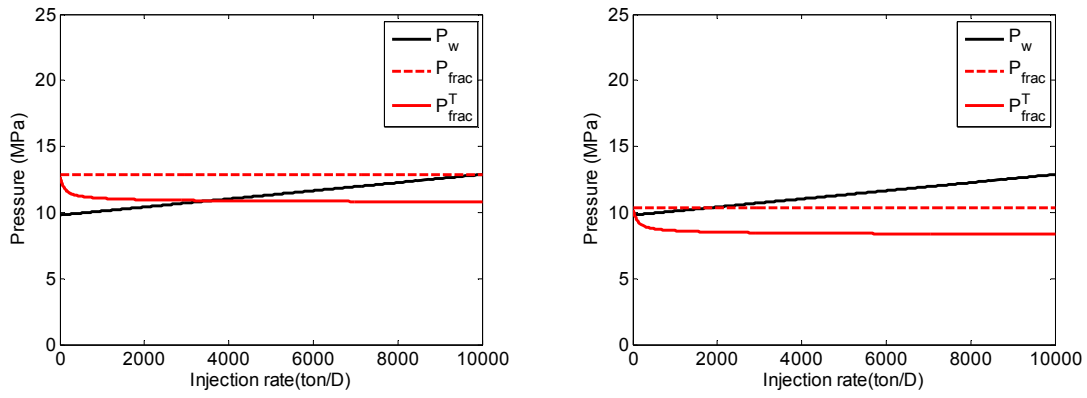

Figure 6.8: The influence of thermo-elastic effect on maximum injection rate of horizontal injectors with formation bulk density (a) ρ_{fm}=2.0 g/cm^3; (b) ρ_{fm}=2.5 g/cm^3. The meaning of each curve and intersection could be referred in Fig. 6.2.

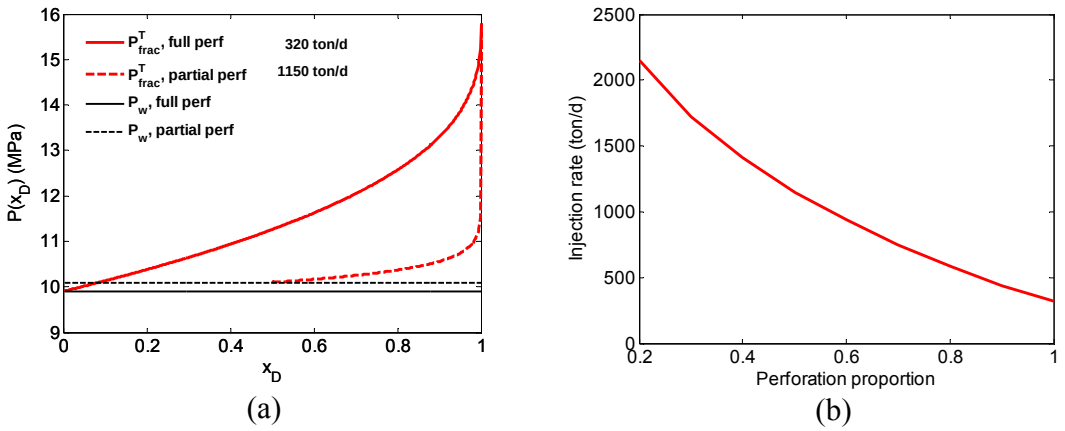

Figure 6.9: (a) Optimization to prevent fracture initiation by partial perforation, which is based on horizontal well injection case in Fig. 6.3 (b). The red solid curve and black solid line stand for P^T_{frac} and P_w of open hole or entirely perforated wellbore at maximum injection rate of 320 ton/d. By starting perforation from x_D = 0.5 (perforation on the latter half), the red dashed curve and black dash line show P^T_{frac} and P_w at 1150 ton/d. In effect the horizontal section $0 < x_D < 0.5$ is used as a heat exchanger and the remaining section to inject CO_2 into the formation; (b) Maximum safe injection versus perforated horizontal wellbore proportion.

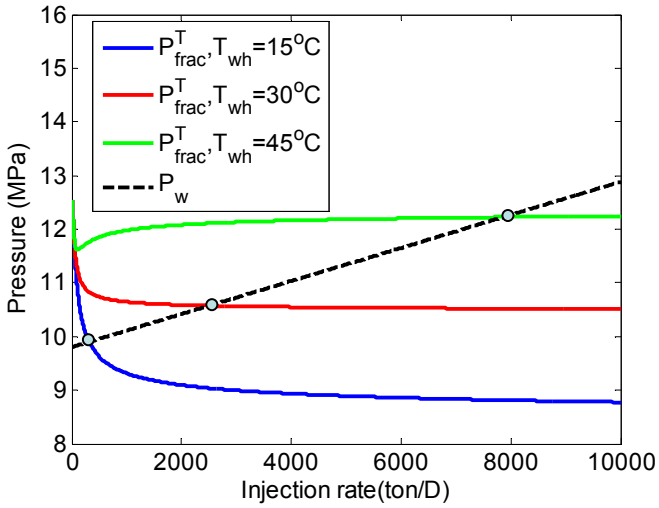

Figure 6.10: Optimization on maximum injection rate by increasing wellhead temperature of injected CO_2, which is based on horizontal well injection case in Fig. 6.3 (b). Intersections indicate to maximum injection rate and bottom hole pressure of each case.

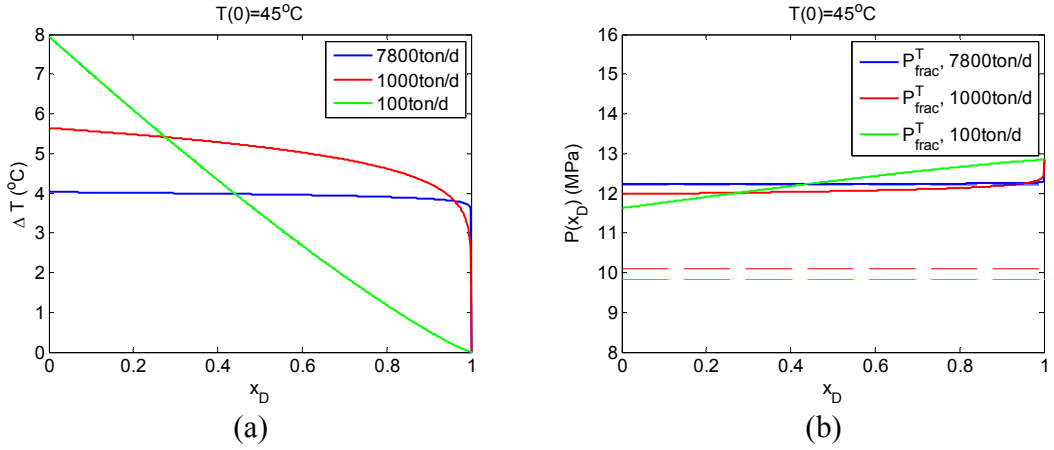

Figure 6.11: (a) Temperature difference profile along horizontal wellbore with various injection rates at $T(0) = 45^oC$; (b) Optimization to prevent fracturing by increasing $T(0)$ of injected CO_2. Solid color lines are fracture initiation pressure with accounting the impact of thermo-elastic effect. Dash lines are bottom hole pressures corresponding to each injection rate. According to fracture initiation criterion, once bottom hole pressure is higher than fracture initiation pressure at somewhere along horizontal wellbore, fractures would occur.

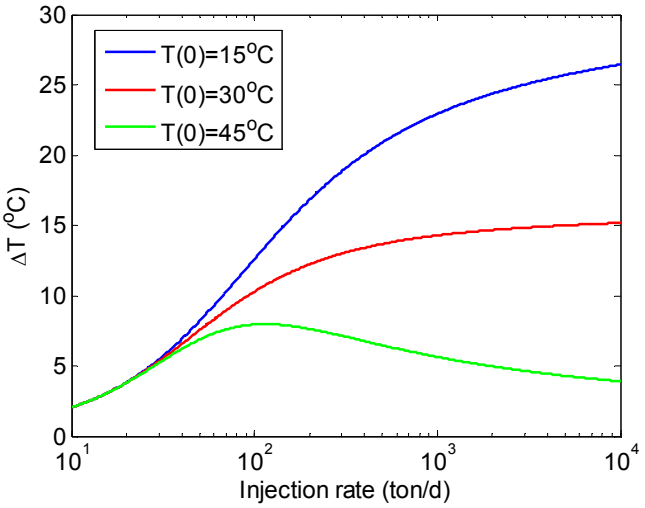

Figure 6.12: Temperature difference at heel of horizontal well at 1000 m depth versus maximum injection rate at different wellhead temperature. The non-monotonic behavior at $T(0)$=45 °C provides great benefit to reduce impact of thermo-elastic stress and recover the high injection rate capacity of horizontal injector.

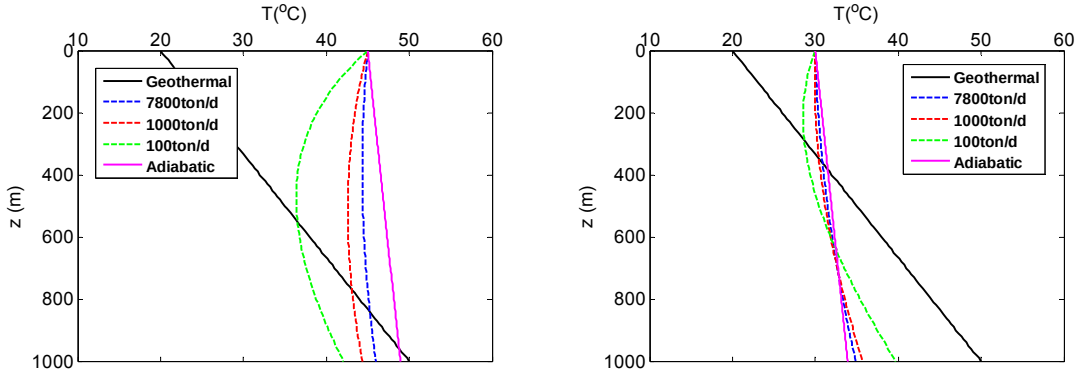

Figure 6.13: (a) Temperature profile in vertical section of wellbore of $T(0)$=45 °C. At large injection rate (7800 ton/d, blue dash line), bottom hole temperature is even higher than those at low injection rates (100 ton/d and 1000 ton/d, green and magenta dash line). At large injection rate the temperature profile approaches the adiabatic limit. This leads to the non-monotonic trend in Fig. 6.12 (green curve, $T(0)$= 45°C). (b) When $T(0)$=30°C, as injection rate increases the temperature difference at 1000 m increases, hence the monotonic profile in Fig. 6.12 (red curve, $T(0)$= 30°C).

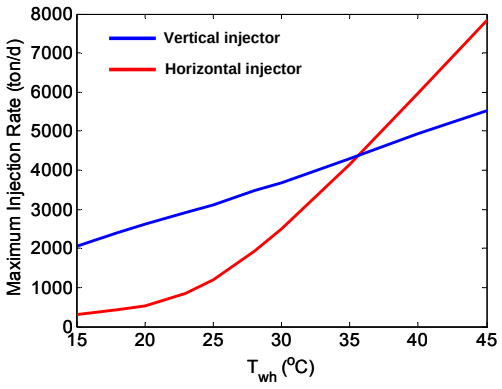

Figure 6.14: Comparisons of maximum injection rate versus wellhead temperature of injected CO_2 after pre-heating CO_2 at wellhead for vertical and horizontal injectors.

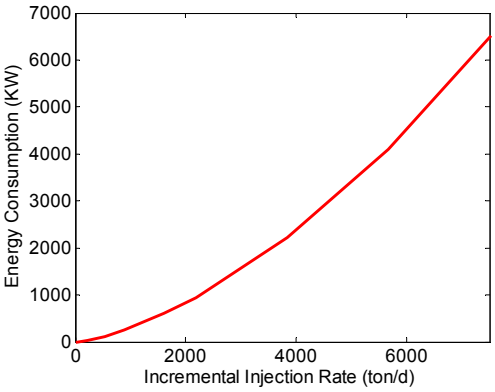

Figure 6.15: Energy consumption for pre-heating injected CO_2 versus incremental injection rate.

Chapter 7: Injection induced fracture propagation from vertical injector in CO_2 sequestration

7.1 INTRODUCTION

Depending on the tolerance of regulators for initiation of fractures in CO_2 storage formations, we have discussed qualifications of storage sites and injection strategies under rigorous regulation, i.e. a prohibition of induced fractures, for vertical and horizontal injectors in Chapter 5 and Chapter 6, respectively. On the other hand, if fractures are allowable, many more formations would be appropriate for CO_2 storage under this flexible regulation. Moreover, injection operation will be simplified if strategies and facilities for reducing temperature difference between injected CO_2 and formation at bottom hole need not be implemented. In sum, large-scale CO_2 injection with high rate would be easier in site screening and operation.

Since most formations are not perfectly intact and may contain pre-existing faults, veins, and fractures, fractures are highly possible to initiate and propagate from injection wells. Fracture growth greatly affects, injectivity of injectors, and CO_2 migration patterns. Fractures from injectors are high permeability conduits that can highly facilitate injection. According to whether fracture propagation is slow or fast, the influence on CO_2 fluid migration is totally different. Slow propagation can increase injectivity without changing flood region to flat ellipse shape (Fig. 7.1(a)); fast propagation increases injectivity but stretches flood region very flat in fracture growing direction and thus results in CO_2 arriving drainage area boundary in a shorter time (Fig. 7.1(b)). Therefore, predictions and monitoring are inevitable on injection induced fracture propagation and injected CO_2 migration.

As large amount of cool CO_2 are injected, formations are cooled and rocks deformation due to temperature change result in thermo-elastic stress, which leads to a reduction of local minimum horizontal stress in the cooled formation. The mechanism of fracture propagation of interest in this chapter is mainly based on the impact of thermally induced stress. Due to the reduction in minimum horizontal stress, the critical pressure for fracture growth at fracture tip can be much lower than expected pressure in hydraulic fracturing treatment. The magnitude of the reduction depends on the case of injection rate and formation conditions. If injection induced fracture occurs, the flooding system will evolve from a circular geometry in the map view to an ellipse, where the oblateness of flood area depends on fracture length and how fast the fracture grows.

In this chapter, we extend the model of Perkins and Gonzalez, originally developed for thermally induced fractures in water flooding of oil reservoirs, to account for propagation of fractures from CO_2 injection wells in brine-filled formations. The fracture propagation criterion is based on fracture mechanics by introducing the concept of rock fracture toughness and taking account of poro-elastic and thermo-elastic stresses. The effect of various boundaries on fracture growth and injectivity are discussed. The evolving elliptical shape of the flood front and thermal front are determined from fracture length and injection rate. By extending Buckley-Leverett theory in elliptic coordinate system, we introduce a two-phase fractional flow model for vertical fractured well. Combining this model with fracture propagation model, we can more accurately predict evolution of CO_2 and brine migration in storage formation. Finally, based on qualitative analysis, conclusions are given about fractures propagation and CO_2 flow migration.

7.2 MODEL OF SINGLE-PHASE FLOW INJECTION INDUCED FRACTURE PROPAGATION

Here we illustrate injection induced fracture from vertical injector as a two-wing like shape (Fig. 7.2). The fracture is assumed to initially grow as an enlarging penny-shaped crack until it becomes confined above and below and then its height is formation thickness (Perkins and Gonzalez, 1985). In CO_2 sequestration process, storage formation is cooled down and in-situ minimum horizontal stress decreases due to thermo-elastic effect. Stresses in upper and lower impermeable sealing layers do not obviously change. The increased difference between in-situ minimum horizontal stress in storage formation and that in sealing formation makes the injection induced fracture harder to invade overburden or underburden formation but stay in storage formation. Therefore, the cooling effect improves fracture height containment. In the map view of CO2 injection from fractured vertical well in Fig. 7.3, we see a region with cooled formation (inside blue ellipse) and cool CO_2 is sharply separated from regions at original reservoir temperature by the interface defined as thermal front (blue ellipse). Similarly, the interface between brine and CO_2 is defined as flood front (red ellipse). Between the two fronts, the fluid is injected CO_2 warmed by formation rock and residual brine. Fracture mechanics studies dictate that the face of fracture is perpendicular to the direction of minimum principal stress, which is minimum horizontal stress in normal faulting stress regime formations.

7.2.1 Mathematical description of the model

The procedure of our semi-analytical quasi-steady state model to estimate fracture growth and CO_2-brine migration is shown in Fig. 7.4. In this section, we introduce the base model with single phase piston-like fluid displacing process in an open boundary

system, assuming CO_2 not dissolvable in brine. There are several aspects of this model that can be considered separately.

(i) Fracture initiation criterion

We have concretely discussed fracture initiation criterion under rigorous regulation that no fracture occurs in intact formations for CO_2 storage site screening and injection operation guidance in Chapter 2 and Chapter 5. The fracture initiation pressure is cited below (Eq. (3.10)) by assuming formation is isotropic ($\sigma_H=\sigma_h$),

$$P_{frac}^{T} = \sigma_h + \frac{1}{2}\left(\Delta\sigma^{T} + \Delta\sigma^{P} + \sigma_s\right) \tag{7.1}$$

However, if fracture is allowed, we may relax restriction on appropriate formations as storage site. Here, we assume the storage formation has pre-existing flaws around injection well. Therefore, fracture has already initiated and it would grow once fracture propagation condition satisfied. We assume an initial fracture length (L_{f0}) equal to at least twice the wellbore radius as in previous literature (Hagoort et al., 1980). The fracture initiation pressure for formations with flaws is

$$P_{frac}^{T} = \sigma_h + \Delta\sigma^{T}(L_{f0}) + \Delta\sigma^{P}(L_{f0}) + \frac{K_{IC}}{\sqrt{\pi L_{f0}}} \tag{7.2}$$

$$K_{IC} = c_K \bullet \sigma_s \tag{7.3}$$

where K_{IC} is Mode-I rock fracture toughness (tensile open fracture). This parameter has been correlated with rock tensile strength that was used in previous chapters. The correlation coefficient c_K is cited from the work of Al-Shayea 2001 as 0.3057 for rocks in Saudi Arabia. Eq. (7.1) is different from Eq. (7.2), which describes the lowest bore hole pressure for breaking down the intact bore hole wall. In Eq. (7.2), fractures already initiated, the pressure (P_{frac}^{T}) is for fracture propagating at initial state.

(ii) Fracture propagation criterion

If pressure at fracture tip (P_{tip}) is higher than either Eq. (7.1) in intact formations or Eq. (7.2) in flawed formations, fractures would grow. Eq. (7.4) is the criterion for continued fracture propagation after initiation.

$$P_{tip} \geq P_{frac}^{prop} \tag{7.4}$$

The pressure for fracture propagation in Eq. (7.4) contains two parts as shown in Eq. (7.5): (I) Pressure required to keep fracture open towards local minimum horizontal stress; (II) Pressure required to overcome resistance at fracture tip and create new fracture volume. In part (I), original horizontal minimum stress is reduced by thermo-elastic stress ($\Delta\sigma^T$, quantity is negative due to cooling) and increased by poro-elastic stress ($\Delta\sigma^P$, quantity is positive due to pressure increase by injection).

$$P_{frac}^{prop} = \underbrace{\sigma_h + \Delta\sigma^T(L_f) + \Delta\sigma^P(L_f)}_{\text{(I)}} + \underbrace{\frac{K_{IC}}{\sqrt{\pi L_f}}}_{\text{(II)}} \tag{7.5}$$

where $\Delta\sigma^T$ and $\Delta\sigma^P$ is variable with geometry of thermal front.

$$\Delta\sigma^T = \frac{\alpha_T E \Delta T}{(1-\nu)} \bullet f(a_0, b_0, h) \tag{7.6}$$

$$\Delta\sigma^P = \alpha_p \Delta P \bullet f(a_0, b_0, h) \tag{7.7}$$

in which ΔT is formation temperature change at fracture tip due to CO_2 injection and ΔP is formation pressure change at fracture tip due to CO_2 injection and the function f accounts for geometric effects. In Eq. (7.7), is function of Poisson's ratio as discussed in Eq. (3.4). As noted, ΔT is negative and not a constant but calculated by heat transfer model vertical injector in Chapter 4. In finite thickness formations, geometry factor for $\Delta\sigma^T$ and $\Delta\sigma^P$ is (Perkins and Gonzalez, 1985)

$$f(a_0, b_0, h) = \frac{1}{1+(b_0/a_0)} + \left[\frac{(b_0/a_0)}{1+(b_0/a_0)}\right] \bullet \left(1 \Big/ \left\{1 + \left[1.45\left(\frac{h}{2b_0}\right)^{0.9} + 0.35\left(\frac{h}{2b_0}\right)^2\right] \bullet \left[1 + \left(1 - \frac{b_0}{a_0}\right)^{1.36}\right]\right\}\right) \tag{7.8}$$

where a_0 and b_0 is half length of major and minor axis of thermal front ellipse, respectively, as shown in Fig. 7.3.

(iii) Pressure at fracture tip

In this section, we assume the boundary is open and boundary pressure (P_{bc}) is constant during injection process. In latter sections, we will investigate the effect of boundary conditions on fluid migration and fracture growth. The pressure at fracture tip, in Eq. (7.5), is the sum of series of pressure drop from drainage boundary to fracture tip as shown in Fig. 7.5 (Perkins and Gonzalez, 1985).

$$P_w = P_{tip} = P_{bc} + \Delta P = P_R + \Delta P_1 + \Delta P_2 + \Delta P_3 \qquad (7.9)$$

where P_R is initial formation pressure. Because of open boundary assumption, P_{bc} keeps its initial value P_R. The bottom hole pressure is equal to the pressure at fracture tip if fracture has infinite conductivity.

The series of pressure drops are

$$\Delta P_1 = \frac{q\mu_{w,warm}}{2\pi k k_{rw} h} \ln\left(\frac{2r_e}{a_1 + b_1}\right) \qquad (7.10)$$

$$\Delta P_2 = \frac{q\mu_{g,warm}}{2\pi k k_{rg} h} \ln\left(\frac{a_1 + b_1}{a_0 + b_0}\right) \qquad (7.11)$$

$$\Delta P_3 = \frac{q\mu_{g,cool}}{2\pi k k_{rg} h} \ln\left(\frac{a_0 + b_0}{L_f}\right) \qquad (7.12)$$

where $\mu_{w,\,warm}$ is viscosity of brine out of flood front, $\mu_{g,\,warm}$ is viscosity of CO_2 between thermal front and flood front, $\mu_{w,\,cool}$ is viscosity of CO_2 inside thermal front. In Perkins and Gonzalez model, they assumed a residual oil saturation (0.25) in water flooded region. In our work, as CO_2 is weak wet to rock compared to brine, we assume there is no residual brine in CO_2 flooded area and S_g=1 as dry CO_2 (Burton et al., 2008). Experiments (Zuluaga, 2005) suggest that typical values of k_{rg}(S_g=1) are 0.7 to 0.85.

It is important to point out that we only consider pure CO_2 without suspended particle in injection process. Our model does not include pressure drop due to filter cakes

generated by suspended particles on fracture surface which is a substantial factor for fracture growth during water flooding in the of Perkins and Gonzalez. A direct comparison of our model with the water flooding model of Perkins and Gonzalez was not attempted.

(iv) CO_2-brine fluid migration

Injected CO_2 migrates from a fractured vertical well an elliptical shape. The pattern of the CO_2 evolution is confocal with fracture, as in Fig. 7.3. As in Eq. (7.6) and (7.7), to calculate $\Delta\sigma^T$ and $\Delta\sigma^P$, we need to know cooled region evolution during injection process.

To determine thermal induced stress at fracture tip, we need to know the front of cooled region. Although numerical simulation can give a comprehensive description of heat transfer in the formation, it is not economical and, more importantly, it is not easy to couple flow or heat transfer model into fracture propagation simulation. To simplify the problem, an approximation of cooled region is calculated by an energy balance theory. Following Perkins and Gonzalez (1985), we ignore the heat transferred from the overburden and underburden formations, and we determine the cool and warm regions from energy balance by

$$\rho_{co_2} C_{co_2} Q(t) = \left[\rho_{gr} C_{gr} (1-\phi) + \rho_{co_2} C_{co_2} \phi \cdot 1 \right] V_T \tag{7.13}$$

or

$$V_T = \frac{\rho_{co_2} C_{co_2} Q(t)}{\rho_{gr} C_{gr} (1-\phi) + \rho_{co_2} C_{co_2} \phi \cdot 1} \tag{7.14}$$

where C_{co2} is specific heat capacity of CO_2 in subsurface state, C_{gr} is specific heat capacity of formation rock grains, ρ_{co2} is the density of CO_2 in storage formation, ρ_{co2} is the density of formation rock grains.

Let L_f be half fracture length as shown in Fig. 7.3. The cooled region is an elliptical shape confocal with fracture and having volume V_T.

$$V_T = \pi a_0 b_0 h = \frac{\pi L_f^2 h}{4}(e^{2\xi_0} - e^{-2\xi_0}) \tag{7.15}$$

$$a_0 = L_f \cosh \xi_0 , \quad b_0 = L_f \sinh \xi_0 \tag{7.16}$$

Similarly, the volume of CO_2 flooded region is

$$V_{inj} = \frac{Q}{\phi(1 - S_{wr})} \tag{7.17}$$

where ϕ is formation porosity, S_{wr} is residual brine saturation in CO_2 flooded region, Q is total injected volume.

$$V_{inj} = \pi a_1 b_1 h = \frac{\pi L_f^2 h}{4}(e^{2\xi_1} - e^{-2\xi_1}) \tag{7.18}$$

$$a_1 = L_f \cosh \xi_1 , \quad b_1 = L_f \sinh \xi_1 \tag{7.19}$$

In this model, the system is assumed quasi-steady state for each time step and steady state flow performance model is applied. Half fracture length L_f starts from twice wellbore radius at time zero.

By running the model as the third box in flow chart as shown in Fig. 7.4, we can simply estimate fracture growth and its influence on CO_2 migration during injection. In the following, we will give some qualitative analysis based on the model to study impact of various geological factors.

7.2.2 Parametric analysis of dependence of fracture growth and flow performance on formation and fluid properties

CO_2 injection can result in three situations in storage formations:, no fracture occurs, fracture grows but stops after certain time, and fracture grows throughout the injection period. The specific case depends on injection rate and geological conditions of storage formations. Before discussing the results of parametric analysis in details, we

give a general sketch of factors related to injection induced fracturing as illustrated in Fig. 7.6. As in Fig. 7.6(a), high injection rate and low matrix permeability-thickness results in high bottom hole pressure and thus fracture growth. In (b), formations with overpressure condition (i.e. initial reservoir pressure exceeds normal hydrostatic pressure) require higher bottom hole pressure to maintain injection rate than that of hydrostatic formations, which implies fracture growth. Depth is directly related to fracture propagation pressure because it influences the magnitude of the minimum horizontal stress and of the thermal induced stress. The deeper the formation, the higher pressure needed for fracturing. In (c), two important factors of rock mechanics, Young's modulus and Poisson's ratio, are the key factors controlling thermo-elastic stress and poro-elastic stress. In strong formations with high Young's modulus and high Poisson's ratio, fractures are easier to occur than in weak formations due to the two injection induced stresses.

A study example of CO_2 injection induced fracturing

To illustrate the use of our semi-analytical model, Fig. 7.7 shows an example of CO_2 injection induced fracturing assuming a constant rate of CO_2 injection. The values of parameters for running the program are listed in Table 7.1 unless otherwise specified. In (a), red curves describe half major and minor axes of the elliptical shape region of injected CO_2; similarly the blue curves indicate axes for the thermal front. The green curve stands for the length of one wing of the fracture versus time. Fracture grows faster at early time and propagation speed declines with time. In this case, we see green almost overlaps with blue dash curve, which means fracture tip is at the same position as thermal front tip. Fracture tip cannot pass thermal front since it needs much higher pressure for fracturing in the region beyond the thermal front, because there is no reduction due to

thermo-elastic stress there. As shown in (b), bottom hole pressure (P_w) and fracture propagation pressure (P_{frac}^{prop}) decline with time and overlap with each other, as there is no pressure drop between the above two pressure due to fracture infinite conductivity. In this quasi-steady state model (Fig. 7.4), for each time step, in the inner iterations, we increase fracture length until P_w is lower than P_{frac}^{prop} . Hence, the curve of P_w is lower or overlaps with curve of P_{frac}^{prop} . From (c) we can see the reason that fracture propagation pressure declines as thermo-elastic stress is declining with time. Moreover, thermo-elastic stress is dominant compared to poro-elastic stress during injection process. In (d), we note that the ratio of major axis over minor axis of the flood front (a_1/b_1) increases with time, which means the ellipse of CO_2-brine boundary is growing flatter by fracture growth. Along with fracture growth, flooding pattern physically leaves plenty area unswept in the direction perpendicular to fracture. In other words, fractures shorten the breakthrough time of CO_2 flood front to storage formation boundary. In (e), at the same injection rate, bottom hole pressure of fractured injector is much lower than unfractured injector and this leads to the injectivity of fractured well in almost 1.7 times of unfractured well in (f). For the case of unfractured injector shown here, it is a virtual scenario presented only for illustration; in practice the bottom hole pressure would exceed fracture criterion pressure and the wellbore would fracture under these conditions. The injectivity increases with time due to the incremental conductivity provided by new growth fracture. In energy saving perspective, fracture provides of high injectivity benefit.

In the same formation, we investigate the impact of injection rate on fracture growth as shown in Fig. 7.8. We observe the length of fracture (green curve) and the distance of CO_2 flood front in major direction (red curve) from injector after 10,000 days injection. Above threshold injection rate (1530 m^3/d), fracture length is non-linear to injection rate in a narrow interval and then grows linearly with injection rate. The tip of

flood front increases linearly before threshold injection rate of fracture growth. After threshold injection rate, its relation turns from non-linear to linear with injection rate. It is important to notice, at high injection rate, fracture tip reaches flood front as the two curves overlap each other. This implies that the injection induced fracture reaches storage system boundary once flood front breakthrough drainage area, where CO_2 may easily leak out and contaminate surrounding environment.

Considering factors related to fracture growth regime behaviors in Fig. 7.6, permeability-thickness, injection rate, formation pore pressure, depth, Young's modulus, and Poisson's ratio of this case all belong to "fracture growth" regime. Therefore, fracture in this example does not stop unless injection ceased.

In the following, we carry out parametric analysis as we have done for fracture initiation in Chapter 5 and Chapter 6 to study the influence of various geological factors on fracture growth and thus on CO_2 migration.

(i) Young's Modulus (E)

Young's modulus is a major factor on thermo-elastic stress which is the reason that fracture propagation pressure declines as shown in Fig. 7.7(b). In fact, Young's modulus is the key factor controlling fracture growth. As shown in Fig. 7.9(a) of formation with low Young's modulus (10 GPa), fracture stops after 3910 days propagation to 86.2m.

In this special case, from the fourth panel of Fig. 7.9(a), we can see bottom hole pressure declines faster than fracture propagation pressure. In this analytical model, at fixed injection rate, only when Young's modulus is in medium value, fracture growth is "grow and stop" mode. The reason is currently not known and is left for future work.

Compared to drainage radius (10000m), approximately, we can ignore the influence of this short fracture on CO_2 migration, as flooded area is almost in circle shape

with a_1/b_1 equal to 1.009 (a_1 is about 716m) after 10000 days injection. However, the injectivity indeed acquires benefit from fracture, increasing to 1.43 times of unfractured injector. Therefore, short fractures during injection are generally favorable.

In Fig. 7.9(b), formation with medium Young's modulus (12GPa), fracture grows as fast as thermal front (753m after 10000 days injection), which stretches the region flooded (931m after 10000 days injection) by CO_2 into an elliptical geometry. Flood front in major axis moves faster than the case in (a). With Young's modulus increasing to 14GPa, as shown in Fig. 7.9(c), fracture grows almost as fast as flood front in major direction (L_f=1336m and a_1=1386m) and the flooding ellipse is much flatter than those of the preview two cases. In this case, as fracture tip almost reaches flood front, cool CO_2 flows from wellbore and along fracture and thereby directly reaches flood front. Thermal front thus overlaps with flood front in fracture growing direction. In contrast to ideal flood pattern as a circle shape, this flatter ellipse area stands for evolving fast in major direction while slow in minor direction. The geometry leads to a quick breakthrough and low usage efficiency of storage site. Moreover, fracture reaches the boundary of the storage formation and thus injected CO_2 may flow along fracture as a conduit to the outside of storage formation. Comparing all cases, we can conclude that the higher Young's modulus, the faster the fracture grows, the quicker flood front breakthrough, and the lower usage efficiency of storage site. The case of fracture stopping only exists in formations with low Young's modulus.

Another factor, thermo-elastic coefficient (α_T), impacts fracture growth and fluid migration on the same way as Young's modulus (E), as it plays the same role in the definition of thermo-elastic stress in Eq. (7.6).

(ii) Poisson's ratio (ν)

The impact of Poisson's ratio is on both thermo-elastic stress and poro-elastic stress as in Eq. (3.4). Reducing Poisson's ratio results in the slower growth of the fracture (in Fig. 7.10), as the increment of thermo-elastic stress is less than the increment of poro-elastic stress (Fig. 7.11). Due to the opposite signs of the two induced stresses, combining the two stresses increases pressure for fracture propagation. Especially, in early time, the increment of poro-elastic stress is much larger than thermo-elastic, as emphasized by grey circles in Fig. 7.11. In sum, effect of Poisson's ratio is stronger on poro-elastic stress than thermo-elastic stress.

(iii) Formation pore pressure (P_R)

As shown in Fig. 7.12(a), in formation with overpressure (1MPa), fracture grows with the speed over 2.5 times as that in normal hydrostatic formation. At the same injection rate, in formation with high pore pressure, higher bottom hole pressure is required, and high bottom hole pressure (Fig. 7.12(b)) is the reason of fast fracture growth. Moreover, high bottom hole pressure needs more energy for pumping.

(iv) Formation porosity (ϕ)

Fracture grows faster in high porosity formation as shown in Fig. 7.13. With porosity increasing from 0.15 to 0.25 (66.7% increment), increment of fracture length is from 623m to753m (20.9% increment) and flood front is from 1030m to 930m (10.8% decrement) after 10000 days injection. In other words, the impact of porosity on fracture growth and fluid migration is weak. Porosity is related to two physical properties during injection, such as volume for CO_2 storage and total heat capacity of rock grains.

With the same amount of CO_2 injected in case (a) and (b), formation with low porosity as in (a), it takes more volume to contain CO_2 and flood front evolves farther from injector although fracture is shorter. Additionally, we notice flood region in (a) is

more round (a_1/b_1 equals 1.26) than in (b) (a_1/b_1 equals 1.74), which means storage site usage efficiency in low porosity formation is higher.

The reason that fracture grows faster in high porosity formation is due to faster growth of thermal front. Growth speed of thermal front directly depends on total heat capacity of rock grains. Since there is less volume of rock grain in high porosity formation and specific heat capacity of rock grain is usually higher than that of CO_2 in formation state, total heat capacity of formation with high porosity is less. According to energy conservation, same amount of cool CO_2 transfers heat with more volume of rock grains and thus cause faster growth of thermal front.

(v) Volumetric rock heat capacity ($\rho_{gr}C_{gr}$)

Volumetric rock heat capacity is another factor directly determining thermal front growth speed. The typical range of $\rho_{gr}C_{gr}$ is between 1120 kJ/(m^3-K) and 2440 kJ/(m^3-K). Here we compare two injection scenarios, with $\rho_{gr}C_{gr}$ equal to 1270 kJ/(m^3-K) and 2340 kJ/(m^3-K) in Fig. 7.14. As we analyzed for high porosity case, low $\rho_{gr}C_{gr}$ results low total heat capacity of rock grains and thus it need more volume for heat transfer with injected cool CO_2. Given thermal fronts moves with almost the same speed in minor direction, it moves much faster in major direction in formations with low $\rho_{gr}C_{gr}$. As noted fracture propagates at the same speed with thermal front, fracture is longer in low $\rho_{gr}C_{gr}$ formation, which stretches flood front flatter. Under this analysis, it is not hard to conclude that fracture in formations with lower $\rho_{gr}C_{gr}$ is longer and it takes shorter time for flood front to breakthrough storage formation.

(vi) Formation permeability (k)

As shown in Fig. 7.15(a), to ensure fracturing in 100md formation, we increase injection rate to 3500 m^3/d. A high permeability formation (100md) enable injected CO_2

to leak off through short fracture (1081m) ; while low permeability formation (50md) requires long fracture (2461m) to provide enough conductivity. The model predicts that bottom hole pressure of 50md case is very high initially (Fig 7.14(b)). This would not be observed in the field; the large value reflects the limitation of steady-state flow model. In fact in early injection period, transient flow is dominant. This flaw would be corrected by setting infinite-acting boundary with transient flow for the model in the next section about effect of boundary condition on fracture growth. In sum, long injection induced fracture occurs in low permeability formation, which may result in a quick breakthrough due to extreme flat ellipse of flooded area.

(vii) Formation thickness (h)

Formation thickness plays exactly the same role as formation permeability on bottom hole pressure. Moreover, formation thickness also is a factor determining thermo-elastic stress and poro-elastic stress, which are considered in pressure for fracture propagation, as Eq. (7.5)-Eq. (7.7). As discussed by Perkins (1985), the larger the ratio h/b_0, the smaller the magnitude of thermo-elastic stress and poro-elastic stress. As a result, fracture propagation pressure is higher and bottom hole pressure is lower in thicker formations. Therefore, fracture is shorter in thicker formations, as shown in Fig. 7.16. For 50m thickness formation, fracture length is 2461m after 10000 day injection; while for 100m thickness formation, fracture length is 365m. As above mentioned, the effect formation thickness in geometry factor of thermo-elastic stress and poro-elastic stress at fracture tip makes fracture length shorter in (100m, 50md) formation than that in (50m, 100md) formation as shown in Fig. 7.15(a), although conductivities of the two formations are the same.

(viii) Storage formation size (r_e)

Size of storage site strongly affects bottom hole pressure of CO_2 injectors. In steady-state flow model, pressure drop is logarithmic to drainage area radius. Hence, bottom hole pressure monotonically increases with injection rate. As shown in Fig. 7.17(b), bottom hole pressure of smaller size storage formation (with drainage radius 5km) becomes lower and lower than that in 10km radius storage formation. In storage site with 5km radius fracture length is 474m after 10000 days injection while in 10km radius formation fracture length is 850m (Fig. 7.17(a)). Correspondingly, flood front in major direction (a_1) is 796.1m and 930.8m. Considering formations size, flood front will breakthrough smaller storage site earlier. On the other hand, comparing the shape of flooding area, it is more round in smaller site with a_1/b_1 equal to 1.24 for site with 5km radius and 1.71 for site with 10km radius (in Fig. 7.18). We can simply conclude that in small site storage usage efficiency is higher than in large site.

7.3 EFFECT OF STORAGE FORMATION BOUNDARY CONDITION ON FRACTURE PROPAGATION AND INJECTED FLUID MIGRATION

In the study of CO_2 injection induced fracture propagation and fluid migration in CO_2-brine system, it is important to identify and characterize the boundary conditions appropriately, as bottom hole pressure and injectivity are directly relevant. Most literatures on CO_2 sequestration employed open system with a constant pressure outer boundary for storage area (Noh, 2004; Kumar, 2005; Izpec, 2006; Burton, 2008), which is simple and convenient, but misleading. For the open system with constant pressure at boundary to be true in practice, the storage formation must outcrop to ground surface, lake or ocean, where it would be in equilibrium with the pressure of outer environment. The connection to outer environment would provide a potential path for injected CO_2 leakage or contaminating environment water, thereby going against the purpose of CO_2

sequestration. On the other hand, the assumption of open system is also widely used in published work about study of injection induced fracture for simplicity (Hagoort et al., 1980; Perkins and Gonzalez, 1985; Saripalli et al., 1999; Suri and Sharma, 2009; Suri et al., 2010). Previous work is rarely seen with analytical model to describe injection induced fracturing without open system assumption.

However, in nature, no-flow and infinite boundary is more likely to be found for CO_2 geological storage. The usual storage sites are like infinite-acting systems, where injected CO_2 displaces original brine outward from injection well to infinite distance. In other cases, if storage formations are sealed by faults or low permeability shale, no-flow boundary condition is more proper to model those closed system. Moreover, when CO_2 is injected into closed system, different from water flooding in reservoir engineering with producers, the pressure in the formation rises rapidly due to no "exit" for fluid and may cause fracture growth very fast. Therefore, open boundary description on storage formations is not able to capture features of some typical storage cases. In this section, we aim at introducing geological realism into the problem, storage formations with no-flow boundary and infinite-acting boundary are investigated. The model provides a quick and simple tool for estimating fracture growth and CO_2-brine migration with different boundary conditions.

7.3.1 Wellbore behavior in various boundary systems

(i) Open system (steady-state flow)

As shown in Fig. 7.19 (a), boundary pressure of an open system is constant. This is a very strong assumption as we discussed. However, steady-state flow model for open boundary systems is the simplest and is still most common used for analytically predicting injection induced fracturing. Therefore, it is not wrong but inaccurate to set

open boundary for estimating fluid migration and fracture growth in CO_2 storage projects.

(ii) Infinite-acting system (transient flow)

Infinite-acting system means the pressure at infinite distance is constant, which implies the pressure at system boundary is variable (see in Fig. 7.19 (c)). As infinite-acting boundary is very important for well testing of hydraulic fractured well, several literatures discussed transient pressure for fracture well (Gringarten, 1972, 1974; Cinco-Ley, 1981). The dimensionless form of well pressure for fractured vertical well in infinite-acting system is

$$P_D = \frac{1}{2}\sqrt{\pi t_{DL_f}}\left[erf\left(\frac{0.134}{\sqrt{t_{DL_f}}}\right) + erf\left(\frac{0.866}{\sqrt{t_{DL_f}}}\right) + 0.067Ei\left(\frac{0.018}{\sqrt{t_{DL_f}}}\right) + 0.433Ei\left(\frac{0.75}{\sqrt{t_{DL_f}}}\right)\right] \tag{7.20}$$

in which $t_{DL_f} = \dfrac{t}{\phi(c_t)_{eff}\left(\dfrac{\mu}{k}\right)_{eff} L_f^2}$.

As the definition of P_D is

$$\Delta P = P_w - P_R = \frac{q\left(\dfrac{\mu}{k}\right)_{eff}}{2\pi h} P_D \tag{7.21}$$

where $\left(\dfrac{\mu}{k}\right)_{eff} = \dfrac{\dfrac{\mu_{w,warm}}{kk_{rw}}\ln\left(\dfrac{2r_e}{a_1+b_1}\right) + \dfrac{\mu_{g,warm}}{kk_{rg}}\ln\left(\dfrac{a_1+b_1}{a_0+b_0}\right) + \dfrac{\mu_{g,cool}}{kk_{rg}}\ln\left(\dfrac{a_0+b_0}{L_f}\right)}{\ln\left(\dfrac{2r_e}{L_f}\right)}$, P_R is initial pressure for the entire formation, $\left(\dfrac{\mu}{k}\right)_{eff} = \dfrac{1}{kM_{eff}}$ is the reciprocal of total effective mobility times permeability. With quasi-steady state three fluid regions model, we can set

$$\frac{\ln\left(\dfrac{2r_e}{L_f}\right)}{M_{eff}} = \frac{\ln\left(\dfrac{a_0+b_0}{L_f}\right)}{M_{g,cool}} + \frac{\ln\left(\dfrac{a_1+b_1}{a_0+b_0}\right)}{M_{g,warm}} + \frac{\ln\left(\dfrac{2r_e}{a_1+b_1}\right)}{M_{w,warm}} \tag{7.22}$$

where $M_{g,cool} = \dfrac{k_{rg}|_{S_w=0}}{\mu_{g,cool}} = 10000\,(\text{Pa-s})^{-1}$, $M_{g,warm} = \dfrac{k_{rg}|_{S_w=0}}{\mu_{g,warm}} = 17400\,(\text{Pa-s})^{-1}$, $M_{w,warm} = \dfrac{k_{rw}|_{s_g=0}}{\mu_{w,warm}} = 2325\,(\text{Pa-s})^{-1}$. Fluid properties are seen in Table 7.1.

Since fracture is assumed with infinite conductivity, there is no pressure drop between wellbore and fracture tip and pressure at fracture tip can be

$$P_{tip} = P_R + \Delta P \tag{7.23}$$

in which P_R is initial pressure of entire storage formation.

(iii) Closed system

Closed system means there is no flow passing boundary, thus injected CO_2 is stored by expanding pore volume. As shown in Fig. 7.19 (b), average pressure of the formation increases linearly with time. All closed reservoir system have transient behavior if t_{DA}<0.0000025 and t_{DA} is defined

$$t_{DA} = \frac{t}{\phi (c_t)_{eff} \left(\frac{\mu}{k}\right)_{eff} r_e^2} \tag{7.24}$$

where $(c_t)_{eff} = \dfrac{c_{tg} \ln\left(\dfrac{a_1 + b_1}{L_f}\right) + c_{tw} \ln\left(\dfrac{2r_e}{a_1 + b_1}\right)}{\ln\left(\dfrac{2r_e}{L_f}\right)}$ is total compressibility of drainage area. In which $c_{tg} = c_f + (1 - S_{wr})c_g + S_{wr}c_w$, $c_{tw} = c_f + c_w S_{wi}$. c_f, c_w, c_g is compressibility of formation, brine, CO_2 in formation state, respectively. S_{wi} is initial brine saturation and S_{wr} is residual brine saturation of region flooded by CO_2.

However, the period of transient behavior is very short compared to CO_2 injection period. For example, transient time of the case based on Table 7.1 is approximate 30 days. Hence, here we ignore transient regime and directly count pseudo-steady state flow behaviors in CO_2-brine system.

The dimensionless format of well pressure for pseudo-steady state is

$$P_D = 2\pi t_{DA} + \frac{1}{2}\ln\left(\frac{r_e}{L_f}\right)^2 + \frac{1}{2}\ln\left(\frac{4}{\gamma C_A}\right) \tag{7.25}$$

where $\gamma = 1.782$ and $C_A = 31.62$.

For infinite conductivity fractures, fracture tip pressure equals to injector bottom hole pressure and is given by Eq. (7.21) and Eq. (7.23).

7.3.2 Comparisons of fracture growth and fluid migration in various boundary systems

Because of the inaccurate description of boundary condition by open system assumption, here we consider infinite-acting system (constant pressure at infinity) and closed system with no-flow boundary condition for studying injection induced fracture. Based on the models described above, we now focus on the flow performance of three systems.

Fig. 7.20 (a) shows the bottom hole pressure variation of three systems in storage formation with 10km radius. Burton (2008) has pointed out that the effective mobility of this CO_2-brine system increases with time, since the regions of cool and warm CO_2 with mobility much higher than that of brine expands during the whole injection process. Increasing mobility reduces the pressure needed for driving fluids outward wellbore. As shown in Fig. 7.21, the effective mobility of entire CO_2-brine system increases with time. As noted, in small system, mobility increases quicker (Fig. 7.21(b)) and bottom hole pressure declines quicker (Fig. 7.20(b)).

Given the boundary pressure in open system is constant, the increasing mobility means that bottom hole pressure decreases with time. On the other hand, the bottom hole pressures for the other two systems are complicated because of the variation of the boundary pressures. The boundary pressure of infinite-acting system slowly and slightly rises after pressure “touches” storage site boundary. Therefore, bottom hole pressure of infinite-acting system declines slower than that of open system. It is obvious that the initial bottom hole pressure of infinite-acting system is lower than that of open or closed

system, since it starts with transient flow with no interference (resistance) from boundary. After the resistance touched, the fracture initiates and bottom hole pressure suddenly falls by over 1MPa as shown at 545 days by blue curve in Fig 7.19(a).

In closed system, bottom hole pressure drops down initially until the whole reservoir pressure rises over the benefit of low displacing pressure due to increasing effective mobility of the system. After that bottom hole pressure starts to rise up drastically, as the average pressure of the whole reservoir increases rapidly which is inversely linear to bulk compressibility of formation (usually very small). The time of this balance breaking up depends on the size (pore volume) and compressibility of storage formation. Bottom hole pressure of closed system (dark green curve) rockets up after 4900 days injection in smaller size storage formation (drainage radius 5km) shown in Fig. 7.20(b); while the time for larger system (drainage radius 10km) is over 10000 days not shown in Fig. 7.20(a).

The size of storage formation also affects flow performance of open system and infinite-acting system. As discussed in parametric analysis in last section, we know bottom hole pressure is lower in smaller system with open boundary, and we also notice bottom hole pressure for infinite-acting system by comparing the initial values of two blue curves in (a) and (b). However, the influence of site size is stronger on open system than infinite-acting system, as shown in (b), bottom hole pressure open system declines faster.

As determined by bottom hole pressure, fracture growth in three systems (in Fig. 7.22) shows coincident trend corresponding to bottom hole pressure. Fracture grow fastest in closed system and growth speed starts to rise up corresponding to the time that bottom hole pressure rises up. Fracture growth in closed system is almost the same as in open system in a certain time and the time period depends on the size of system. As

shown in (a) and (b), the time is 3050 days and 1030 days. As bottom hole pressure in infinite-acting system varies slightly, fracture grows almost with constant speed. Fracture in infinite-acting system is shorter than that in open system until the bottom hole pressure of the former is over the latter, which could be seen in both small and large size systems.

In summary of the effect of system boundary conditions on fracture growth, we may conclude that open boundary assumption may overestimate fracture growth for in early time and underestimate it in late time, where the transition time depends on the size of storage system. Fracture grows faster than prediction with open boundary assumption in a closed system after a certain time in which the time depends on the size of storage system. Moreover, it is noted that even in closed system, CO_2 storage still can be operated in limited amount and fracture growth may not over that in systems with other types boundary.

7.4 MODEL OF TWO-PHASE FLOW INJECTION INDUCED FRACTURE PROPAGATION

In this section, we introduce Buckley-Leverett fractional flow theory to describe CO_2-brine system in the storage formation, which replace the piston-like single phase displacing model used in the preceding section. In the hope that it can more accurately evaluate pressure drop between fracture tip and drainage area boundary and predict evolution of CO_2 migration, we apply this new flow performance model in fracture growth estimation.

7.4.1 Extended Buckley-Leverett two-phase fractional flow model for fractured injector in elliptic coordinate system

Since brine can dissolve into supercritical state CO_2 and vice versa, the single phase model is not accurate to illustrate fluid migration in CO_2-brine system. Although

numerical simulations provide detailed information about mixture zone with two phases (CO_2-saturated water and water-saturated CO_2), it takes much cost and time. To simply describe boundaries (dry front and flood front) and saturations ($S_{g,dry}$ and $S_{g,BL}$) of two-phase zone, as shown in Fig. 7.23, Buckley-Leverett fractional flow theory is extended to apply for fractured vertical injector.

Traditional Buckley-Leverett theory is valid for 1-dimension immiscible displacement from vertical injector. Similar to the approaches in previous literature (Noh 2007, Burton 2008) which applied the fractional flow theory in radial flow from unfractured injectors, here we will build elliptic coordinate system and determine speed of fronts and phase saturation on each side of fronts by using the extended fractional flow theory as the following. Values of all properties used for extending fractional flow calculation are referred to Table 7.2.

We set V as the volume of ellipse confocal with fracture inside equisaturation contour S_g (CO_2 saturation) with half major axis $a = L_f \cosh\xi$ and half minor axis $b = L_f \sinh\xi$ at time t,

$$V = \pi abh = \pi L_f^2 h \cosh\xi \sinh\xi \tag{7.26}$$

The dimensionless form of volume is defined as,

$$V_D = V / V_e \tag{7.27}$$

where V_e is the drainage volume of the storage formation.

The dimensionless cumulative injected volume t_D is defined as,

$$t_D = \int_0^t \frac{q(t)dt}{A_e h\phi} = \frac{Q(t)}{A_e h\phi} \tag{7.28}$$

where A_e is drainage area of storage formation.

The dimensionless equisaturation S_g ellipse volume traveling at speed t_D is given by the following equation,

$$v_D = \frac{dV_D}{dt_D} = \frac{\pi L_f^2 \phi h \cosh 2\xi}{q} \frac{d\xi}{dt} \tag{7.29}$$

which can also be determined from fractional flow curve,

$$v_D = \frac{dV_D}{dt_D} = \left.\frac{df_g}{dS_g}\right|_{S_g} \tag{7.30}$$

where f_g is fractional flow of CO_2 phase.

According to the definitions in Noh's article (2007), we have dimensionless speed of the traveling volume of dry CO_2 front and flood front (also called Buckley-Leverett front) as,

$$v_{D,dry} = \frac{dV_{D,dry}}{dt_D} = \frac{\pi L_f^2 h\phi \cosh 2\xi_{dry}}{q} \left.\frac{d\xi}{dt}\right|_{\xi=\xi_{dry}} = \left.\frac{df_g}{dS_g}\right|_{S_{g,dry}} \tag{7.31}$$

$$v_{D,BL} = \frac{dV_{D,BL}}{dt_D} = \frac{\pi L_f^2 h\phi \cosh 2\xi_{BL}}{q} \left.\frac{d\xi}{dt}\right|_{\xi=\xi_{BL}} = \left.\frac{df_g}{dS_g}\right|_{S_{g,BL}} \tag{7.32}$$

By calculating the slopes of tangents to the fractional flow curve and applying CO_2 and brine mutual solubility theory, we know that

$$v_{D,dry} = \left.\frac{df_g}{dS_g}\right|_{S_{g,dry}} = \frac{f_{g,dry} - D_{BL\to dry}}{S_{g,dry} - D_{BL\to dry}} \tag{7.33}$$

$$v_{D,BL} = \left.\frac{df_g}{dS_g}\right|_{S_{g,BL}} = \frac{f_{g,BL} - D_{brine\to BL}}{S_{g,BL} - D_{brine\to BL}} \tag{7.34}$$

where $f_{g,dry}$ is fractional flow at dry front and $f_{g,BL}$ is fractional flow at flood front. $D_{brine\to BL}$ and $D_{BL\to dry}$ are determined by phase concentrations in different regions (Noh 2007).

Then we can identify positions of the three regions by calculating the positions of the two front ellipses. The values of ξ of the two ellipses are,

$$\xi_{dry} = \frac{1}{2}\ln\left[\frac{2v_{D,dry}qt}{\pi L_f^2 h\phi} + \frac{1}{2}\sqrt{\left(\frac{4v_{D,dry}qt}{\pi L_f^2 h\phi}\right)^2 + 4}\right] \tag{7.35}$$

$$\xi_1 = \frac{1}{2}\ln\left[\frac{2v_{D,BL}qt}{\pi L_f^2 h\phi} + \frac{1}{2}\sqrt{\left(\frac{4v_{D,BL}qt}{\pi L_f^2 h\phi}\right)^2 + 4}\right] \tag{7.36}$$

Then we know the half major and minor axes of the two ellipses are,

$$a_{dry} = L_f \cosh \xi_{dry}, \quad b_{dry} = L_f \sinh \xi_{dry} \tag{7.37}$$

$$a_1 = L_f \cosh \xi_{BL}, \quad b_1 = L_f \sinh \xi_{BL} \tag{7.38}$$

From the above formula, we can calculate the volume of dry and total flooded regions as

$$V_{dry} = \pi a_{dry} b_{dry} h \tag{7.39}$$

$$V_{inj} = \pi a_1 b_1 h \tag{7. 40}$$

The cooled volume depends on the position of thermal front. As shown in Fig. 7.24, thermal front may locate at two possible positions, either in dry CO_2 region or in two-phase region, depending on total heat capacity of formation rocks. We conceptually determine the cool and warm regions from energy balance as shown above in single flowing phase CO_2-displacing-brine model. The cool region can be calculated in two cases:

(a) $V_T < V_{dry}$, where V_T is the volume of cooled region

$$\rho_{co_2} C_{co_2} Q(t) = \left[\rho_{gr} C_{gr} (1-\phi) + \rho_{co_2} C_{co_2} \phi \cdot 1 \right] V_T \tag{7.41}$$

$$V_T = \frac{\rho_{co_2} C_{co_2} Q(t)}{\rho_{gr} C_{gr} (1-\phi) + \rho_{co_2} C_{co_2} \phi \cdot 1} \tag{7.42}$$

(b) $V_T > V_{dry}$

$$\begin{aligned} \rho_{co_2} C_{co_2} Q(t) = {} & \rho_{gr} C_{gr} (1-\phi) V_T + \rho_{co_2} C_{co_2} \phi V_{dry} \\ & + \rho_{co_2} C_{co_2} \phi S_{g,ave} \left(V_T - V_{dry} \right) \\ & + \rho_w C_w \phi \left(1 - S_{g,ave} \right) \left(V_T - V_{dry} \right) \end{aligned} \tag{7.43}$$

$$V_T = \frac{\rho_{co_2} C_{co_2} Q(t) + (\rho_w C_w - \rho_{co_2} C_{co_2}) \phi \left(1 - S_{g,ave} \right) V_{dry}}{\rho_{gr} C_{gr} (1-\phi) + \rho_{co_2} C_{co_2} \phi S_{g,ave} + \rho_w C_w \phi \left(1 - S_{g,ave} \right)} \tag{7.44}$$

where $S_{g,ave}$=($S_{g,dry}$+ $S_{g,BL}$)/2 is the average CO_2 saturation in two-phase region, C_w is specific heat capacity of brine, ρ_w is the density of brine in formation.

Similar to dry front and flood front, the thermal front is approximated as an elliptical region confocal with the previous two fronts and having volume,

$$V_T = \pi a_T b_T h = \frac{\pi L_f^2 h}{4}(e^{2\xi_T} - e^{-2\xi_T}) \tag{7.45}$$

By solving the above equation, we obtain

$$\xi_T = \frac{\ln y}{2} = \frac{1}{2}\ln\left[\frac{2V_T}{\pi L_f^2 h} + \frac{1}{2}\sqrt{\left(\frac{4V_T}{\pi L_f^2 h}\right)^2 + 4}\right] \tag{7.46}$$

$$a_0 = a_T = L_f \cosh\xi_T\,, \quad b_0 = b_T = L_f \sinh\xi_T$$

After identifying the positions of three fronts, we can estimate the pressure drop from fracture tip to drainage area boundary, ΔP, under the two fluid patterns shown in Fig. 7.24. We know the total pressure drop ΔP contains four parts, the only difference being one part is ΔP_{dry}^{warm} versus ΔP_{BL}^{cool}.

The total pressure drop is

(a) $V_T < V_{dry}$

$$\begin{aligned}\Delta P &= \Delta P_{dry}^{cool} + \Delta P_{dry}^{warm} + \Delta P_{BL}^{warm} + \Delta P_{brine}^{warm} \\ &= \frac{q}{2\pi khM_{dry}^{cool}}\ln\left(\frac{a_T + b_T}{L_f}\right) + \frac{q}{2\pi khM_{dry}^{warm}}\ln\left(\frac{a_{dry} + b_{dry}}{a_T + b_T}\right) \\ &+ \frac{q}{2\pi khM_{BL}^{warm}}\ln\left(\frac{a_{BL} + b_{BL}}{a_{dry} + b_{dry}}\right) + \frac{q}{2\pi khM_{brine}^{warm}}\ln\left(\frac{2r_e}{a_{BL} + b_{BL}}\right)\end{aligned} \tag{7.47}$$

where the relative mobility of each region is

$$M_{dry}^{cool} = \frac{k_{rg}\big|_{s_g=1}}{\mu_{g,cool}}, M_{dry}^{warm} = \frac{k_r\big|_{s_g=1}}{\mu_{g,warm}}, M_{BL}^{warm} = \left(\frac{k_{rg}}{\mu_{g,warm}} + \frac{k_{rw}}{\mu_{w,warm}}\right)\Bigg|_{S_g=S_{g,ave}}, M_{brine}^{warm} = \frac{k_{rw}\big|_{s_g=0}}{\mu_{w,warm}}$$

(b) $V_T > V_{dry}$

$$\begin{aligned}\Delta P &= \Delta P_{dry}^{cool} + \Delta P_{BL}^{cool} + \Delta P_{BL}^{warm} + \Delta P_{brine}^{warm} \\ &= \frac{q}{2\pi khM_{dry}^{cool}}\ln\left(\frac{a_{dry} + b_{dry}}{L_f}\right) + \frac{q}{2\pi khM_{BL}^{cool}}\ln\left(\frac{a_T + b_T}{a_{dry} + b_{dry}}\right) \\ &+ \frac{q}{2\pi khM_{BL}^{warm}}\ln\left(\frac{a_{BL} + b_{BL}}{a_T + b_T}\right) + \frac{q}{2\pi khM_{brine}^{warm}}\ln\left(\frac{2r_e}{a_{BL} + b_{BL}}\right)\end{aligned} \tag{7.48}$$

where the relative mobility of each region is $M_{dry}^{cool}=\frac{k_r g|_{s_g=1}}{\mu_{g,cool}}$, $M_{BL}^{cool}=\left(\frac{k_{rg}}{\mu_{g,cool}}+\frac{k_{rw}}{\mu_{w,cool}}\right)\Big|_{S_g=S_{g,ave}}$, $M_{BL}^{warm}=\left(\frac{k_{rg}}{\mu_{g,warm}}+\frac{k_{rw}}{\mu_{w,warm}}\right)\Big|_{S_g=S_{g,ave}}$, $M_{brine}^{warm}=\frac{k_{rw}|_{s_g=0}}{\mu_{w,warm}}$. From the above equations, we have

$$P_{tip}=P_R+\Delta P \tag{7.49}$$

By adding the information of two-phase region during CO_2-brine migration, bottom hole pressure could be more accurately estimated and thus fracture growth. The rest of the procedure for fracture growth calculation is the same as that in single phase flow model (Section 7.2) and thus we do not repeat it here.

7.4.2 Fracture growth based on two-phase flow performance model

Compared two panels in Fig. 7.25, we find fracture grows faster with two-phase flow model (803m) and CO_2 flooded region is more round with two-phase flow model (a_1/b_1 equals 1.36) than those of single-phase model with fracture length 753m and a_1/b_1 equals 1.71 after 10000 days injection. In two-phase flow model, flood front moves faster to 1182m in major direction after 10000 days injection compared to 931m by single-phase flow model. It may explained the why fracture growth faster in two-phase flow model by its higher bottom hole pressures in Fig. 7.26(a). Hence, injectivity is overestimated by single-phase model as shown in Fig. 7.26(b).

As we mentioned in the last part of model, volume of cooled region (V_T) may or may not be larger than pure CO_2 region (V_{dry}). By investigating porosity and volumetric rock heat capacity, we demonstrate both cases are possible to exist during CO_2 injection process. As the two cases in Fig. 7.27, in low porosity and high volumetric rock heat capacity formation, V_T is smaller than V_{dry}, and vice versa.

In conclusion, the two-phase model can more practically mimic the system of CO_2-brine by considering the mutual dissolution two-phase region in the formation. By introducing two-phase region, flow performance can be estimated more accurately from the bottom hole pressure and injectivity. These features enable to predict flooded region shape, CO_2 migration speed, and fracture length more accurately compared to traditional analytical injection induced fracturing model with single-phase flow.

7.5 SUMMARY

The implication of this chapter is profound. A simple and results immediately shown semi-model is provided to predict CO_2 injection induced fracture growth and CO_2 migration in storage formations. Much more important, the model improves storage site boundary condition of traditional CO_2 sequestration model from open system to infinite-acting system or closed system, which are more realistic situations of storage site. By extending Buckley-Leverett fractional flow theory in elliptical coordinate system, we successfully incorporated two-phase flow model to semi-analytical model of injection induced fracture. The improvement enable CO_2-brine mutually soluble mixture region in CO_2-brine migration system, which allows more accurately predict flow performance from fractured vertical injectors.

We also investigate fracture growth in various injection scenarios by parametric analysis on operation factors and geological factors of formation as listed in Table 7.1. As results from simulations for a single set of formation and fluid properties, we obtain the following conclusions that apply for specific scenarios evaluated:

(i) Fracture growth speed directly determines shape CO_2 flooded region and migration speed of flood front. Long fracture stretches flooding

region to a flat ellipse with long axis in the same direction with fracture, which results in an early breakthrough to storage site boundary and lowers the usage efficiency of storage site. On the other hand, short fracture almost does not change circle shape of flooding area and thus flood front grows slow with longer time to breakthrough storage site. Short fracture still provides high injectivity of injector compared to unfractured vertical injector.

(ii) At low injection rate, fracture tip does not reach flood front tip and fracture length is non-linear to injection rate; while at high injection rate, fracture tip overlaps flood front tip and fracture length is linear to injection rate.

(iii) Young's modulus is the main reason controlling fracture growth speed. In high Young's modulus formation, fracture grows faster and vice versa. Slow growing and short fractures result in a nearly circle flooded region and long breakthrough time; while fast growing and long fractures a quick breakthrough and low storage site usage efficiency.

(iv) Effect of Poisson's ratio is stronger on poro-elastic stress than on thermo-elastic stress. However, thermo-elastic stress is dominant to poro-elastic stress in fracture propagation pressure definition.

(v) Overpressured formation is not appropriate for CO_2 sequestration, as fracture grows very fast in that type of formation.

(vi) Fracture grows faster in high porosity formation where storage site usage efficiency is low.

(vii) Fracture grows faster in formation with low volumetric rock heat capacity.

(viii) Fracture grows slower in formation with high conductivity (*kh*). The influence of formation thickness is stronger than formation permeability on fracture growth.

(ix) Small size storage site provides better storage site usage efficiency as flooding region is more round.

(x) Compared to open system, closed system and infinite-acting system are more common and realistic. Open system assumption may overestimate fracture growth in early injection period and underestimate that in later injection period. Fracture grows fastest in closed system, which is underestimated with open boundary assumption. Even in closed system, if the site is large enough, fracture grows not faster than in systems with other types of boundaries in a considerably long time.

(xi) Fracture grows faster but flooded area is more round predicted by two-phase fractional flow model.

Table 7.1: Base case values for CO_2 injection induced fracture analysis

Injection operation properties	
Formation depth, D	1000 m
Formation thickness, h	50 m
Injection rate, q	2000 m^3/d
Injection period	10000 days
Wellhead CO_2 temperature, $T(0)$	15 °C
Earth surface temperature, $T_{fm}(0)$	20 °C
Wellbore radius, r_w	0.1 m
Storage formation radius, r_e	10,000 m
Formation rock properties	
Compressibility of rock grain, c_{gr}	2.2×10^{-11} Pa^{-1}
Compressibility of formation, c_f	4.8×10^{-10} Pa^{-1}
Young's modulus, E	12 GPa
Poisson's ratio, v	0.35
Thermoelasticity coefficient, α_T	1.0×10^{-5} K^{-1}
Rock tensile stress, σ_s	2 MPa
Geothermal gradient, G	30 °C/km
Formation permeability, k	100 md
Formation porosity, ϕ	0.25
Endpoint relative permeability CO_2 phase, k_{rg}	0.8
Unit volume rock grain heat capacity, $\rho_{gr}C_{gr}$	2340 kJ/(m^3-K)
Formation fluid properties	
Formation fluid density, ρ_w	1000 kg/m^3

Table 7.1, Cont'd

Mean density of CO_2, ρ_{co2}	800 kg/m^3
Compressibility of brine at subsurface condition, c_w	5.2×10^{-10} Pa^{-1}
Compressibility of CO_2 at subsurface condition, c_g	1.66×10^{-8} Pa^{-1}
Volumetric Specific heat capacity of brine, C_w	4200 kJ/(m^3-K)
Volumetric specific heat capacity of CO_2, C_{co2}	1200 kJ/(m^3-K)
Viscosity of warm brine in the formation, $\mu_{w,warm}$	4.3×10^{-4} Pa-s
Viscosity of cool brine in the formation, $\mu_{w,cool}$	7.0×10^{-4} Pa-s
Viscosity of warm CO_2 in the formation, $\mu_{g,warm}$	4.6×10^{-5} Pa-s
Viscosity of cool CO_2 in the formation, $\mu_{g,cool}$	8.0×10^{-5} Pa-s

Table 7.2: Sandstone Properties

$D_{brine\rightarrow BL}$	-0.0582
$D_{BL\rightarrow dry}$	1.0469
S_{wr}	0.4230
k_{rg}^{o}	0.2638
m	1.7
n	2.8

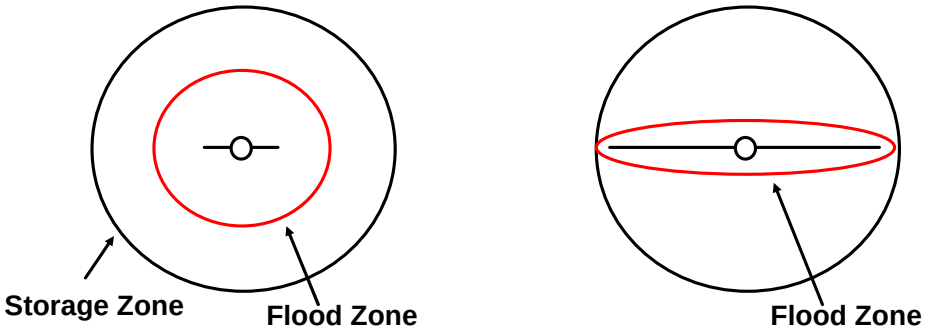

Figure 7.1: Sketch of injection induced fractures with different length and their corresponding geometry of CO_2 migration areas: (a) slow growth short fracture; (b) fast growth long fracture.

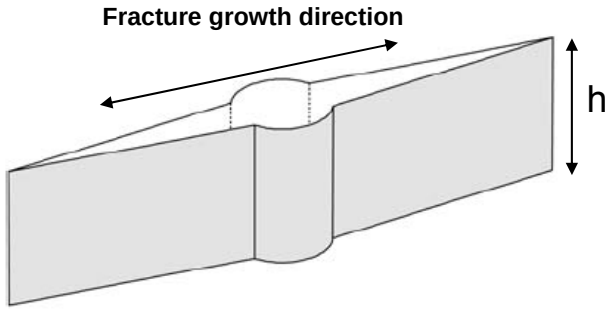

Figure 7.2: Sketch of injection induced vertical fracture from perforated portion of vertical injector

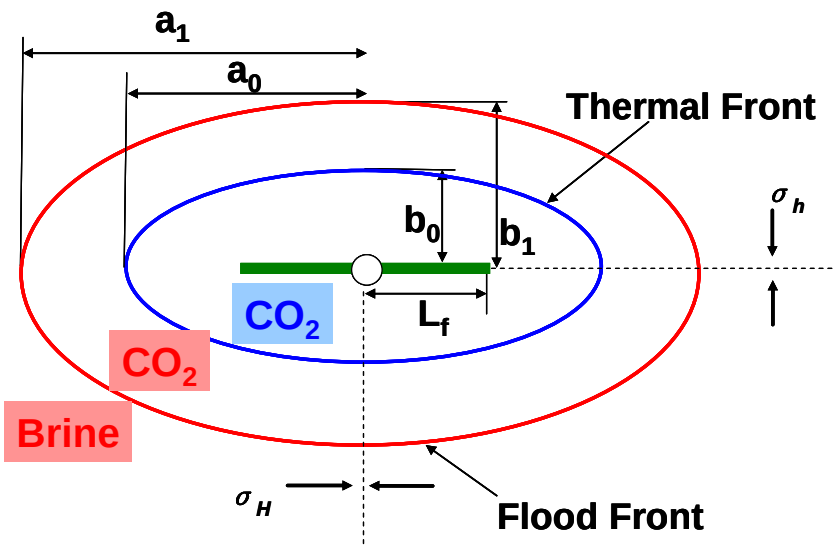

Figure 7.3: Map view showing a two-winged infinite conductivity vertical fracture (dark green line) of half length L_f oriented perpendicular to the plane of minimum horizontal stress. The two ellipses stand for thermal front (blue) and flood front (red) during CO_2 injection process, respectively. Fluids in CO_2 storage aquifer occupy three regions divided by the two fronts: a cool CO_2 zone between the fracture and the thermal front, warm CO_2 zone between thermal front and flood front, and warm brine zone beyond flood front

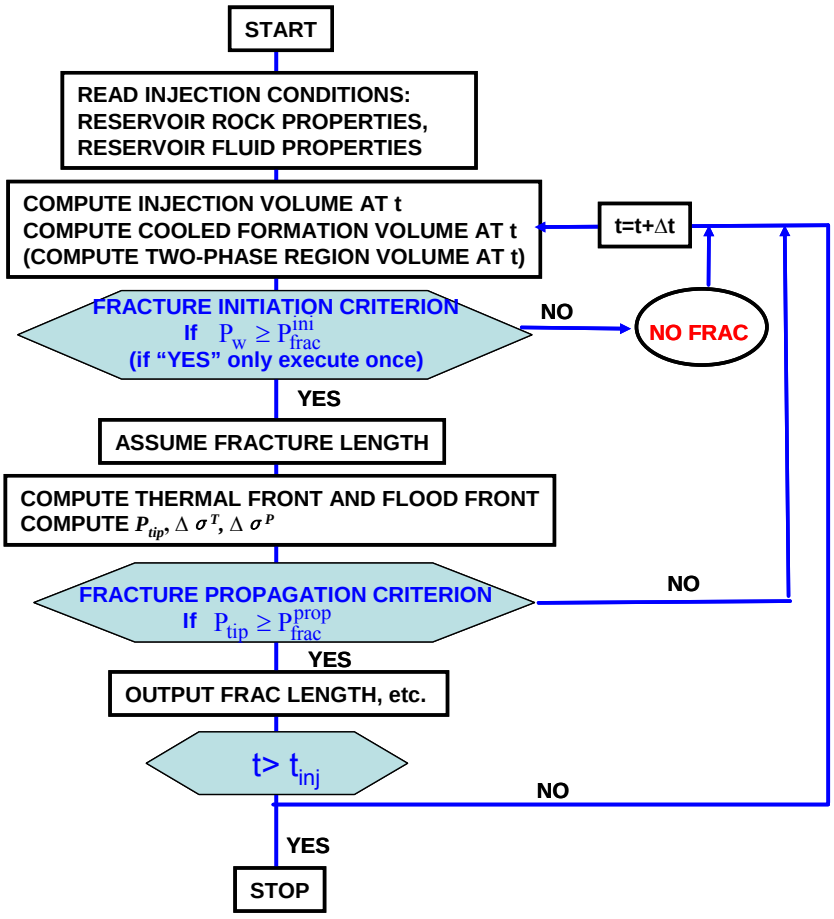

Figure 7.4: Flow chart of fracture growth modeling

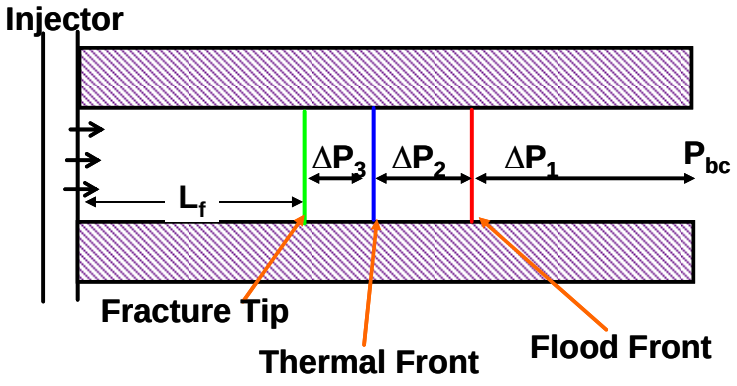

Figure 7.5: Side view of one wing of injection induced fractures and sketch of pressure drops in each zone (ref. Fig. 7.2). P_{bc} is pressure at drainage area boundary.

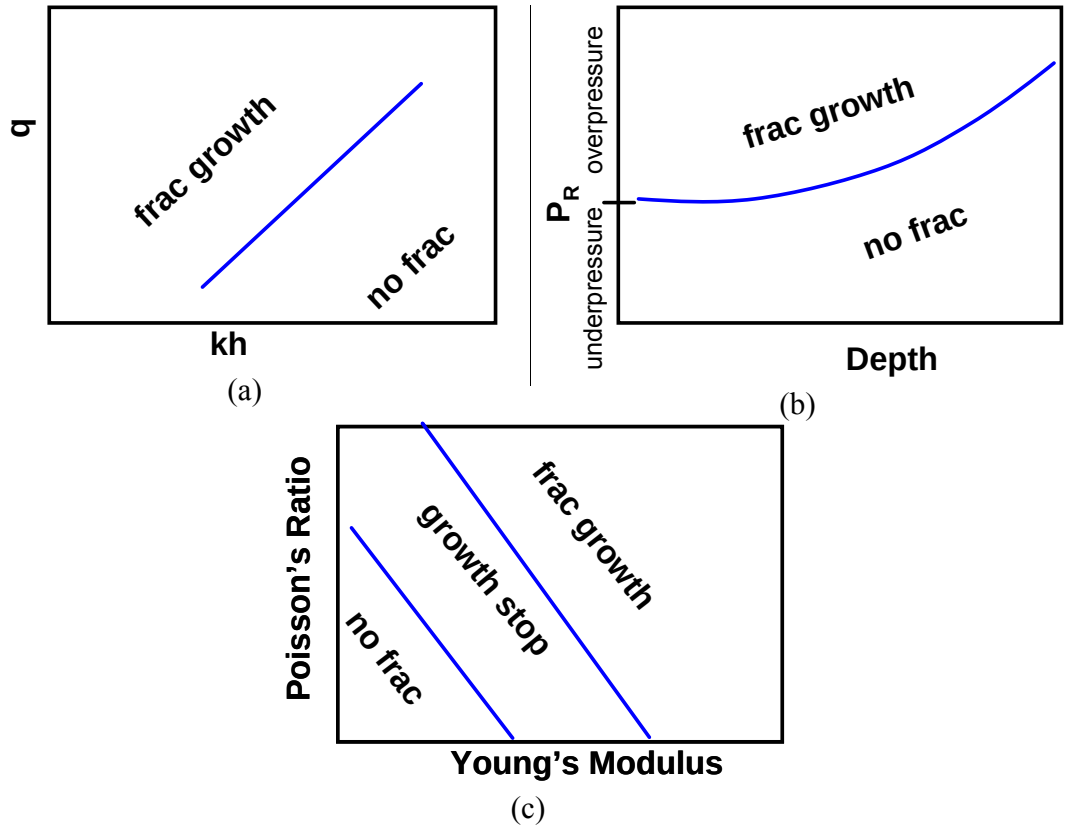

Figure 7.6: General behaviors of fracture growth regimes rely on: (a) injection rate and permeability-thickness of the formation; (b) formation pore pressure and depth; (c) Young's modulus and Poisson's ratio of rocks.

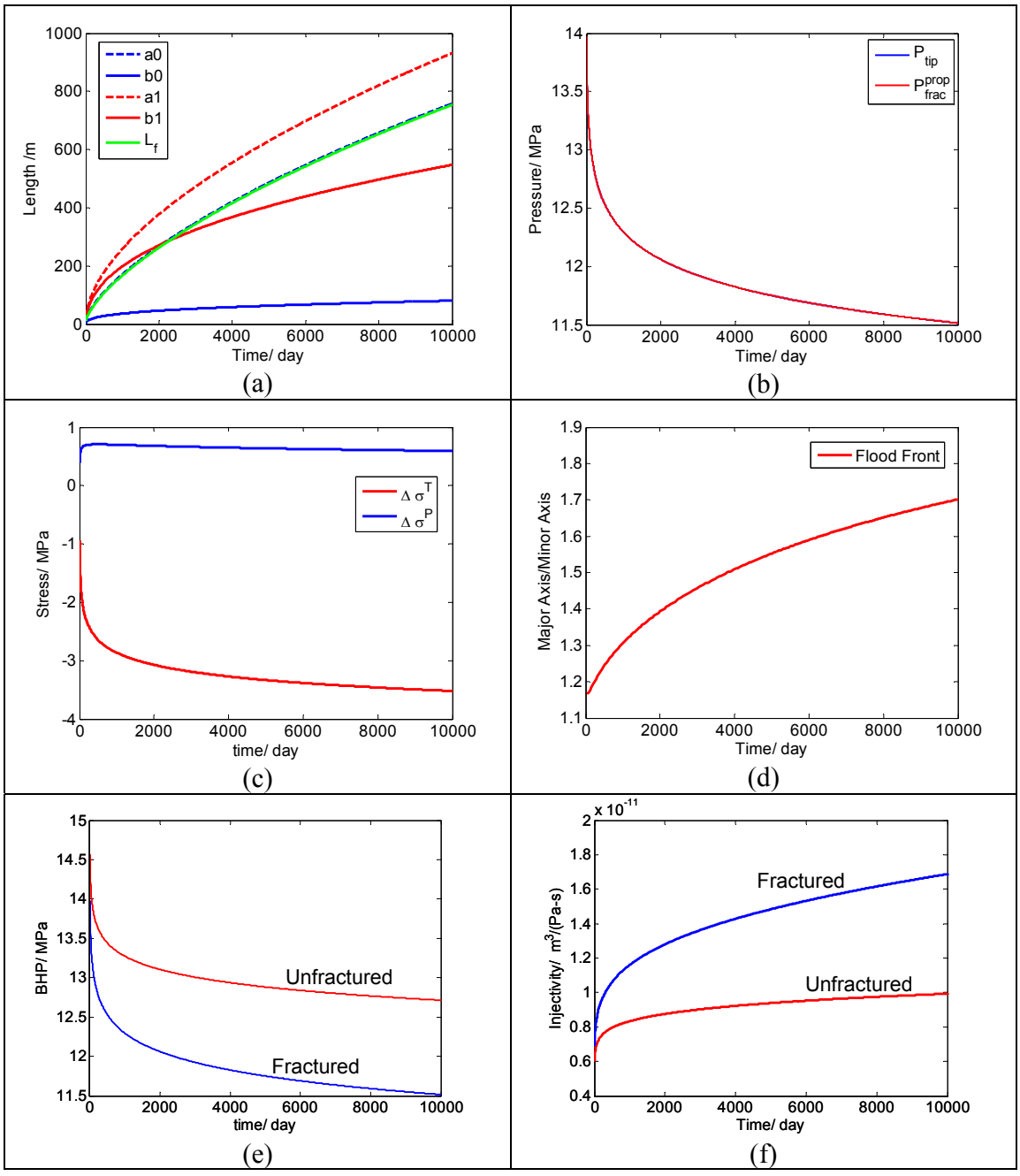
Length /m
Time/ day
a0
b0
a1
b1
L_f
(a)
Pressure/ MPa
Time/ day
P_{tip}
P^{prop}_{frac}
(b)
Stress/ MPa
time/ day
$\Delta\sigma^T$
$\Delta\sigma^P$
(c)
Major Axis/Minor Axis
Time/ day
Flood Front
(d)
BHP/ MPa
time/ day
Unfractured
Fractured
(e)
x 10^{-11}
Injectivity/ m^3/(Pa-s)
Time/ day
Fractured
Unfractured
(f)

Figure 7.7

Figure 7.7: Analysis of a case of CO_2 injection induced fracture growth: (a) fracture growth and fronts growth: green line stands for fracture length versus time, red dash line and solid line are major axis and minor axis of flood front, blue dash line and solid line are major axis and minor axis of thermal front; (b) fracture propagation pressure and pressure at fracture tip versus time, where they are almost identical; (c) thermo-elastic stress and poro-elastic stress at fracture tip versus time; (d) the ratio of major axis over minor axis of flood front versus time; (e) bottom hole pressure versus time of fractured and unfractured vertical injectors; (f) injectivity versus time of fractured and unfractured vertical injectors. Values of all parameters used here are given in Table 7.1.

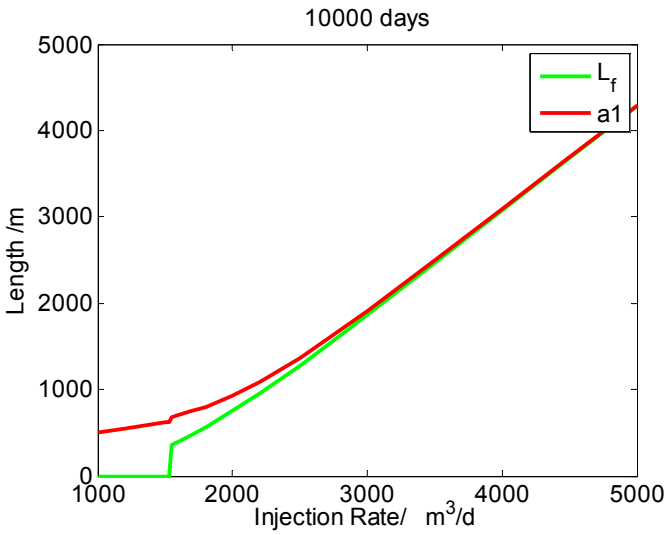

Figure 7.8: Fracture growth and major axis of flood front growth versus injection rate.

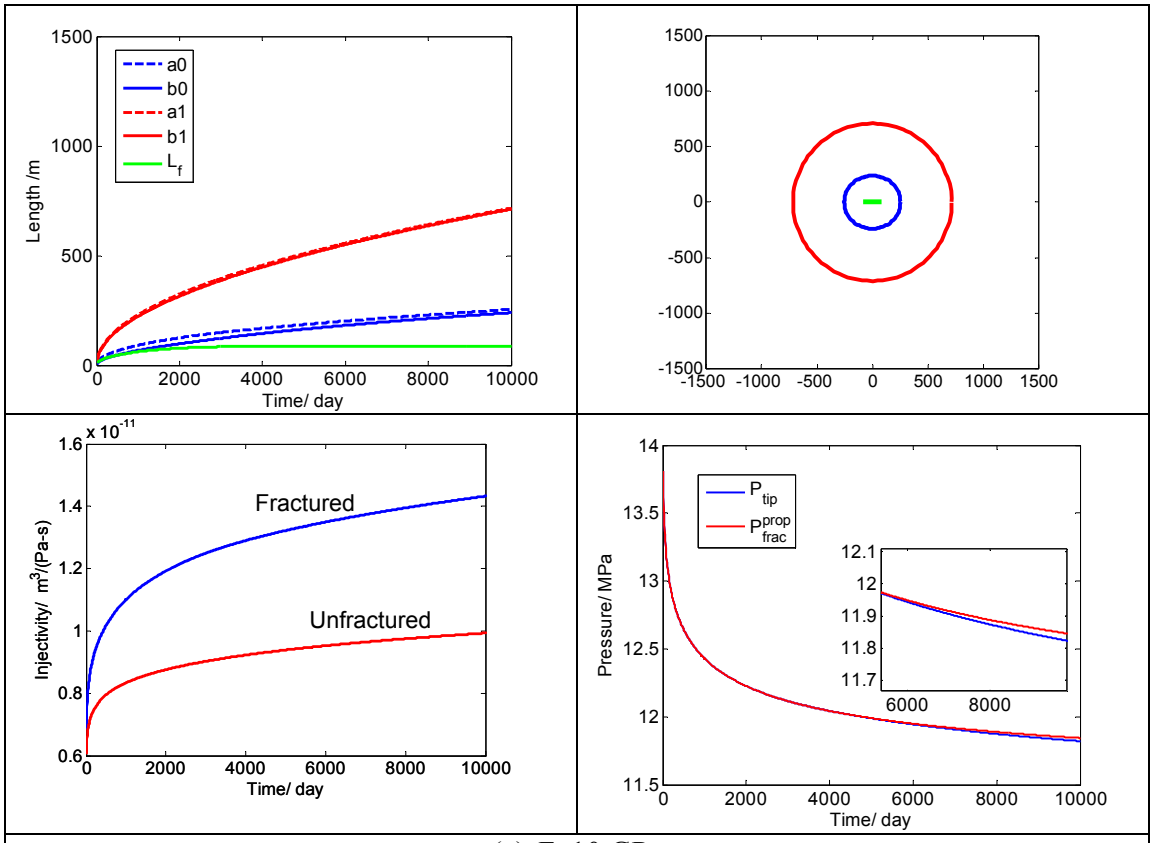

(a) E=10 GPa

(b) E=12 GPa

Figure 7.9

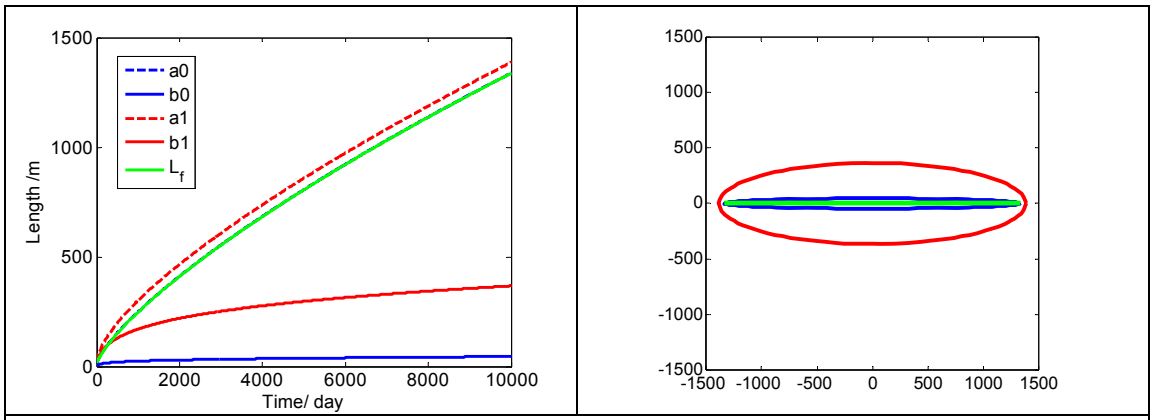

(c) E=14 GPa

Figure 7.9: The effect of Young's modulus of storage formation on fracture growth and shapes of flooded and cooled regions: (a) E=10 GPa; (b) E=12 GPa; (c) E=14 GPa. The left column shows fracture, thermal front, and flood front growth versus time; while the right column shows flooded and cooled regions evolution after 10,000 days CO_2 injection.

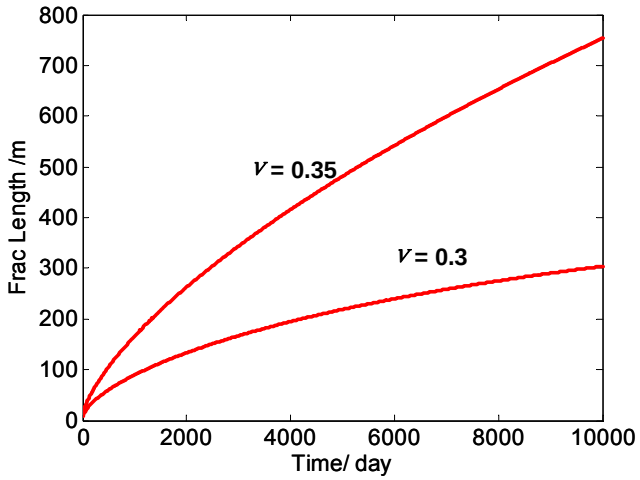

Figure 7.10: The effect of Poisson's ratio on fracture growth

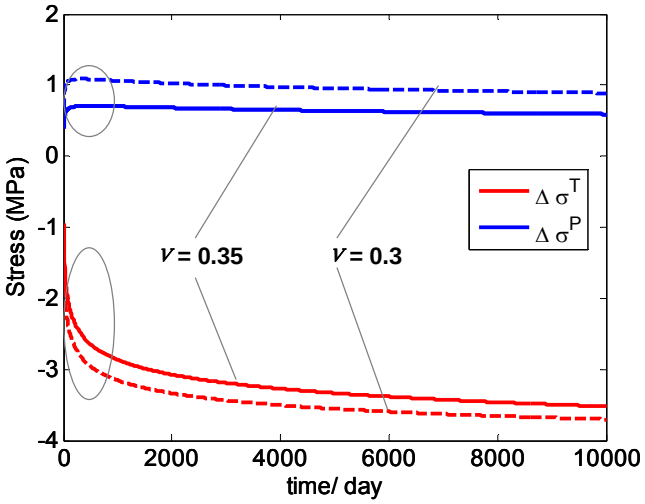

Figure 7.11: Thermo-elastic stress and poro-elastic stress at ν=0.3 and 0.35. The grey circle emphasize increment of poro-elastic stress is much larger than that of thermo-elastic stress at early period of injection.

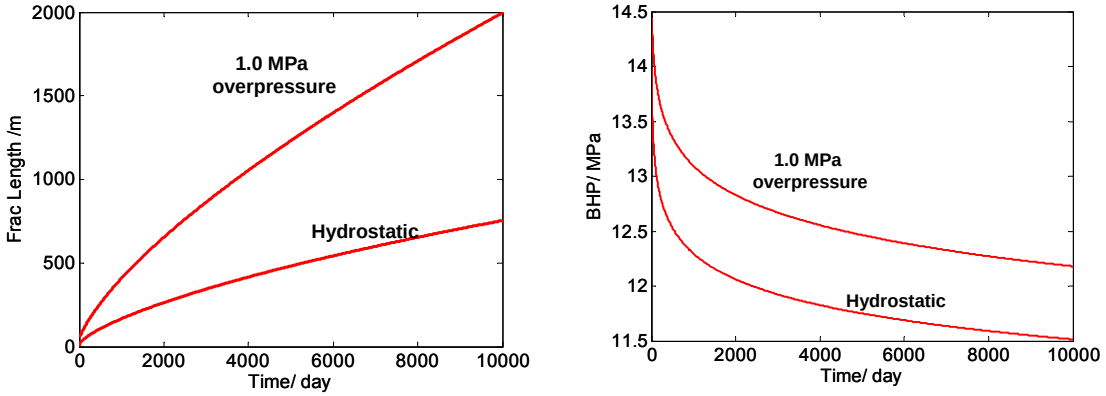

Figure 7.12: (a) The effect of formation pore pressure on fracture growth. Pore fluid density is ρ_f=1000 kg/m^3 in hydrostatic circumstance; while it is ρ_f=1100 kg/m^3 for 1 MPa overpressure formation; (b) bottom hole pressures of hydrostatic and overpressure formations

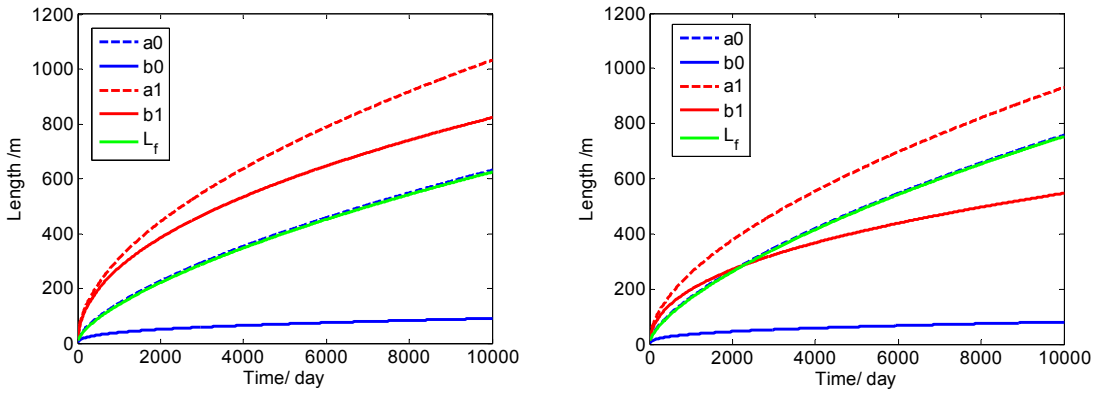

(a) (b)

Figure 7.13: The effect of porosity on cooled region volume: (a) $\phi = 0.15$; (b) $\phi = 0.25$. Porosity is relevant to total heat capacity of rock grains and thus the volume of cooled region. Low porosity means more grains, which stores higher heat than that in high porosity formation, and thus results in smaller cooled region volume.

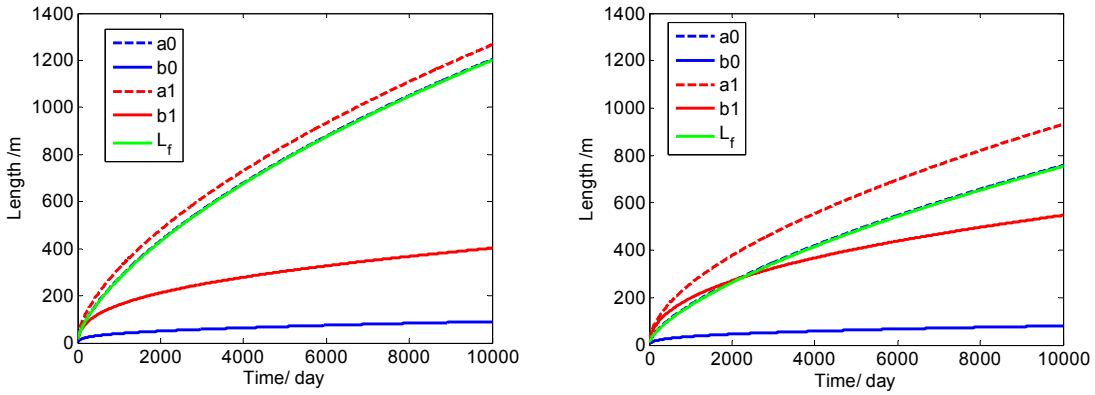

(a) (b)

Figure 7.14: The effect of rock unit volume heat capacity on fracture growth: (a) $\rho_{gr}C_{gr}$=1170 kJ/(m^3-K); (b) $\rho_{gr}C_{gr}$=2340 kJ/(m^3-K).

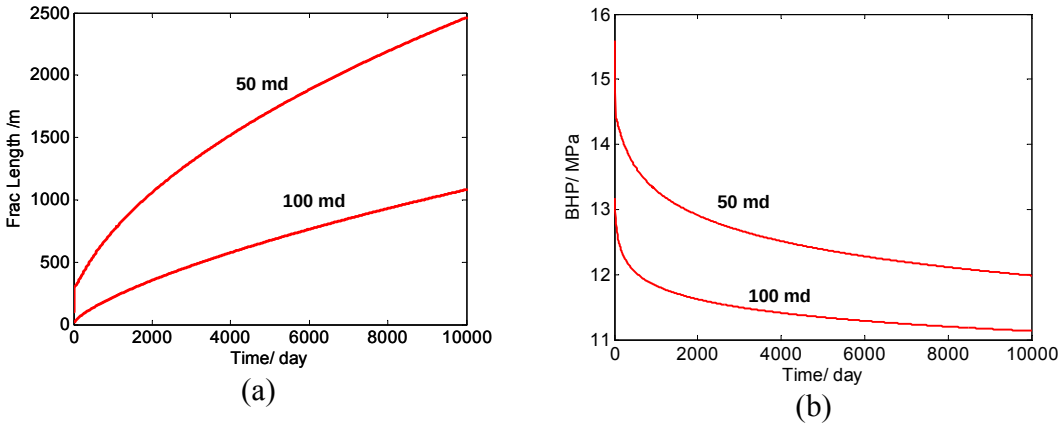

Figure 7.15: The effect of formation permeability on fracture growth. In this figure, we increase injection rate to 3500 m^3/d to ensure injection induced fracturing in 100md formation; (b) bottom hole pressures of 50md and 100md formations

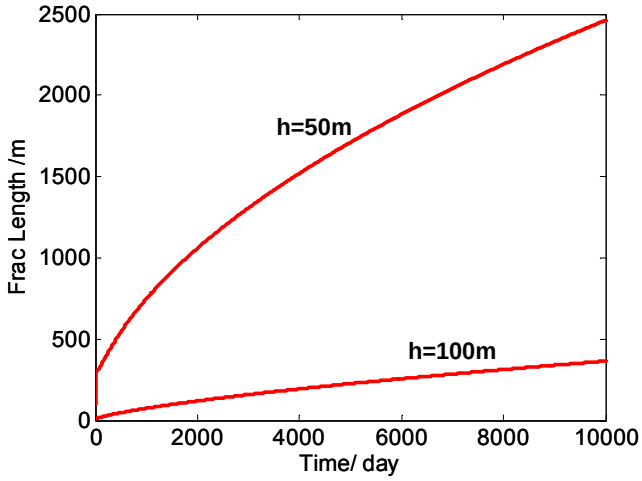

Figure 7.16: The effect of formation thickness on fracture growth.

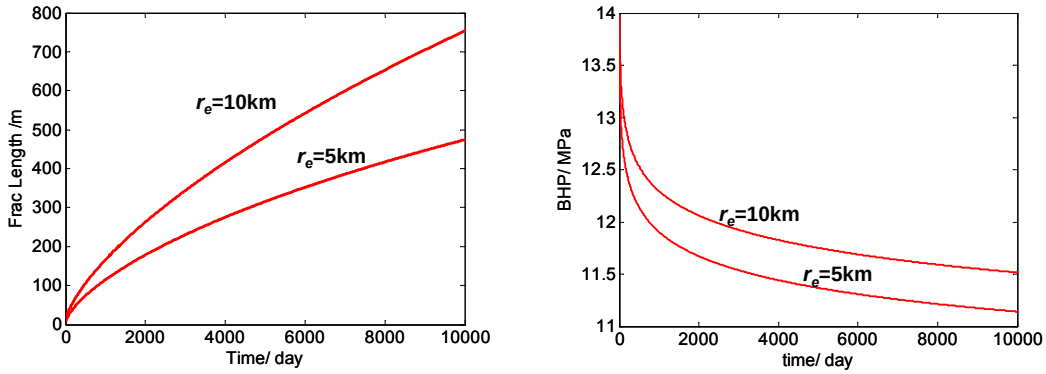

(a) (b)

Figure 7.17: The effect of formation drainage radius on bottom hole pressure in fracture propagation; (b) bottom hole pressures of formations with 5km and 10km drainage radius.

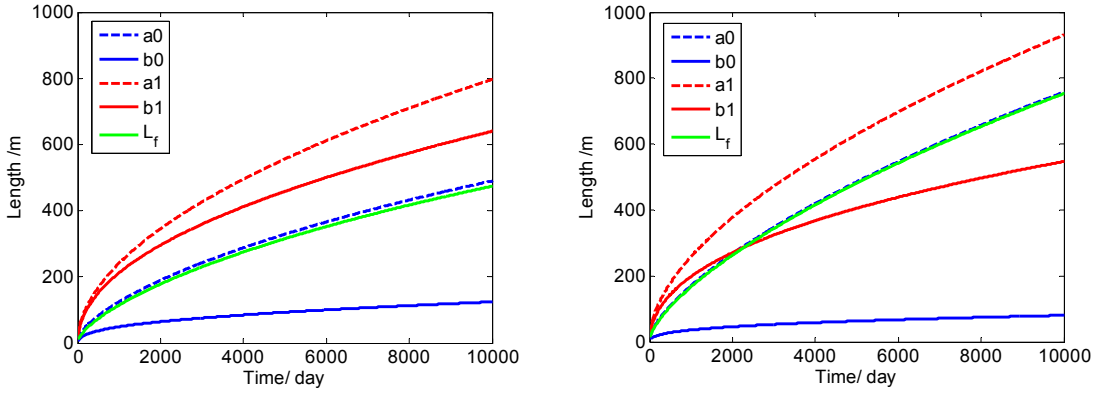

(a) (b)

Figure 7.18: The effect of formation drainage radius on fracture growth and injected CO_2 migration: (a) r_e=5km; (b) r_e=10km.

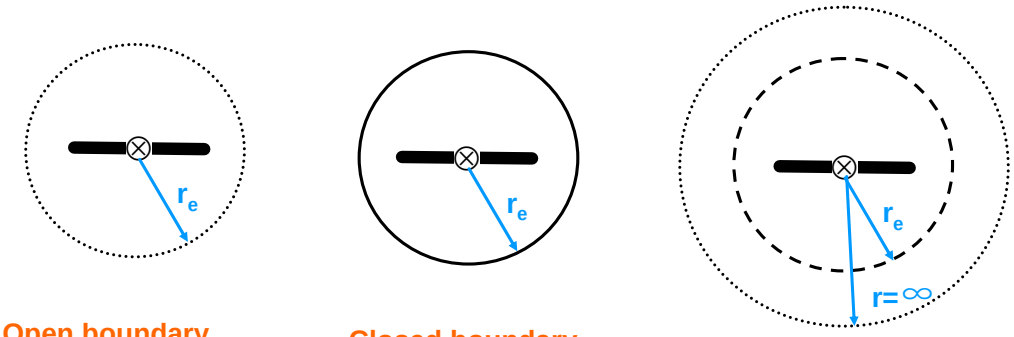

Open boundary
Constant pressure at boundary

$$(P)_{r_e} = \text{const}$$

$$\frac{\partial P}{\partial t} = 0$$

Closed boundary
No flow through boundary

$$\left(\frac{\partial P}{\partial r}\right)_{r_e} = 0$$

$$\frac{\partial P}{\partial t} = -\frac{q}{c_t A h \phi} \quad \text{const}$$

Infinite acting
Constant pressure at infinite distance
Pressure never "touch" infinite distance

$$(P)_{r\to\infty} = \text{const}$$

Figure 7.19: Sketch and conditions of various boundary system: (a) open system with constant pressure at boundary; (b) closed system with no-flow boundary; (c) infinite-acting system with constant pressure at infinite distance.

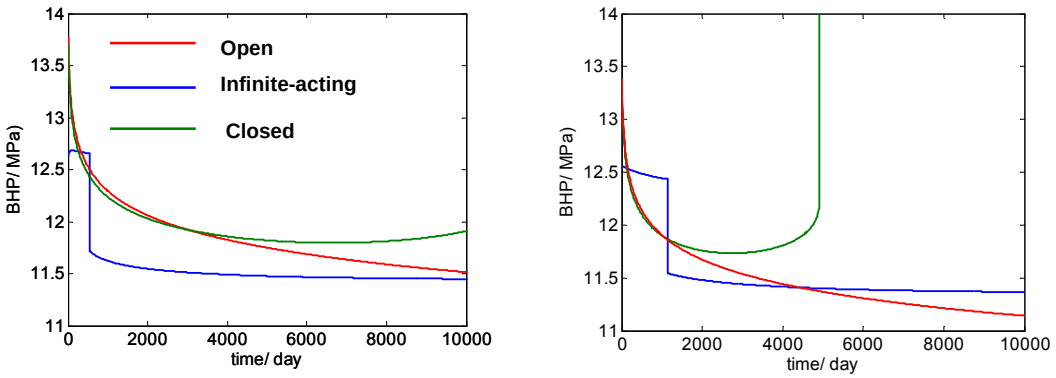

(a) (b)

Figure 7.20: Bottom hole pressure in fractured injector at various boundary systems for different size storage sites: (a) r_e=10km; (b) r_e =5km.

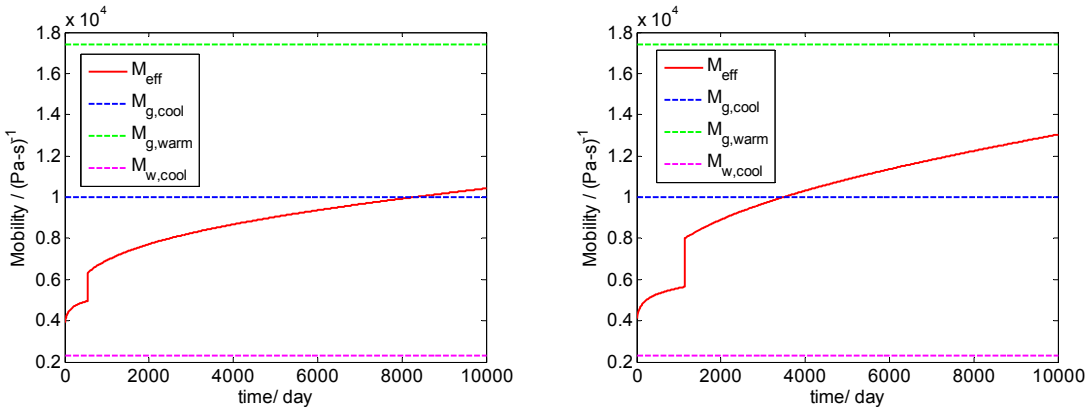

Figure 7.21: Effective mobility of entire CO_2-brine system under infinite-acting boundary condition: (a) r_e=10km; (b) r_e =5km. The meaning of parameters are defined in notation of Eq.(7.22).

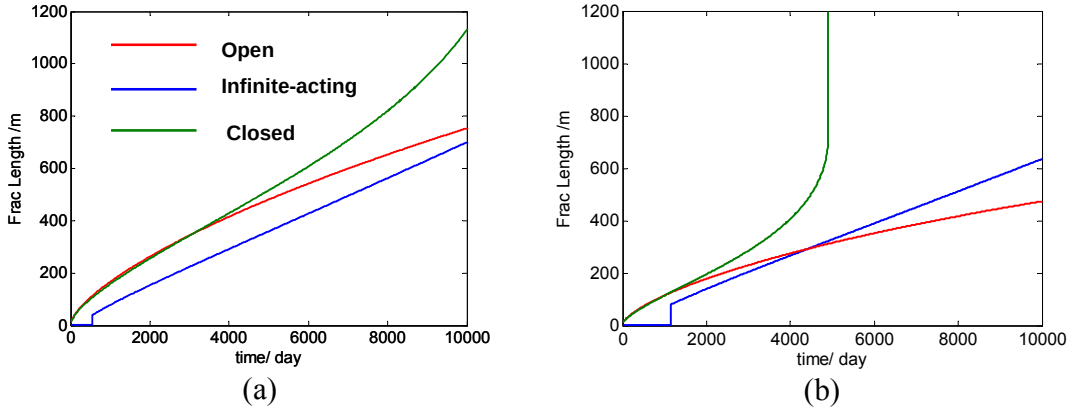

Figure 7.22: The effect of formation boundary condition on fracture growth for different size storage sites: (a) r_e=10km; (b) r_e =5km.

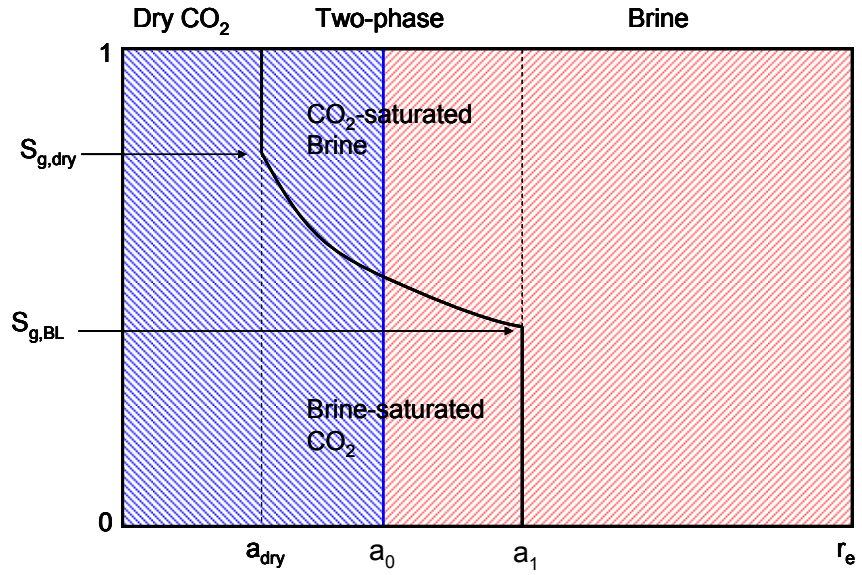

Figure 7.23: Four regions of CO_2 migration during injection with two-phase flow model. Besides pure CO_2 and brine zones, a two-phase zone of CO_2-brine mixture is designed with Buckley-Leverett Theory in elliptic coordinate system. The thermal front divides the entire formation to two parts, cooled zone (under blue shade) and warm zone (under red shade). The fractional flow curve modified to account for multiphase transport of CO_2-brine determines the positions of dry front (a_{dry}) and flood front (a_1) and the saturations in the two-phase Buckley-Leverett region.

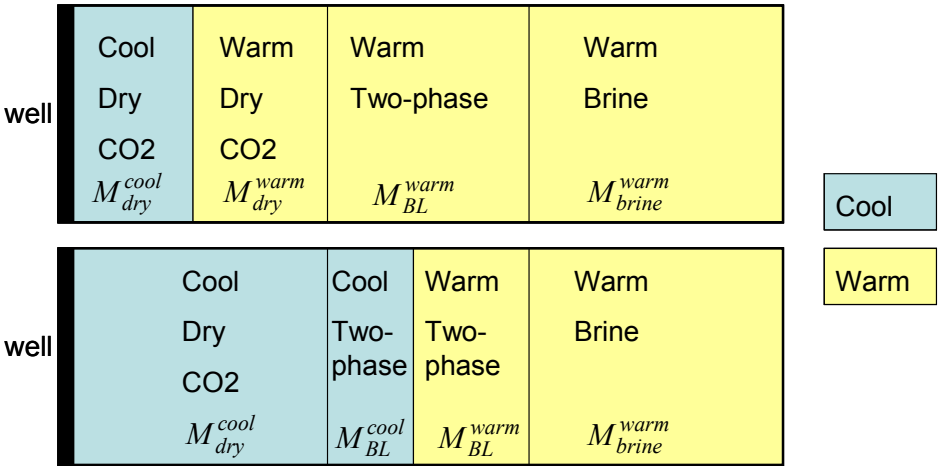

Figure 7.24: Two possible patterns of CO_2-brine displacement flow regions: (above) cool region (light blue) smaller than dry CO_2 region (light brown), as $V_T < V_{dry}$; (below) cool region larger than dry CO_2 region, as $V_T > V_{dry}$.

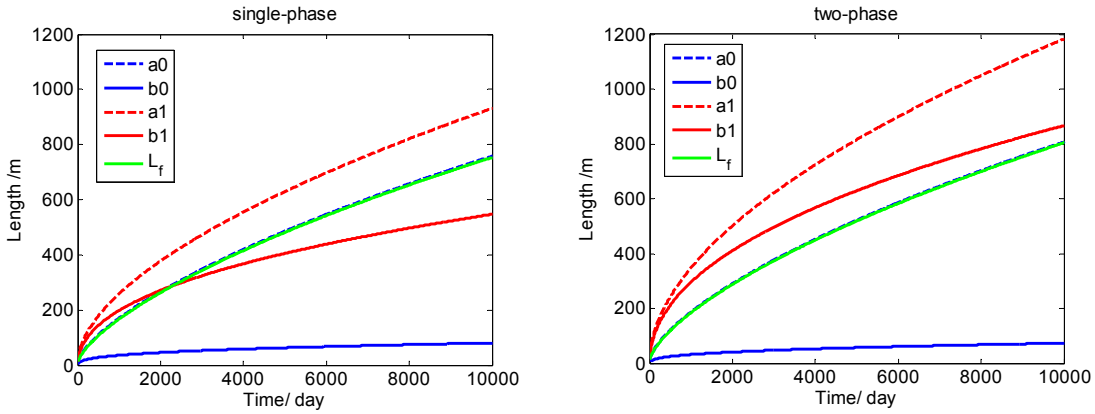

(a) (b)

Figure 7.25: Comparison of single-phase model with two-phase model on fracture growth and fronts growth with formation drainage radius, r_e =10km: (a) single phase; (b) two-phase.

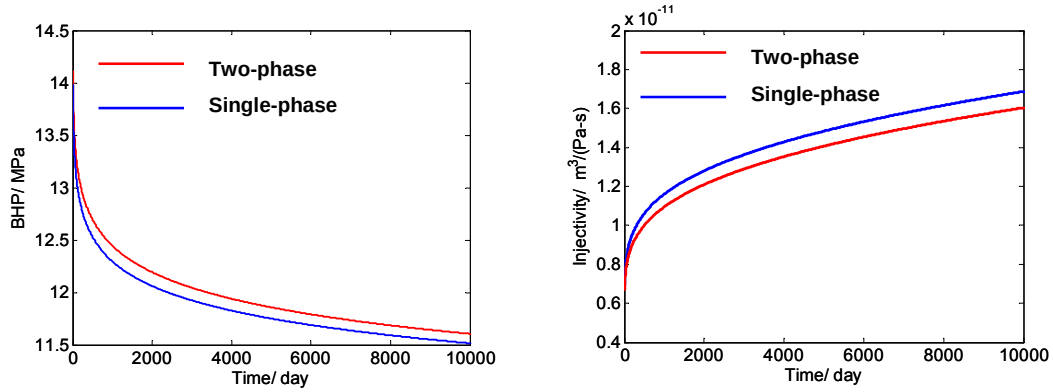

(a) (b)

Figure 7.26: Comparison of single-phase model with two-phase model on (a) bottom hole pressure and (b) injectivity of the case in Fig. 7.23.

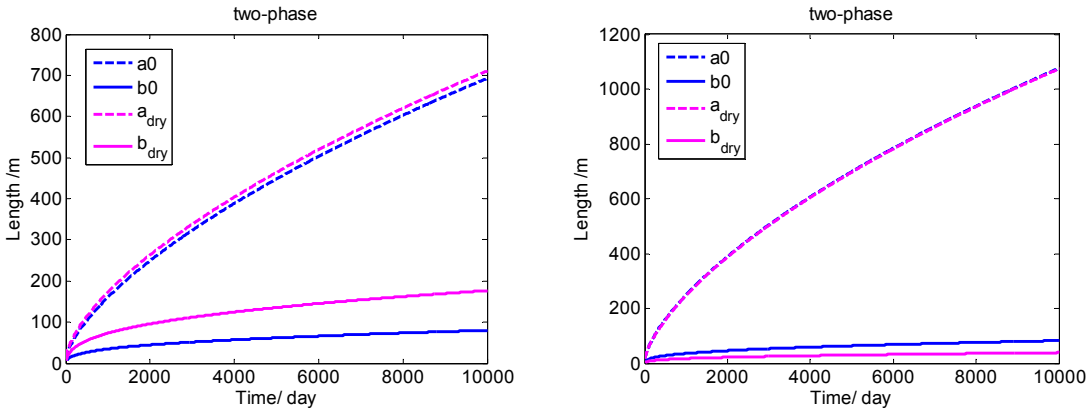

Figure 7.27: Two injection scenarios corresponds to the cases in Figure 7.22: (a) $V_{dry}>V_T$ with $\phi=0.1$, $\rho_{gr}C_{gr}$=2340 kJ/(m^3-K); (b) $V_{dry}<V_T$ with $\phi=0.3$, $\rho_{gr}C_{gr}$=1170 kJ/(m^3-K). Blue curves and magenta curves stand for the major and minor axes of thermal front and dry front (interface of pure CO_2 zone and two-phase zone).

Chapter 8 Summary, conclusions and future work

In this chapter, the works of this dissertation are summarized and conclusions are listed. Further, several recommendations are provided for future work.

8.1 SUMMARY AND CONCLUSIONS

In CO_2 sequestration projects, one potentially risky event is injection induced fractures. Fractures can be conduits for potential leakage which is risky and may not be accepted by regulators and public. Therefore, in some storage sites, regulators insist a no-fracture regulation for CO_2 sequestration projects. In this research, the major objective is to determine a criterion for injection induced fracture and to prevent fracture occurrence by screening out inappropriate sites and restricting operations, for example imposing a maximum safe injection rate. Large amount of CO_2 at high injection rate in storage formation may induce formation deformation due to the CO_2 cooling effect on surrounding rocks. As thermal induced stress reduces in-situ stress and thus lower fracture initiation and propagation pressure, fracture is easier to occur because of high rate injection. To avoid fracture, restriction on injection rate is inevitable. However, to satisfy requirement of large-scale commercial CO_2 sequestration projects, high injection rate is necessary. Hence, optimizations on increasing injection are performed.

To mathematically describe fracture initiation, we first deduce fracture criterion for rigorous case with no-fracture regulation based on bore hole stability analysis in Chapter 3. From the analysis, we know that injection induced fracture initiation pressure is determined by minimum in-situ stress, injection induced thermo-elastic stress and poro-elastic stress, and rock tensile strength. Among these factors, only thermo-elastic

stress and poro-elastic stress are related to injection operation, like injection rate. By comparing the above two stresses in several typical injection case, we find that they have opposite signs and the impact of thermo-elastic stress is much stronger than that of poro-elastic stress in CO_2 sequestration. Moreover, from the definition of thermo-elastic stress, we know that bore hole wall temperature change is a key factor. Therefore, to estimate thermo-elastic stress, bottom hole temperature prediction is necessary.

In Chapter 4, we build analytical steady state heat transfer model for predicting bottom hole temperature of vertical injector and horizontal injector. The model takes account correlation between overall heat transfer coefficient and injection rate for the case with dynamic injection rate or flow rate variation along horizontal wellbore. By dimensionless analysis and regression of data from Cranfield measurements, we identify the power law correlation with index as 0.8. The comparison of predicted bottom hole temperature with measurements shows that the model with this correlation can predict 87% bottom hole temperature within 2^oC errors. Based on the model, parametric analysis shows that formation depth, Stanton number, and CO_2 temperature at wellhead are major factors on bottom hole temperature. When wellhead temperature is close to surface temperature, temperature difference between bottom hole fluid and formation rocks decreases with storage increasing depth, until a critical depth; then it trends to a constant. The critical depth depends on other parameters, like Stanton number. Stanton number, which indicates the ratio of the rate of heat transfer to the rate of advective transport of enthalpy, depends on injection rate. Larger Stanton number yields smaller temperature difference. Wellhead temperature has a first order influence; pre-heating fluid at the wellhead can reduce or even entirely cancel temperature difference at bottom hole. In horizontal well model, we assume the entire wellbore is separated to a vertical segment and horizontal segment in which CO_2 uniformly leaks off and pressure does not vary

because of low viscosity of CO_2. Based on various scenarios, we find the largest temperature difference occurs at heel of horizontal segment, where fracture most probably initiates. Besides factors discussed for vertical segment, the length of horizontal segment is an additional factor related to temperature difference. The longer the horizontal segment, the longer part with high temperature difference along wellbore. Finally, Joule-Thomson cooling effect has been studied for CO_2 injection and storage in saline aquifer. The analysis shows that temperature change this effect is very tiny and can be ignored.

With the simple and accurate tool to predict bottom hole temperature of injected CO_2, we can estimate fracture initiation pressure with accounting impact of thermo-elastic effect for vertical injection in Chapter 5. By setting upper bound of bottom hole pressure as fracture initiation pressure, we can evaluate maximum injection rate under no-fracture regulation for CO_2 sequestration. According to this criterion, we conduct parametric analysis to qualitatively provide several conclusions on storage sites screening and operation optimizations for large-scale CO_2 sequestration projects. We may identify ideal formations for large-scale CO_2 injection and storage with following features: (i) low Young's modulus; (ii) low Poisson's ratio; (iii) low thermo-elasticity coefficient; (iv) intact formation with high rock tensile strength; (v) deep formation; (vi) low geothermal gradient; (vii) formation with high permeability and large thickness; (viii) small drainage area for single well; (iv) hydrostatic pore pressure formation. Among these properties, Young's modulus is the most important one. In formation with high Young's modulus, injection rate have to reduce by over 80% to avoid fracturing due to high thermo-elastic stress by high Young's modulus. Especially, the large impact of thermo-elastic effect due to high Young's modulus of formation is not easily to be cancelled by the advantage

provided by other parameters. For example, thermo-elastic effect negates the benefit of high injectivity provided by high formation permeability.

From analysis in Chapter 4 we know CO_2 bottom hole temperature is a function of CO_2 wellhead temperature, which may be the most feasible factor we can modify in practical operations. By pre-heating CO_2 before injection, injection can overcome impact of thermo-elastic effect and partially recover original injection rate especially in high Young's modulus formation. However, the benefit of pre-heating on injection rate is built on the capital of facility and energy consumption. Therefore, a balance between the cost and injection rate raise may need to be assessed before setting pre-heating procedure.

Due to the attractive high injectivity benefit, several CO_2 sequestration projects use horizontal injectors. We have discussed pros and cons of horizontal injectors through parametric analysis and comparisons with vertical injectors in Chapter 6. Impact of thermo-elastic effect is strong for horizontal injector and the correseponding injection rate limitation is usually unacceptable unless optimizations operation is applied. Horizontal injector is not economical for thick formations, formations with high permeability, and formation with large drainage radius compared with vertical injectors. In formation with high bulk density, horizontal injector is not desirable due to easy fracturing. Additionally, length of horizontal wellbore does not obviously benefit the maximum injection rate from economic perspective.

Due to huge impact of thermo-elastic effect on horizontal injectors, optimizations are necessary to increase the maximum injection rate. Partial perforation can increase injection rate several times by making the first portion of the horizontal well function as a heat exchanger for the CO_2 injected. The maximum injection rate declines with length of perforated wellbore. Pre-heating is valid and effective for improving the maximum injection rate for horizontal well injection. A threshold level of pre-heating for CO_2 is

necessary to lessen temperature difference in the formation and thus lower impact of thermo-elastic effect. Fracture initiation pressure at heel of horizontal injector is non-monotonic versus injection rate in some pre-heating cases with high wellhead temperature. In other words, high injection rate is necessary to diminish impact of thermo-elastic effect once CO_2 is pre-heated above a certain temperature at wellhead. Incremental maximum injection rate of horizontal injectors is non-linear to wellhead temperature; while it is linear for vertical injectors. As a result, the higher the increment of injection rate is, the more energy consumed per unit increment

If fractures are allowable, many more formations would be appropriate for CO_2 storage under this flexible regulation. Fracture growth strongly affects CO_2 migration in storage site. In Chapter 7, we provided a simple and low cost semi-analytical model to estimate injection induced fracture growth and migration of CO_2-brine system at various boundary conditions. Further, we improved the traditional injection induced fracture model from single phase flow to two phase fractional flow model, which more realistically describes the flow performance of CO_2 in storage site. As a result, we obtain the following conclusions:

(i) Fracture growth speed directly determines shape CO_2 flooded region and migration speed of flood front. Long fracture stretches flooding region to a flat ellipse with long axis in the same direction with fracture, which results an early breakthrough to storage site boundary and lowers the usage efficiency of storage site. On the other hand, short fracture almost does not change circle shape of flooding area and thus flood front grows slow with longer time to breakthrough storage site. Short fracture still provides high injectivity of injector compared to unfractured vertical injector.

(ii) At low injection rate, fracture tip does not reach flood front tip and fracture length is non-linear to injection rate; while at high injection rate, fracture tip overlaps flood front tip and fracture length is linear to injection rate.

(iii) Young's modulus is the main determinant factor controlling fracture growth speed. In high Young's modulus formation, fracture grows faster and vice versa. Slow growing and short fractures result in a nearly circle flooded region and long breakthrough time; while fast growing and long fractures a quick breakthrough and low storage site usage efficiency.

(iv) Effect of Poisson's ratio is stronger on poro-elastic stress than on thermo-elastic stress. However, thermo-elastic stress is dominant to poro-elastic stress in fracture propagation pressure definition.

(v) Overpressured formation is not appropriate for CO_2 sequestration, as fracture grows very fast in that type of formation.

(vi) Fracture grows faster in high porosity formation where storage site usage efficiency is low.

(vii) Fracture grows faster in formation with low volumetric rock heat capacity.

(viii) Fracture grows slower in formation with high conductivity (kh). The influence of formation thickness is stronger than formation permeability on fracture growth.

(ix) Small size storage site provides better storage site usage efficiency as flooding region is more round.

(x) Compared to open system, closed system and infinite-acting system are more common and realistic. Open system assumption may overestimate fracture growth in early injection period and underestimate that in later

injection period. Fracture grows fastest in closed system, which is underestimated with open boundary assumption. Even in closed system, if the site is large enough, fracture grows not faster than in systems with other types of boundaries in a considerably long time.

(xi) Fracture grows faster but flooded area is more round predicted by two-phase fractional flow model.

In sum, this work provides analytical tools which run fast for large numbers of potential CO_2 storage sites, enabling screening and evaluating the maximum injection rate for vertical and horizontal injectors under rigorous no-fracture regulation and evaluating fracture growth and CO_2 migration in flexible regulation. Although the results from analytical models on fracture growth and CO_2 migration are not as accurate as full physics numerical simulations, the models save lots of time on computation of coupling fracture mechanics with flow dynamics in porous media. Further, due to the simplicity of running the models, it is easy and appropriate for operators to arrange operation strategies on site based on the models.

Based on the applications of these tools, the risk of injection induced fracture during CO_2 sequestration is finally predictable and evitable and high injection rate requirement of large-scale commercial CO_2 sequestration project can be satisfied by suggested optimizations.

8.2 RECOMMENDATIONS FOR FUTURE WORK

Some improvements of my models and unaddressed issues related to fractures during CO_2 sequestration and could be future work of this study are presented in this section.

(i) In wellbore heat transfer model, we assume that temperature of surrounding formations along injector wellbore follows geothermal profile without considering the variation due to heat transferred from borehole fluid. In long time injection project, it indeed affects bottom hole temperature of injected CO_2 and makes it lower than current predicted.

(ii) Temperature change of formation rock around injector is not exactly a constant during long time injection, as heat is transferred from underburdon and overburden formations.

(iii) Single phase flow heat transfer model for heat transfer may not cover some injection cases with two-phase flow in wellbore.

(iv) Steady state model may be not accurate enough for predicting bottom hole temperature and pressure in early period during injection process.

(v) More concrete explanations on physical mechanism of fracture growth pattern are expected.

(vi) Validation of injection induced fracture model by field measurement and comprehensive numerical simulation is expected.

(vii) Natural pre-existing fracture re-activition due to CO_2 injection induced pressure and temperature change should be investigated.

(viii) More work on impact of anisotropy of rock properties are needed on geomechanics and fracture mechanics study for CO_2 sequestration.

(ix) Model of fracture growth from horizontal injector and injected CO_2 migration is expected.

(x) The integrity of cap rock due to injection induced stresses is an important topic for assessing risk of leakage in CO_2 sequestration.

Appendix A: Analytical Heat Transfer Model of Horizontal Well

In this appendix, we assume the temperature at the heel of horizontal well is already calculated from the previous vertical well model in section 4.2. We obtain the governing equation Eq. (A1), which describes heat transfer between wellbore fluid and surrounding rocks, similar to that of vertical well except that there is no effect of potential energy and the temperature of surrounding formations is a constant, T_R.

$$\frac{dT}{dx} = \frac{2\pi r_w U \left(T_R - T(x)\right)}{c_p \dot{m}(x)} \tag{A1}$$

Assuming CO_2 flows through perforation holes distributed along the horizontal wellbore, mass flow rate $\dot{m}(x)$ is no longer constant as in vertical wellbore model. It varies with position along the wellbore. Although CO_2 has no phase change in horizontal wellbore, its density (ρ) and specific heat capacity (c_p) vary along wellbore with temperature change at constant bore hole pressure (Fig. A.1). This is fairly different from the situation in vertical wellbore, where pressure and temperature both vary with depth and thus ρ and c_p do not change a lot (Fig. 4.2). Hence, the average value of c_p in Eq. (A1) can just result in an approximate solution of temperature profile along horizontal wellbore. From Fig A.1 we also know the higher wellbore pressure, the smaller changes of ρ and c_p along wellbore. The approximation solution of temperature profile will not influence the evaluation fracture initiation pressure a lot. As in Chapter 6, we use CO_2 temperature at heel to calculate thermo-elastic stress, where it has the largest value.

Two types of flow leakage models are built in this appendix. One is the commonly used uniform leak-off flux model (constant pressure along the wellbore); the other is non-uniform leak-off flux model (pressure drop along the wellbore), when the injection rate is high and wellbore radius is small. In both flux models, we identify the

safe perforation zones in different injection strategies, where the fluid pressure in the wellbore is lower than fracture initiation pressure of surrounding rocks.

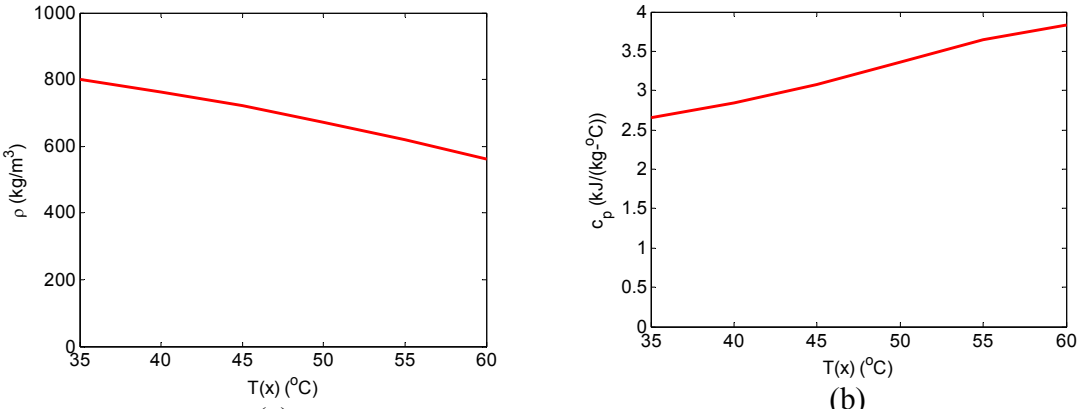

Figure A.1: (a) Variation of ρ of pure CO_2 in horizontal wellbore from heel to toe at constant bore hole pressure; (b) variation of c_p of pure CO_2 in horizontal wellbore from heel to toe at constant bore hole pressure. The values of bottom hole pressures and temperatures are selected from the typical range of injection.

A.1 UNIFORM FLUX MODEL

If the pressure in the wellbore is uniform, the entire wellbore is perforated or open hole, and reservoir pressure is homogeneous, then flux through perforation holes is uniform. This means the mass flow rate from the heel to the toe decrease linearly from $\dot{m}_0$ to zero, as

$$m(x) = \dot{m}_0 - ax \tag{A2}$$

where x=0, $m(0) = \dot{m}_0$; x=L, $m(L) = 0$ and $a = \dot{m}_0 / L$.

The boundary condition for Eq. (A1) is x=0, $T(0)$=T_{heel}, where T_{heel} is bottom hole temperature of vertical segment of well.

By assuming the surrounding formation temperature of the horizontal wellbore is T_R, and introduce overall heat transfer coefficient is function of injection rate $U = b\dot{m}^{0.8} + c$, we rearrange Eq. (A1),

$$\frac{dT}{dx} = \frac{2\pi r_w b(T_R - T)}{c_p \dot{m}_0^{0.2}(1 - x/L)^{0.2}} + \frac{2\pi r_w c(T_R - T)}{c_p \dot{m}_0 (1 - x/L)} \tag{A3}$$

Then we have solution of (A3),

$$\Delta T(x_D) = T_{res} - T(x) = \left(T_{fm}(0) - T(0)\right)(1 - x_D)^{\frac{2\pi r_w cL}{c_p \dot{m}_0}} \cdot \left[\left(1 - \frac{\alpha}{\beta}\right)e^{-\beta} + \frac{\alpha}{\beta}\right] \exp\left\{\frac{5}{2}\frac{\pi r_w bL}{c_p \dot{m}_0}\left[(1 - x_D)^{0.8} - 1\right]\right\} \tag{A4}$$

where $\alpha = \frac{G - g/c_p}{T_{fm}(0) - T(0)} D$ is a dimensionless temperature gradient, $\beta = \frac{2\pi r_w UD}{c_p \dot{m}_0}$ is a Stanton number, a dimensionless ratio of the rate of heat transfer to the rate of advective transport of enthalpy in vertical wellbore and D is the depth of the heel of the horizontal section, and dimensionless distance from heel $x_D = x/L$.

A.2 NON-UNIFORM FLUX MODEL

We assume the entire wellbore is perforated. When the flux into the reservoir is non-uniform along the wellbore, mass flow rate ($\dot{m}$) along the wellbore is a non-linear function of dimensionless friction factor (γ) and dimensionless position (x_D), which can be obtained by the following approach.

From (A1), we have

$$\frac{T_R - T(x)}{T_R - T(0)} = \exp\left[-\frac{2\pi r_w}{c_p}\int_0^x \frac{U(\dot{m})dx}{\dot{m}(x)}\right] \tag{A5}$$

To simplify this solution, we apply the similar dimensionless groups used in uniform flux model and have the following equations,

$$\frac{T_R - T(x)}{T_R - T(0)} = \exp\left[-\left(\frac{2\pi r_w bL}{c_p \dot{m}_0^{0.2}}\int_0^{x_D} \frac{dx_D}{\dot{m}_D^{0.2}(x_D, \gamma)} + \frac{2\pi r_w cL}{c_p \dot{m}_0}\int_0^{x_D} \frac{dx_D}{\dot{m}_D(x_D, \gamma)}\right)\right] \tag{A6}$$

$$\Delta T(x_D) = T_R - T(x) = \exp\left[-\left(\frac{2\pi r_w bL}{c_p \dot{m}_0^{0.2}} \int_0^{x_D} \frac{dx_D}{\dot{m}_D^{0.2}(x_D,\gamma)} + \frac{2\pi r_w cL}{c_p \dot{m}_0} \int_0^{x_D} \frac{dx_D}{\dot{m}_D(x_D,\gamma)} \right) \right] \cdot \left[\left(1 - \frac{\alpha}{\beta}\right) e^{-\beta} + \frac{\alpha}{\beta} \right] \left(T_{fm}(0) - T(0) \right) \quad \text{(A7)}$$

where $\dot{m}_D(x_D,\gamma) = \dot{m}(x/L)/\dot{m}_0$, $\gamma = \dfrac{2fk_H \dot{m}_0 L^2}{\pi\mu r_w^5 \left[\dfrac{L}{h} \ln \dfrac{4r_{eH}}{L} + \ln \dfrac{h}{2\pi r_w} \right]}$ is the dimensionless friction factor of the entire horizontal well and f is the conventional friction factor for flow along the horizontal section of the wellbore, as described next.

Since the pressure and mass flow rate are not constant along the horizontal wellbore, we use semi-analytical approach to calculate pressure and mass flow rate profile versus distance. First, we evaluate the value of Reynolds number of flow in the wellbore,

$$\mathrm{Re} = \frac{\rho u_r R_h}{\mu} \quad \text{(A8)}$$

and then we determine the approximate friction factor of the flow from the value of Reynolds number

$$f = \frac{15`}{\mathrm{Re}} \qquad \mathrm{Re} < 2100$$

$$f = \frac{0.0791}{\mathrm{Re}^{1/4}} \qquad 2100 < \mathrm{Re} < 10^5 \quad \text{(A9)}$$

$$f = -\left(3.6 * \log_{10} \left[\frac{6.9}{\mathrm{Re}} + \left(\frac{\varepsilon}{3.7} \right)^{10/9} \right] \right)^{-2} \qquad \mathrm{Re} > 10^5, 0 < \varepsilon < 0.05$$

From Borisov's horizontal well model, we have the relation between flow flux and pressure drop of element with length *dx*,

$$q(x) = \frac{2\pi k_H (dx)(P_w(x) - P_R)/(\mu B)}{\ln(4r_{eh}/L) + (h/L)\ln(h/(2\pi r_w))} \quad \text{(A10)}$$

$$\begin{cases} \dfrac{d\dot{m}}{dx} = -u_r(2\pi r_w)\rho \\ u_r(x) = q(x)/(2\pi r_w dx) = \lambda(P_w - P_R) \\ \dfrac{dP_w}{dx} = -\dfrac{1}{2}\rho u_t^2 f / R_h \\ u_t = \dfrac{\dot{m}(x)}{\rho\pi r_w^2} \end{cases} \tag{A11}$$

where $R_h = r_w / 2$, $\lambda = \dfrac{k_H}{\mu r_w \left[\dfrac{L}{h}\ln\dfrac{4r_{eH}}{L} + \ln\dfrac{h}{2\pi r_w}\right]}$, and assume CO_2 density is constant then B=1.

Combining equations in (A11), we have

$$\frac{d^2\dot{m}}{dx^2} = \frac{2fk_H}{\pi r_w^5 \mu\left[\dfrac{L}{h}\ln\dfrac{4r_{eH}}{L} + \ln\dfrac{h}{2\pi r_w}\right]}\dot{m}^2 \tag{A12}$$

with x=0, $m(0) = \dot{m}_0$; x=L, $m(L) = 0$.

We can have dimensionless form of (A12) as,

$$\frac{d^2\dot{m}_D}{dx_D^2} = \gamma\dot{m}_D^2 \tag{A13}$$

with $x_D = 0$, $\dot{m}_D(0) = 1$; $x_D = 1$, $\dot{m}_D(1) = 0$.

Under the above boundary conditions, we use Newton iteration method to numerically solve (A13), and substitute the result into (A7).

To simplify deduction, we set $\dot{m}_D = y$, $x_D = x$, $\gamma = A$.

Then (A13) can be written as $\dfrac{d^2y}{dx^2} = Ay^2$. Let $z = \dfrac{dy}{dx}$.

We have

$$\frac{dz}{dy}z = Ay^2$$

$$\frac{1}{2}z^2 = \frac{A}{3}y^3 + c$$

$$\frac{dy}{dx} = -\sqrt{\frac{2A}{3}y^3 + c}$$

$$\frac{dx}{dy} = -\frac{1}{\sqrt{\frac{2A}{3}y^3 + c}} = f(y,c) \tag{A14}$$

At the interval [0,1], discretize (A14) and obtain its numerical form,

$$y_j = j/N, j = 0,1,2,...N$$

$$\frac{x_j - x_{j-1}}{h} = \frac{1}{2}\left(f(c,y_{j-1}) + f(c,y_j)\right), j = 1,2,...N$$

where h=dy=1/N.

$$B.C. \qquad x_0 = 1, \quad x_N = 0$$

N unknown variables: $c, x_1, x_{2,}....x_{N-1}$

$$\sum_{j=1}^{n} \frac{h}{2}\left(f(c,y_{j-1}) + f(c,y_j)\right) = -1$$

$$F(c) = f(c,y_0) + f(c,y_N) + \sum_{j=1}^{N-1} 2\left(f(c,y_{j-1}) + f(c,y_j)\right) + \frac{2}{h} = 0$$

Newton iteration method:

$$c^{k+1} = c^k - F(c^k)/F'(c^k)$$

Then we have

$$x_m = x_0 + \sum_{j=1}^{m} \frac{h}{2}\left(f(c,y_{j-1}) + f(c,y_j)\right), m = 1,2,....N-1$$

It is important to choose proper initial value of c, else Newton iteration will not converge. First, give a test value of c to see F(c)> 0 or <0. Then, modify the value of c.

During the calculation (A13), we first assume an initial value of γ, then update γ in each iteration with new value of $\dot{m}_D$ until convergence.

Nomenclature

a_0	=	major semi-axis of the elliptical cool region
a_1	=	major semi-axis of the elliptical CO_2 flooded region
b_0	=	minor semi-axis of the elliptical cool region
b_1	=	minor semi-axis of the elliptical CO_2 flooded region
BHT	=	bottom hole temperature measurements
$Biot$	=	formation Biot's number
c_{gr}	=	compressibility of rock grain
c_f	=	compressibility of formation
c_w	=	compressibility of brine in storage formation
c_t	=	total compressibility of CO_2-brine system
c_g	=	compressibility of CO_2 in storage formation
Cco_2	=	volumetric Specific heat capacity of CO_2
C_{gr}	=	volumetric Specific heat capacity of rock grain
C_w	=	volumetric Specific heat capacity of brine
c_p	=	specific heat capacity
D	=	formation depth
E	=	Young's modulus
$f(a_0, b_0)$	=	geometry factor of thermal front
$f_{g,dry}$	=	fractional flow at dry front
$f_{g,BL}$	=	fractional flow at flood front (Buckley-Leverett front)
g	=	acceleration of gravity
G	=	geothermal gradient
h	=	CO_2 storage formation thickness
H	=	enthalpy of CO_2
J	=	injectivity
k	=	formation permeability
k_{rg}	=	end point relative permeability of CO_2 phase
k_{rw}	=	end point relative permeability of brine phase
K_{IC}	=	fracture toughness
L	=	length of horizontal wellbore
L_f	=	one wing fracture length
$\dot{m}$	=	mass injection rate
$\dot{m}_0$	=	mass flow rate at heel of horizontal wellbore
M_{eff}	=	effective mobility of CO_2-brine system
Nu	=	Nusselt number
P_f	=	pore pressure
$P_{hydrostat}$	=	hydrostatic formation pore pressure
P_R	=	initial formation pressure
P_{res}	=	far field reservoir pressure
Pr	=	Prandtl number

P_w	=	bottom hole fluid pressure
P_{frac}	=	fracture initiation pressure without accounting for impact of thermo-elastic effect
P_{frac}^T	=	fracture initiation pressure accounting for impact of thermo-elastic effect
P_{tip}	=	pressure at fracture tip
P_{bc}	=	boundary pressure of CO_2 storage formation
P_D	=	dimensionless pressure
q	=	volumetric injection rate
Q	=	heat transferred between wellbore fluid and surrounding formations
$Q(t)$	=	cumulative injected CO_2
Re	=	Renolds number
r_e	=	drainage radius
r_{eH}	=	horizontal well equivalent drainage radius
r_w	=	wellbore radius
s	=	skin factor
S_g	=	saturation of CO_2 in storage formation
$S_{g,ave}$	=	average CO_2 saturation in two-phase region
S_{wr}	=	residual
t	=	cumulative time during CO_2 injection
t_D	=	dimensionless time of open system
t_{DLf}	=	dimensionless time of infinite acting system
t_{DA}	=	dimensionless time of closed system
$T(z)$	=	temperature of CO_2 at depth z in wellbore
$T_{fm}(z)$	=	temperature of wellbore surrounding formation at depth z
T_{wh}	=	wellhead temperature
T_R	=	CO_2 storage formation temperature
$v_{D,dry}$	=	dimensionless speed of dry CO_2 front
$v_{D,BL}$	=	dimensionless speed of Buckley-Leverett front
V_{inj}	=	flooded region volume
V_T	=	volume cooled by injected CO_2
V_{dry}	=	volume of dry CO_2 region
V_e	=	drainage volume of the storage formation
x	=	distance from heel of horizontal wellbore
x_D	=	dimensionless distance from heel of horizontal wellbore
U	=	overall heat transfer coefficient
$<v>$	=	average velocity of CO_2 in wellbore
v_p	=	flow velocity through a perforation hole
WHT	=	wellhead temperature measurements
z	=	depth along wellbore

α	=	dimensionless temperature gradient
α_T	=	thermoelasticity coefficient
α_P	=	poroelasticity coefficient
β	=	Stanton number
β'	=	Stanton number at depth D
γ	=	dimensionless friction factor of entire horizontal wellbore
μ	=	bulk viscosity of CO_2 in wellbore
μ_{eff}	=	effective viscosity of CO_2-brine system
$\mu_{w,\ cool}$	=	viscosity of cool brine in storage formation
$\mu_{w,\ warm}$	=	viscosity of warm brine in storage formation
$\mu_{g,\ warm}$	=	viscosity of warm CO_2 in storage formation
$\mu_{w,\ cool}$	=	viscosity of cool CO_2 in storage formation
θ	=	angle measured from direction of maximum horizontal stress
ν	=	Poisson's ratio
ρ	=	density of CO_2 at storage formation
ρ_f	=	formation pore fluid density
ρ_w	=	density of brine in storage formation
ρ_{gr}	=	density of rock grain in storage formation
ρ_{fm}	=	formation bulk density
σ	=	effective stress
σ_h	=	in-situ minimum horizontal stress
σ_H	=	in-situ maximum horizontal stress
σ_v	=	in-situ vertical stress
σ_s	=	rock tensile strength
σ_θ	=	tangential stress at the borehole wall
$\Delta\sigma^T$	=	injection induced thermo-elastic stress
$\Delta\sigma^P$	=	injection induced poro-elastic stress
ΔP	=	pressure change (current – initial)
ΔP_{perf}	=	pressure drop due to flow of CO_2 through a perforation
ΔT_{perf}	=	temperature drop due to flow of CO_2 through a perforation
ΔT	=	temperature change (current – initial)
ϕ	=	formation porosity

References

Alves, I. N., Alhanati, F. J. S., & Shoham, O. (1992). A Unified Model for Predicting Flowing Temperature Distribution. in Wellbores and Pipelines. *SPE production engineering*, *7*(4), 363-367.

Al-Shayea, N. A., Khan, K., & ABDURAHEEM, A. (2001). Fracture toughness vs. tensile strength for reservoir rocks from Saudi Arabia. *Frontiers of rock mechanics and sustainable development in the 21st century*, 169.

Bachu, S., Gunter, W. D., and E. H. Perkins. (1994). Aquifer disposal of CO_2 Hydrodynamic and mineral trapping. *Energy Conversion and Management* 35.4 : 269-279.

Bachu, S. (2003). Screening and ranking of sedimentary basins for sequestration of CO_2 in geological media in response to climate change.*Environmental Geology*, *44*(3), 277-289.

Benson, S. M., & Cole, D. R. (2008). CO_2 sequestration in deep sedimentary formations. *Elements*, *4*(5), 325-331.

Bergman, P. (1999) Geological sequestration of CO_2: a status report."*Greenhouse Gas Control Technologies*: 169-173.

Bielinski, A. (2007). Numerical simulation of CO_2 sequestration in geological formations.

Biot, M. A., & Willis, D. G. (1957). The elastic coefficients of the theory of consolidation. *J. appl. Mech*, *24*(594-601), 206.

Borisov, J. P. (1984). Oil production using horizontal and multiple deviation wells, Nedra, Moscow. *Translated into English by Strauss J, Edited by Joshi S D. Philips*.

Breckels, I. M., & Eekelen, H. V. (1982). Relationship between horizontal stress and depth in sedimentary basins. *Journal of Petroleum Technology*,*34*(9), 2191-2199.

Bryant, S. (2007). Geologic CO_2 Storage? Can the Oil and Gas Industry Help Save the Planet?. *Journal of Petroleum Technology*, *59*(9), 98-105.

Burnett, E. S., & Roebuck, J. R. (1910). On a Radial Flow Porous Plug and Calorimeter. *Physical Review (Series I)*, *30*(4), 529.

Burton, M., Kumar, N., & Bryant, S. (2008, April). Time-dependent injectivity during CO_2 storage in aquifers. In *SPE/DOE Symposium on Improved Oil Recovery*.

Chang, K. W., Minkoff, S., & Bryant, S. (2008, September). Modeling leakage through faults of CO_2 stored in an aquifer. In *SPE Annual Technical Conference and Exhibition*.

Chin, L. Y., Rajagopal, R., & Thomas, L. K. (2000). Fully coupled geomechanics and fluid-flow analysis of wells with stress-dependent permeability. *Spe Journal*, *5*(1), 32-45.

Cinco-Ley, H., & Samaniego-V, F. (1981). Transient pressure analysis for fractured wells. *Journal of petroleum technology*, *33*(9), 1749-1766.

Clifford, P. J. (1989, July). Simulation of Waterflood Fracture Growth with Coupled Fluid Flow, Temperature and Rock Elasticity. In 1st European Conference on the Mathematics of Oil Recovery.

Clifford, P. J., Berry, P. J., & Gu, H. (1991). Modeling the vertical confinement of injection-well thermal fractures. *SPE production engineering*, *6*(4), 377-383.

Detournay, E., & Cheng, A. (1992). Influence of pressurization rate on the magnitude of the breakdown pressure. In *Proc. 33nd US Rock Mechanics Symposium, Balkema*.

Eaton, B. (1969). Fracture gradient prediction and its application in oilfield operations. *Journal of petroleum technology*, 21(10), 1353-1360.

Garon, A. M., Lin, C. Y., & Dunayevsky, V. A. (1988, March). Simulation of Thermally Induced Waterflood Fracturing in Prudhoe Bay. In *SPE California Regional Meeting*.

Gor, G. Y., Stone, H. A., & Prevost, J. H. (2012). Fracture Propagation Driven by Fluid Outflow from a Low-permeability Aquifer. *arXiv preprint arXiv:1203.4543*.

Gringarten, A. C., Ramey Jr, H. J., & Raghavan, R. (1972). *Pressure analysis for fractured wells* (No. CONF-7210140-).

Gringarten, A., Henry J, R., & Raghavan, R. (1974). Unsteady-state pressure distributions created by a well with a single infinite-conductivity vertical fracture.*Old SPE Journal*, *14*(4), 347-360.

Hagoort, J., Weatherill, B., & Settari, A. (1980). Modeling the propagation of waterflood-induced hydraulic fractures. *Old SPE Journal*, *20*(4), 293-303.

Hasan, A. R., Kabir, C. S., & Sarica, C. (2002). *Fluid flow and heat transfer in wellbores*. Richardson, TX: Society of Petroleum Engineers.

Heinemann, N., Wilkinson, M., Haszeldine, R. S., Fallick, A. E., & Pickup, G. E. (2013). CO_2 sequestration in a UK North Sea analogue for geological carbon storage. *Geology*, *41*(4), 411-414.

Houghton, J. T., et al. (1997). Implications of Proposed CO_2 Emissions Limitations. *Technical Paper IV, IPCC, Geneva, Switzerland* .

Hovorka, S. D., Benson, S. M., Doughty, C., Freifeld, B. M., Sakurai, S., Daley, T. M., & Knauss, K. G. (2006). Measuring permanence of CO_2 storage in saline formations: the Frio experiment. *Environmental Geosciences*,*13*(2), 105-121.

Hustedt, B., Zwarts, D., Bjoerndal, H. P., Al-Masfry, R., & van den Hoek, P. (2008). Induced fracturing in reservoir simulations: application of a new coupled simulator to a waterflooding field example. *SPE Reservoir Evaluation & Engineering*, *11*(3), 569-576.

IEA (2006) World Energy Outlook 2006. IEA/OECD, Paris, France.

IPCC (2005) Underground geological storage. In: Metz B, Davidson O, de Coninck HC, Loos M, Meyer LA (eds) IPCC Special Report on Carbon Dioxide Capture and Storage, prepared by Working Group III of the Intergovernmental Panel on Climate Change. Cambridge University Press, Cambridge, UK, and New York, USA, pp 195-276

IPCC (2007). Climate Change 2007: Mitigation. Contribution of Working Group III to the Fourth Assessment Report of the Intergovernmental Panel on Climate Change. Cambridge, UK: Cambridge University Press.

Izgec, O., Demiral, B., Bertin, H., & Akin, S. (2006, September). Experimental and numerical modeling of direct injection of CO_2 into carbonate formations. In*SPE Annual Technical Conference and Exhibition*.

Ji, L., Settari, A., & Sullivan, R. (2007, November). A Novel Hydraulic Fracturing Model Fully Coupled with Geomechanics and Reservoir Simulator. In *SPE Annual Technical Conference and Exhibition*.

Joshi, S. D. (1991). *Horizontal well technology*. PennWell Corporation.

Kumar, A., Noh, M. H., Sepehrnoori, K., Pope, G. A., Bryant, S. L., & Lake, L. W. (2005). Simulating CO2 storage in deep saline aquifers, Carbon Dioxide Capture for Storage in Deep Geologic Formations-Results from the CO_2 Capture Project, v. 2: Geologic Storage of Carbon Dioxide with Monitoring and Verification, SM Benson.

Lienhard IV, J. H., Lienhard, J. H., & V A, H. T. T. (2006). Cam-bridge.

Lindeberg, E. (2011). Modelling pressure and temperature profile in a CO_2 injection well. *Energy Procedia*, *4*, 3935-3941.

Luo, Z., & Bryant, S. (2010, November). Influence of thermo-elastic stress on CO_2 injection induced fractures during storage. In *SPE International Conference on CO_2 Capture, Storage, and Utilization*.

Luo, Z., & Bryant, S. (2011, November). Influence of Thermoelastic Stress on Fracturing a Horizontal Injector During Geological CO_2 Storage. In *Canadian Unconventional Resources Conference*.

Luo, Z., & Bryant, S. (2011). Influence of thermo-elastic stress on fracture initiation during CO_2 injection and storage. *Energy Procedia*, *4*, 3714-3721.

Mathias, S. A., Gluyas, J. G., Oldenburg, C. M., & Tsang, C. F. (2010). Analytical solution for Joule–Thomson cooling during CO_2 geo-sequestration in depleted oil and gas reservoirs. *International Journal of Greenhouse Gas Control*, *4*(5), 806-810.

Noh, M., Lake, L., Bryant, S., & Araque-Martinez, A. (2007). Implications of coupling fractional flow and geochemistry for CO_2 injection in aquifers. *SPE Reservoir Evaluation & Engineering*, *10*(4), 406-414.

Oldenburg, C. M. (2007). Joule-Thomson cooling due to CO_2 injection into natural gas reservoirs. *Energy Conversion and Management*, *48*(6), 1808-1815.

Orr, F. (2004). Storage of carbon dioxide in geologic formations. *Journal of Petroleum Technology*, *56*(9), 90-97.

Perkins, T. K., & Gonzalez, J. A. (1985). The effect of thermoelastic stresses on injection well fracturing. *Old SPE Journal*, *25*(1), 78-88.

Pruess, K. (2005). Numerical studies of fluid leakage from a geologic disposal reservoir for CO_2 show self‐limiting feedback between fluid flow and heat transfer. *Geophysical research letters* 32.14.

Pruess, K. (2008). On CO_2 fluid flow and heat transfer behavior in the subsurface, following leakage from a geologic storage reservoir. *Environmental Geology*, *54*(8), 1677-1686.

Rahman, K., & Khaksar, A. (2012, October). Fracture Growth and Injectivity Issues for Produced Water Reinjection Wells C"" Case Studies with Fields from offshore Australia and UK North Sea. In *SPE Asia Pacific Oil and Gas Conference and Exhibition*.

Ramey, H.J. (1962). Wellbore heat transmission. *Journal of Petroleum Technology*,*14*(4), 427-435.

Rodrigues, L., Cunha, L., & Chalaturnyk, R. (2009, October). Coupled Reservoir Flow Simulation: Fault Leakage Analysis. In *SPE Annual Technical Conference and Exhibition*.

Saadatpoor, E., Bryant, S. L., & Sepehrnoori, K. (2010). New trapping mechanism in carbon sequestration. *Transport in Porous Media*, *82*(1), 3-17.

Sadd, M. H. (2009). *Elasticity: theory, applications, and numerics*. Access Online via Elsevier.

Saripalli, K., Bryant, S., & Sharma, M. (1999, March). Role of fracture face and formation plugging in injection well fracturing and injectivity decline. In*SPE/EPA Exploration and Production Environmental Conference*.

Satter, A. (1965). Heat losses during flow of steam down a wellbore. *Journal of Petroleum Technology*, *17*(7), 845-851.

Schlumberger, M., Perebinossoff, A. A., & Doll, H. G. (1936). *Temperature measurements in oil wells*.

Settari, A. (1980). Simulation of hydraulic fracturing processes. *Old SPE Journal*, *20*(6), 487-500.

Settari, A. (1988, October). General Model of Fluid Flow (Leakoff) From Fractures Induced in Injection Operations. In *SPE Annual Technical Conference and Exhibition*.

Sieder, E. N., & Tate, G. E. (1936). Heat transfer and pressure drop of liquids in tubes. *Industrial & Engineering Chemistry*, *28*(12), 1429-1435.

Suri, A., & Sharma, M. (2009, January). Fracture Growth in Horizontal Injectors. In *SPE Hydraulic Fracturing Technology Conference*.

Suri, A., Sharma, M., & Peters, E. (2010, May). Estimates of Fracture Lengths and Injection Profile in an Injection Well by History Matching Bottom Hole Pressures. In *SPE Western Regional Meeting*.

Tao, Q., Checkai, D., Huerta, N., & Bryant, S. (2010, September). Model to Predict CO_2 Leakage Rates Along a Wellbore. In *SPE Annual Technical Conference and Exhibition*.

Takahashi, T., Goldberg, D., & Mutter, J. C. (2000). Secure, long-term sequestration of CO_2 in deep saline aquifers associated with oceanic and continental basaltic rocks. *Proc of the SRI Int Sympos, Deep Sea & CO_2*.

Van der Meer, L. G. H. (1992). Investigations regarding the storage of carbon dioxide in aquifers in the Netherlands. *Energy Conversion and Management* 33.5: 611-618.

Wertz, Frédéric, Pascal Audigane, and Olivier Bouc. (2009). CO_2-Thermodynamic Model in a Leaking Well. *Energy Procedia* 1.1: 1791-1798.

Zoback, M. D. (2010). Reservoir geomechanics. *Cambridge University Press*.

Zoback, M. D., & Gorelick, S. M. (2012). Earthquake triggering and large-scale geologic storage of carbon dioxide. *Proceedings of the National Academy of Sciences*, *109*(26), 10164-10168.

Zuluaga, A. (2005),. Geochemical effects in two-phase flow, PhD Dissertation, University of Texas at Austin